

Electronic Thesis and Dissertation Repository

4-19-2013 12:00 AM

Magnetic Resonance Imaging of a Natural Killer Cell Therapy in a Mouse Model of Prostate Cancer

Christiane L. Mallett
The University of Western Ontario

Supervisor
Paula Foster
The University of Western Ontario

Graduate Program in Medical Biophysics
A thesis submitted in partial fulfillment of the requirements for the degree in Doctor of Philosophy
© Christiane L. Mallett 2013

Follow this and additional works at: <https://ir.lib.uwo.ca/etd>



Part of the [Medicine and Health Sciences Commons](#)

Recommended Citation

Mallett, Christiane L., "Magnetic Resonance Imaging of a Natural Killer Cell Therapy in a Mouse Model of Prostate Cancer" (2013). *Electronic Thesis and Dissertation Repository*. 1234.
<https://ir.lib.uwo.ca/etd/1234>

This Dissertation/Thesis is brought to you for free and open access by Scholarship@Western. It has been accepted for inclusion in Electronic Thesis and Dissertation Repository by an authorized administrator of Scholarship@Western. For more information, please contact wlsadmin@uwo.ca.

Magnetic Resonance Imaging of Natural Killer Cell Therapy in a Mouse Model of
Prostate Cancer

(Thesis format: Integrated Article)

by

Christiane Lynn Mallett

Graduate Program in Medical Biophysics
Collaborative Program in Molecular Imaging

A thesis submitted in partial fulfillment
of the requirements for the degree of
Doctor of Philosophy

The School of Graduate and Postdoctoral Studies
The University of Western Ontario
London, Ontario, Canada

© Christiane Mallett 2013

Abstract

Purpose: This thesis uses magnetic resonance imaging (MRI) techniques to study natural killer (NK) cell therapy in a nude mouse model of prostate cancer. Cellular MRI, anatomical MRI and hyperpolarized ^{13}C pyruvate spectroscopy were used to study various aspects of the model. **Methods:** The cells used were KHYG-1 NK cells and PC-3M prostate cancer cells. Imaging was performed on a clinical 3T GE MR750 scanner, using a high-performance gradient insert for acquisition with the balanced steady state free precession (bSSFP) sequence, and using the built-in gradients for ^{13}C pyruvate spectroscopy. Pyruvate was hyperpolarized by dynamic nuclear polarization. **Results:** KHYG-1 were toxic to PC-3M *in vitro*, and were successfully labeled with MoldayRhodamine, a superparamagnetic iron oxide nanoparticle (SPIO). A subcutaneous PC-3M tumour model was used to investigate tracking of KHYG-1 *in vivo* using the bSSFP sequence. Four days after administration, KHYG-1 accumulation in the tumours was detected by histology but not by MRI, although labeled KHYG-1 at high density were visible in MR images. The bSSFP sequence was then optimized for imaging the mouse prostate and the whole mouse body. Tumour development in an orthotopic prostate cancer model was characterized by MRI and histology for tumour growth, metastasis and tumour metabolism. Tumours were visible by MRI day 9 after injection. Using histology, metastasis was detected in the lymph nodes and spleen of the mice. Necrotic regions in the tumours were detected on day 22 by both anatomical imaging and pyruvate spectroscopy and were confirmed by histology. **Conclusions:** KHYG-1 cell therapy shows promise as a treatment of prostate cancer. A mouse model that developed lymph node metastases was characterized. Based on the accumulation of KHYG-1 in SC tumours 4 days after administration, and the consistent presence of MRI-visible tumours on day 9-13, a treatment time point of 9-13 days is proposed for future NK cell tracking experiments.

Keywords: Natural killer cells, prostate cancer, KHYG-1, PC-3M, MRI, cell tracking, SPIO, bSSFP, hyperpolarized carbon 13 spectroscopy, pyruvate, nude mouse, metastasis

Co-Authorship Statement

Chapter 2 contains material from 2 previously published papers. The first is C McFadden, CL Mallett and PJ Foster (2011) *Labeling of multiple cell lines using a new iron oxide agent for cell tracking by MRI* Contrast Media and Molecular Imaging 6:6, 514-522. For this paper, PJF contributed to experimental design and to writing the paper, CM performed most experiments, contributed to experimental design and wrote the manuscript. CLM performed some experiments and contributed to writing the manuscript. The second paper is CL Mallett, C McFadden, Y Chen and PJ Foster (2012) *Migration of iron-labeled KHYG-1 natural killer cells to subcutaneous tumors in nude mice, as detected by magnetic resonance imaging* Cytotherapy 14:6, 743-51. For this paper, CLM worked on experimental design and did the majority of the experimental work and writing. CM assisted with cell culture and writing the manuscript, YC performed the histology and assisted with writing the manuscript, and PJF contributed to experimental design and manuscript writing.

Chapter 3 is reprinted from: CL Mallett and PJ Foster (2011) *Optimization of the Balanced Steady State Free Precession (bSSFP) Pulse Sequence for Magnetic Resonance Imaging of the Mouse Prostate at 3T* PLoSONE 6(4):e18361. CLM contributed to experimental design, performed the experiments, analysed the data and wrote the manuscript. PJF contributed to experimental design and assisted with manuscript preparation.

Chapter 4 is in preparation for submission to the journal The Prostate. The authors are: CL Mallett, H Lim, K Thind, Y Chen, E Ribot, F Martinez, TJ Scholl, PJ Foster. CLM contributed to experimental design, performed the experiments, analysed the data and wrote the manuscript. HL, KT, FM, ER and TJS contributed to the design and performance of the ^{13}C experiments, and HL and KT assisted with analysis of that data and writing of that section of the manuscript. YC performed the surgery and did the histology. PJF contributed to experimental design and manuscript preparation.

Acknowledgments

I'd like to begin by thanking my supervisor, Paula Foster for a great experience over the last 4 years. I'm grateful that she welcomed me into her lab when I (typically) asked to join at the last minute. I appreciate her ability to focus a project and calmly rescue it from small disasters, and thank her for letting me run with ideas when I felt strongly about them but also making sure I kept my plans realistic. My advisory committee has also been really helpful – Greg Dekaban asked the immunology questions that I should answer with my work and his lab provided immunology and technical support. Tim Scholl helped to design my last experiment one day at a poster session and was always a positive person when I needed MRI help or to borrow the majority of his lab for a few days at the scanner.

This project would not have been possible without the help of Yuhua Chen – thanks for cutting and staining all that tissue, learning a new surgery and teaching me how to suture the little guys after their operations. Catherine McFadden was a great help as we both learned how to deal with a new cell line and was always available to answer my cell-related questions and figure out what was going on when I had troubles. Thanks to Sherri Couto for being great at multitasking to make sure all the important paperwork was done and Anne Leaist for the cookies and special occasion chocolates. I'd also like to thank the summer students and volunteers who assisted with segmenting the many many images I had: Freda Jawan, Philip Gareau and Jason Woowon Shin. Other members of the Foster lab, both current and past, were also important in the progress of my project and in keeping me entertained while I did it! Thanks to Gabrielle Siegers, for all the immunology and NK cell advice, and for keeping me company in the cell culture room many times. Vas Economopoulos has been a great help – my first resource when I needed to find a paper about a random cancer phenomenon or had an MR question. Emeline Ribot was a perfect conference roommate and gym buddy and was super-helpful with her magical ability to catheterize mice! Amanda Hamilton always knew the answer to my histology questions and was another fun conference co-attender. And past students Shruti Krishnamoorthy, Jenny Noad, Dean Percy and Jon Snir, you made the days go by much

quicker with your companionship and trips to the movies! Laura Gonzalez and Paco Martinez, thanks for your kindness when I needed a ride during the bus strike, but also for your endless generosity with scientific and lab questions, as well as coming to the 3T at all hours of the day to troubleshoot. Many other students were very helpful with scanning, especially with setting aside their own projects for the spectroscopy experiments, Patrick Lim and Kundan Thind in particular. Thanks to Lanette Friesen Waldner and Charlie McKenzie for letting me watch your scanning sessions for inspiration with my project.

And most of all, thanks to my family. I can't reduce your contributions to a few lines, but I will try. Thanks to my Dad, for the ski trips every year, my Mom for the shopping trips and my sister for the moral support over the phone and in person. And all the rest of you for always being interested in what I was doing (and how my mice were doing too).

Table of Contents

Abstract.....	ii
Co-Authorship Statement.....	iii
Acknowledgments.....	iv
Table of Contents.....	vi
List of Tables.....	x
List of Figures.....	xi
List of Appendices.....	xiii
List of Symbols and Abbreviations.....	xiv
Chapter 1.....	1
1 Introduction.....	1
1.1 The Immune System.....	1
1.1.1 The Immune System and Cancer.....	1
1.1.2 Immunosuppressive Environment of Tumours.....	3
1.2 Cancer Immunotherapy.....	3
1.3 Prostate Cancer.....	4
1.3.1 Mouse models of prostate cancer.....	5
1.4 Magnetic Resonance Imaging (MRI).....	6
1.4.1 General MRI.....	7
1.4.2 Pulse Sequences.....	9
1.4.3 Balanced Steady State Free Precession Sequence (bSSFP).....	11
1.4.4 Contrast Agents.....	14
1.5 Cellular Magnetic Resonance Imaging.....	15
1.5.1 Cell Labeling.....	16

1.5.2	Cellular Imaging of Immune Cells	18
1.5.3	Hyperpolarized Spectroscopy	19
1.6	Model	23
1.7	Purpose of Thesis	24
1.7.1	Objectives	24
1.8	References	25
Chapter 2	38
2	Labeling of KHYG-1 with Molday-Rhodamine and MRI of Migration to Subcutaneous PC-3M Tumours in Nude Mice	38
2.1	Introduction.....	38
2.2	Methods.....	40
2.2.1	Cell Culture.....	40
2.2.2	KHYG-1 Labeling with Iron Oxide Nanoparticle	40
2.2.3	Electron Microscopy.....	41
2.2.4	Cytotoxicity Assay.....	41
2.2.5	<i>In vivo</i> tracking experiments.....	42
2.2.6	Magnetic Resonance Imaging.....	42
2.2.7	Direct injection experiment.....	43
2.2.8	Histology.....	43
2.2.9	Statistics	44
2.3	Results.....	44
2.3.1	Cell Labeling and Cytotoxicity.....	44
2.3.2	Migration of KHYG-1 to PC-3M Tumours	46
2.3.3	<i>In vivo</i> Longitudinal MRI	48
2.3.4	Additional MRI Findings.....	53
2.3.5	Direct Injection Experiment.....	54

2.4 Discussion.....	56
2.5 References.....	61
Chapter 3.....	68
3 Optimization of the Balanced Steady State Free Precession (bSSFP) Pulse Sequence for Magnetic Resonance Imaging of the Mouse Prostate at 3T.....	68
3.1 Introduction.....	68
3.2 Methods.....	69
3.2.1 Animals.....	69
3.2.2 MRI.....	69
3.2.3 Image Analysis.....	70
3.3 Results.....	70
3.3.1 Effect of phase cycles and averaging.....	70
3.3.2 Effect of bandwidth and flip angle.....	71
3.3.3 Comparison of bSSFP with T_{1w} and T_{2w} SE.....	72
3.3.4 3D nature of bSSFP.....	73
3.4 Discussion.....	75
3.5 References.....	77
Chapter 4.....	82
4 Anatomical and Metabolic Magnetic Resonance Imaging Characterization of an Orthotopic Mouse Model of Prostate Cancer Using the PC-3M Cell Line in Nude Mice.....	82
4.1 Introduction.....	82
4.2 Methods.....	83
4.2.1 Cells.....	83
4.2.2 Tumour Cell Injection.....	84
4.2.3 Anatomical Imaging Study.....	84

4.2.4	Anatomical Magnetic Resonance Imaging	84
4.2.5	Spectroscopic Imaging.....	85
4.2.6	Histology.....	86
4.2.7	Statistical Analysis.....	87
4.3	Results.....	87
4.3.1	Tumour Appearance in MRI Images	87
4.3.2	Tumour Volume.....	88
4.3.3	Lymph Node Histology.....	90
4.3.4	MR appearance of metastatic lymph nodes	93
4.3.5	Pyruvate Metabolism	94
4.3.6	Sample Size Calculation	97
4.4	Discussion	98
4.5	References.....	103
Chapter 5	108
5	Summary and Future Work.....	108
5.1	Conclusions.....	108
5.2	Future Work.....	109
5.2.1	NK Cell Dose Optimization.....	110
5.2.2	Metabolic Imaging.....	111
5.2.3	Bioluminescence Imaging.....	111
5.2.4	Imaging NK Cells in Metastatic Models	112
5.3	References.....	113
Appendices	115
Curriculum Vitae	123

List of Tables

Table 1.1: Properties of Selected Iron Oxide Nanoparticles.....	16
Table 4.1: Summary of locations where prostate cancer cells were detected.....	90
Table 4.2: Summary of previous PC-3 and PC-3M tumour growth and metastasis.....	101

List of Figures

Figure 1.1: T_1 and T_2 relaxation curves.....	9
Figure 1.2: Vector diagram of spin-echo pulse sequence.....	10
Figure 1.3: Vector diagram of gradient-echo pulse sequence.....	11
Figure 1.4: Pulse sequence diagram for balanced steady state free precession (bSSFP) sequence.....	12
Figure 1.5: Example of a phase cycling scheme for 4 phase cycles.....	13
Figure 1.6: Metabolic fate of pyruvate changes depending on tissue type and proliferation.....	21
Figure 1.7: Sample lactate and pyruvate spectrum.....	22
Figure 1.8 The mouse prostate.....	23
Figure 2.1: KHYG-1 labeling with MoldayION RhodamineB was highly efficient.....	45
Figure 2.2: Molday labeling did not affect KHYG-1 cytotoxicity to PC-3M cells.....	45
Figure 2.3: KHYG-1 were present in tumours after all routes of administration.....	47
Figure 2.4: There are live NK cells in the tumours.....	48
Figure 2.5: Signal loss at edge of tumour after subcutaneous injection of labeled KHYG-1 cells and histological validation of KHYG-1 in tumour margins.....	50
Figure 2.6: Labeled KHYG-1 are in the tumour but not detectable by MRI.....	52
Figure 2.7: Rhodamine and iron are co-localized.....	53
Figure 2.8: Additional MR signal loss patterns.....	54

Figure 2.9: Effect of KHYG-1 direct injection on tumour volume.	55
Figure 2.10: Histology of intratumoural injection site.....	56
Figure 3.1: Effect of phase cycling and averaging on <i>ex vivo</i> prostate image quality.....	71
Figure 3.2: Effect of flip angle and bandwidth on prostate visibility and artifacts.	72
Figure 3.3: Comparison of <i>in vivo</i> axial images acquired with 3 different pulse sequences..	73
Figure 3.4: 3 views of prostate from one 3-dimensional <i>in vivo</i> scan.	74
Figure 3.5: Sections of coronal view of mouse with prostate and lymph nodes identified. ...	74
Figure 4.1: MR appearance and sample segmentation of the prostate and tumour over time.	88
Figure 4.2: Tumour volume over time.....	89
Figure 4.3: Distribution of multiple tumour lobes.....	89
Figure 4.4: Presence of PC-3M in lymph nodes and spleens.	92
Figure 4.5: MR appearance of the iliac lymph node over time.	93
Figure 4.6: Volumes of iliac and inguinal lymph nodes over time.....	94
Figure 4.7: Sample image of lactate/pyruvate spectrum in a tumour with variable uptake....	95
Figure 4.8: Comparison of lactate/pyruvate ratio in voxels with high and low pyruvate and lactate signal.....	96
Figure 4.9: Comparison of spectroscopy, bSSFP and histology.....	97

List of Appendices

Appendix A: Longitudinal 13C Data.....	115
Appendix B: Permissions.....	120
Appendix C: Animal Use Protocol.....	122

List of Symbols and Abbreviations

2D	Two-dimensional
3D	Three-dimensional
α	Flip angle
Ag	Antigen
ATP	Adenosine triphosphate
B_0	Main magnetic field
BLI	Bioluminescence imaging
bSSFP	Balanced steady state free precession
BW	Bandwidth
CHES	Chemical shift selective sequence
CME	Clathrin-mediated endocytosis
CNR	Contrast-to-noise ratio
CRPC	Castration resistant (or recurrent) prostate cancer
CSI	Chemical shift imaging
DAPI	4',6-diamidino-2-phenylindole
DC	Dendritic cell
DNP	Dynamic nuclear polarization
FA	Flip angle
FBS	Fetal bovine serum
FDA	Federal Drug Administration (US)
FOV	Field of view
FSE	Fast spin echo
γ	Larmor frequency
Gd	Gadolinium
GE	General Electric
GI	Gastrointestinal
GM-CSF	Granulocyte macrophage colony stimulating factor
GMP	Good manufacturing practices
GRE	Gradient echo
H & E	Hematoxylin and eosin
HBSS	Hanks balanced salt solution
HuNu	Human nuclear membrane
IC	Intracardiac
IFN- γ	Interferon γ
IL	Interleukin
ILN	Inguinal lymph node
IP	Intraperitoneal
IV	Intravenous
KIR	Killer immunoglobulin-like receptor
Lac/pyr	Lactate to pyruvate ratio
mCRPC	Metastatic castration resistant (or recurrent) prostate cancer
MDSC	Myeloid derived suppressor cells
MHC I	Major histocompatibility complex I

MPIO	Micron-sized iron oxide particle
MRI	Magnetic resonance imaging
MTT	(3-(4,5-Dimethylthiazol-2-yl)-2,5-diphenyltetrazolium bromide
NEX	Number of excitations
NK	Natural killer cell
PAP	Prostatic acid phosphatase
PPB	Perls' Prussian blue
PC	Phase cycles
PET	Positron emission tomography
PSA	Prostate serum antigen
r_1	Longitudinal relaxivity
r_2	Transverse relaxivity
RARE	Rapid acquisition with refocused echoes
RF	Radiofrequency
ROS	Reactive oxygen species
RPMI	Roswell Park Memorial Institute media
SC	Subcutaneous
SE	Spin echo
SNR	Signal-to-noise ratio
SPECT	Single photon emission computed tomography
SPIO	Superparamagnetic iron oxide nanoparticle
T	Tesla
T_1	Longitudinal (spin-lattice) relaxation
T_1W	T1-weighted
T_2	Transverse (spin-spin) relaxation
T_2^*	Apparent transverse relaxation
T_2W	T2-weighted
TAM	Tumour-associated macrophage
TE	Echo time
TEM	Transmission electron microscopy
TNF	Tumour necrosis factor
TR	Repetition time
TRAMP	Transgenic adenocarcinoma of the mouse prostate
T_{reg}	Regulatory T-cell
TUNEL	Terminal deoxynucleotidyl transferase dUTP nick end labeling
USPIO	Ultrasmall superparamagnetic iron oxide nanoparticle

Chapter 1

1 Introduction

Prostate cancer is a leading cause of cancer death in North American men (1,2). New treatment strategies are required for treating the disease, particularly metastatic prostate cancer. A promising field of study involves using the immune system as a treatment for prostate cancer. In this thesis, we use magnetic resonance imaging (MRI) to track an immune therapy for prostate cancer using natural killer cells (NK), and fully characterize a metastatic mouse model of prostate cancer.

1.1 The Immune System

In general, one purpose of the immune system is to differentiate cells that are “self” from “non-self” and eliminate cells that do not belong. Immune cells are constantly circulating through the blood and lymphatic systems to detect non-self and abnormal cells; one important cell surface marker of “self” is the major histocompatibility complex I (MHC I) that is shared by all cells in an organism. The immune system is composed of 2 parts, the innate and the adaptive immune systems. The innate immune system is the first, less specific response to pathological organisms and non-self cells or abnormal cells. Cells that are part of the innate immune system include natural killer cells (NK), $\gamma\delta$ T-cells, macrophages, mast cells and others. The adaptive immune system takes a few days to respond to threats and provides a reaction that is specific to a foreign or non-self antigen, is long-lasting and can respond to subsequent presentations of the same foreign antigen much more quickly. This system includes cells such as T-cells (of the $\alpha\beta$ subtype), and B cells, among others. The two systems are bridged by dendritic cells (DC) (3).

1.1.1 The Immune System and Cancer

Many cells of the innate immune system are involved in cancer immunology, in both tumour-promoting and tumour-suppressing roles. Natural killer cells and $\gamma\delta$ T-cells are directly cytotoxic towards tumour cells, but myeloid derived suppressor cells (MDSC), DC and macrophages are also important in the immune response toward cancer (4). The

focus of this thesis is NK cells, although there are similarities in mechanism between the Nk and $\gamma\delta$ T-cells. NK cytotoxicity depends on the cell-to-cell contact between the NK cell and the target cell and the engagement of receptors and ligands between the cells. NK have both activating and inhibitory receptors for cytotoxicity, and if more activating than inhibitory receptors are engaged, then the NK cell is activated (5). There are 3 key types of receptors on NK cells that determine their activity: the natural cytotoxicity receptors, the killer immunoglobulin-like receptors (KIR) and the lectin-type receptors. Inhibitory KIR such as KIR2D4, KIR3DL and KIR2DL recognize MHC I molecules on the target cell to prevent NK from killing healthy cells. Activating receptors include the natural cytotoxicity receptors NKp30, NKp44 and NKp46, which bind to proteins on the surface of target cells that are transformed by viral infection or by the transformation to cancer cells. Another activating receptor expressed by NK cells is called NKG2D, a lectin-type receptor that recognizes stress-induced markers MIC A/B and ULBP (6), which are present on a variety of tumour types including prostate cancer (7). Once activated, NK cells kill the target cell through one of two pathways: the release of cytotoxic granules containing perforin and granzyme, or the expression of death ligands such as Fas and tumour necrosis factor (TNF) to trigger apoptosis in the target cell, as well as releasing cytokines such as interferon- γ (IFN- γ) to stimulate other immune cells (5).

DC activate T-cells and NK cells to act in concert to target tumour cells. Immature DC serve as sentinels and are distributed throughout the body, and when they encounter a foreign antigen (Ag) in combination with a pro-inflammatory danger signal, they take the Ag up and start to differentiate into a mature, migratory DC phenotype and begin to display activation markers as well. Then, the DC migrates to a draining lymph node, completing its maturation and becoming fully activated on contact with T cells. There, it presents the foreign or non-self antigen to T-cells present in the lymph node. The T-cells activate and rapidly proliferate so that they can then circulate and kill the cells expressing that antigen, once again through the release of perforin and granzymes (3). Mature DC can also activate NK cells to become more effective killer cells (8,9). Upon cell-to-cell contact, mature DC induce NK to produce IFN- γ and also increase their cytolytic activity toward tumour cells (9).

1.1.2 Immunosuppressive Environment of Tumours

The tumour microenvironment helps the tumour to evade the immune system by producing factors that upregulate and activate regulatory cells of the immune system. Regulatory T-cells (T_{reg}) suppress the proliferation of T-cells by secreting TGF- β and IL-10 or through cell contact-dependent mechanisms (10). Myeloid derived suppressor cells (MDSC), which are improperly matured dendritic cells, monocytes and macrophages, produce reactive oxygen species (ROS) that inhibit T-cell function, and also inhibit expansion of T-cells through the secretion of TGF- β and the metabolism of arginine (11). MDSC also inhibit NK cell cytotoxicity (12). Both T_{regs} and MDSC are activated/recruited by tumour-derived factors (10,11). Tumour-associated macrophages (TAM) that are activated by the M2 pathway – the most common type of macrophage in the tumour microenvironment – similarly inhibit T-cell function through the secretion of IL-10 and reactive oxygen species (ROS) (10,13). As well, MHC I molecules on the tumour cells can be downregulated, resulting in a lower T-cell response (14).

1.2 Cancer Immunotherapy

The goal of cancer immunotherapy is to use the immune system to treat cancer. Early iterations involved stimulating the immune system with interleukin-2 (IL-2), although this had limited effectiveness and toxic side effects (15). Other treatments attempted to stimulate existing cells have included IFN- γ (16) and granulocyte macrophage colony stimulating factor (GM-CSF) (17). More recently, DC based vaccines have been investigated. With DC based vaccines, DC are harvested from the patient, then pulsed with a tumour antigen *ex vivo* and returned to the patient to induce a T-cell and NK-cell based immune response (18). As well, autologous and allogenic tumor infiltrating T-cells have also been expanded *ex vivo* and adoptively transferred into patients. Alternatively, T-cells that are specific to the tumour's antigen(s) are extracted from the patient's blood are selected and expanded, and then are transplanted back into the patient. This therapy has been tested in early phase trials of patients with melanoma (19,20).

NK cells are an attractive cell type for immunotherapy because they kill target cells without needing to be sensitized in an antigen specific manner. NK cell-based therapy is being studied for solid tumours and leukemia/lymphoma. Early phase clinical trials are in progress, with mixed results – some trials were terminated early for toxicity, some had no expansion of the administered NK cells, and some reached their endpoints successfully (for example, [clinicaltrials.gov](https://clinicaltrials.gov/ct2/show/study/NCT00652899) identifiers NCT00652899, NCT00328861, NCT00823524, NCT00697671). Several avenues of NK cell therapy are being explored, including *in vivo* and *ex vivo* expansion of the patient's NK cells, *ex vivo* expansion of allogenic NK cells from a donor, or administration of cytotoxic cell lines (such as NK-92, YT or KHYG-1) (21-23). Cytotoxic cell lines can be expanded *ex vivo* in compliance with good manufacturing practices (GMP) (21) and have the advantage of expressing a different receptor repertoire than the patient's own NK cells, which have already allowed immune evasion of the tumour cells. In human trials, NK cell therapy is administered as one or several IV infusions or an intra-arterial injection (24-26).

1.3 Prostate Cancer

Immunotherapies are being investigated in a variety of blood-borne and solid tumours, including prostate cancer. Prostate cancer is the 3rd most deadly cancer in Canadian men, and the 2nd most deadly in American men (1,2) and the most commonly diagnosed cancer in men. Early cancers are detected by a blood test for elevated Prostate Serum Antigen (PSA) and confirmed by a biopsy. The differentiation of the cells in the biopsy core is used to grade the cancer and is called the Gleason score (27,28). The higher the Gleason score, the more advanced the cancer. Prostate cancer is generally slow growing, so the first line of treatment is watchful waiting or active surveillance, to monitor disease progress. In cases where treatment is needed, it includes androgen deprivation therapy – prostate cancer is dependent on testosterone for growth in its initial stages – radiotherapy and surgical removal of the prostate, all of which have side effects ranging from lower gastrointestinal effects to incontinence and impotence. Prostate cancer most commonly metastasizes to the bone, lung, lymph nodes and liver (29).

More advanced cancers are androgen-independent and so androgen-deprivation therapy becomes ineffective. When androgen therapy fails, the cancer is then termed castration-resistant (or recurrent) prostate cancer (CRPC), and can be either metastatic or confined at this stage (18). The current treatment for metastatic CRPC (mCRPC) is docetaxel. After docetaxel has failed, additional chemotherapeutic agents such as cabazitaxel and abiraterone are approved for treatment (in conjunction with prednisone) (18,30).

Immunotherapy is approved to treat patients with mCRPC and may offer a treatment option with fewer side effects than chemotherapy (30). Sipuleucel-T involves drawing blood from the patient and retaining the DC, T-cells, monocytes, B cells and NK cells (31). Then the cells are co-cultured with a fusion antigen comprised of GM-CSF (to activate immune cells) and prostatic acid phosphatase (PAP, an antigen that is overexpressed in most prostate cancers (31,32)). The fusion protein is washed out and the leukocytes are administered to the patient, where they are assumed to induce a T-cell response (30,32). In a phase III trial, this treatment resulted in an improvement in overall survival of 4.1 months (32).

Other immunotherapies under investigation but not yet out of Phase III trials include the monoclonal antibody ipilimumab, which blocks the CTLA-4 receptor on T-cells that downregulates T-cell activity (30). Another strategy is to induce an immune response to prostate tumours by treating with a poxvirus containing PSA and immune system stimulators (30). Immune therapies under investigation for other cancers include restoring the function of exhausted T-cells (33).

1.3.1 Mouse models of prostate cancer

A variety of mouse strains have been developed that spontaneously develop prostate cancer. These include the TRAMP mouse (transgenic adenocarcinoma of the mouse prostate), which was one of the earliest transgenic mouse models of prostate cancer and is still commonly used (34). Prostate cancer occurs because a promotor is inserted into the epithelial cells of the prostate and inactivates tumour suppressor genes (34,35). This model develops cancer in a predictable way that recapitulates the human disease progression, but rarely metastasizes to bone and is much more rapid than human disease

(35). Other models include those based on deletion of the pten tumour suppressor gene, which can also be combined with other gene deletion to manipulate the phenotype (35).

However, in the context of a model for NK cell-based therapy for prostate cancer, interaction between human NK cells and human prostate cancer is required. A number of different models have been developed that are based on the implantation of human cancer cell lines into immunocompromised mice; immunocompetent mice would reject the implantation of a xenograft as well as the human cell line administered to treat the tumour. The nu/nu or nude mouse lacks mature T-cells and so cannot mount immune responses that are dependent on T-cells, such as cytotoxicity to cells that are infected with viruses and stimulation of B cells to produce antibodies (3). Other, more immune compromised mice include the severe combined immune deficiency or SCID mouse, which has no T or B cells, and SCID/beige mice which have no NK cells (36). The research presented in this thesis, like many other xenograft prostate cancer models (37,38), uses nude mice.

Prostate cancer cell lines have been isolated from human primary or metastatic tumours. Some examples are LNCaP, which is a slow growing cell line that is androgen dependent and the related cell line C4-2B which has a tendency to metastasize to bone (39). PC-3 is another commonly-used cell line which was isolated from a bone metastasis in a patient (40). This cell line was further passaged *in vivo* in a mouse and a splenic metastasis was cultured to develop the PC-3M cell line, which is a highly metastatic cell line that is androgen independent (41), and so models the more advanced case of CRPC.

1.4 Magnetic Resonance Imaging (MRI)

Subcutaneous (SC) tumour growth can be easily measured with calipers, but this is difficult with orthotopic tumours because they are difficult to palpate until they are quite large. Magnetic resonance imaging (MRI), a non-invasive imaging modality with excellent soft tissue contrast, is an ideal method to monitor orthotopic tumour growth and response to therapy.

1.4.1 General MRI

MRI derives a signal by exploiting the interaction between nuclear spin and an externally-applied magnetic and radiofrequency (RF) field. This requires no ionizing radiation and results in an image with excellent soft-tissue contrast. The contrast can be manipulated to emphasize different tissues by changing the parameters of RF excitation and manipulating the magnetic field in the sample.

An MRI system consists of 3 components: a main magnetic field, gradient coils and radiofrequency coils. Each component is important in image creation. Interaction with the sample occurs at the level of the nucleus. All nuclei have an intrinsic property known as spin – only those nuclei with non-zero nuclear spin are visible with MRI and those with $\frac{1}{2}$ spin are the most useful. Hydrogen, as the most abundant element in our bodies, is the usual nucleus detected by MRI. The orientation of these nuclei or ‘spins’ is determined by thermodynamic principles and is random when they are outside of a magnetic field. When the sample is placed inside a strong external magnetic field, as in the bore of the MRI scanner, the spins precess around the magnetic field and tend to align with or against the magnetic field; the stronger the field, the more net alignment there is and so the stronger the magnetization. The net alignment is still very small, however, at 10 ppm in a 3T field. The frequency of precession is determined by the Larmor equation:

$$\omega_0 = \gamma B_0 \quad (1)$$

where ω_0 is the angular frequency of the spins, γ is the gyromagnetic ratio of the spins (42.5 MHz/T for protons), and B_0 is the strength of the main magnetic field. In the coordinate system used in MRI, the axis of the scanner that is parallel to the bore is the z -axis, with the xy -plane perpendicular to the bore.

The gradient coils are used to encode for position along one axis (eg the z -axis) of the scanner by creating a field that is approximately linear in space. The frequency of precession is field-dependent, so the frequency is linearly dependent on position along that axis. The assumption in image reconstruction is that all changes in frequency are a

result of manipulation of the gradients; however, the moving electrons in molecules also create a varying magnetic field and can actually shield the hydrogen nuclei so that they are exposed to a different effective magnetic field, and so precess at a different frequency than the one imposed by the field applied by the scanner. This can lead to an artifact called chemical shift, where signal is assigned to the wrong physical location because its frequency has been increased or decreased by local differences in magnetic field.

The position in the other directions (eg x and y directions) is also determined using the gradient fields. Magnetic gradient pulses are applied to change the phase (but not the frequency) of the rotation of the spins as a function of position; the longer a positive gradient is applied, the more the phase will change. This can be used to encode position in 2 directions for 3D imaging, or in one other direction for 2D imaging.

The RF pulse excites a portion of the spins into a stable high-energy state, which effectively ‘tips’ the magnetization from the z -axis into the xy -plane – the longer the pulse lasts and the greater its amplitude, the more the magnetization tips. The magnetization is also precessing around the z -axis at the Larmor frequency, so to simplify the conceptualization of the MR sequences, it is easier to consider a rotating frame of reference that is also rotating at the Larmor frequency ($x'y'$ -plane). The magnetization decays back to the low energy state through two mechanisms: spin-lattice, or longitudinal (T_1) relaxation and spin-spin or transverse (T_2) relaxation (Figure 1.1). T_1 relaxation involves the increase of the magnetization along the z -axis and is achieved by the transfer of energy from the nucleus to the lattice around it. T_2 relaxation involves the transfer of energy between spins, so that the net amount of magnetization decays because of loss of spin coherence. T_2^* relaxation is due to local inhomogeneities in the magnetic field caused by either the magnet itself or by differences in susceptibility such as bone, air or blood with high iron content and also causes signal to decay in the xy plane (42). Magnetization lost through T_2^* effects is by rephasing the spins, while magnetization lost through T_2 effects is not. The recovery of the longitudinal magnetization is exponential and is characterized by the time constant T_1 ; it takes about 5 T_1 intervals to return to the initial level of magnetization. Similarly, the decay of the transverse magnetization is exponential and is characterized by the time constant T_2 (42).

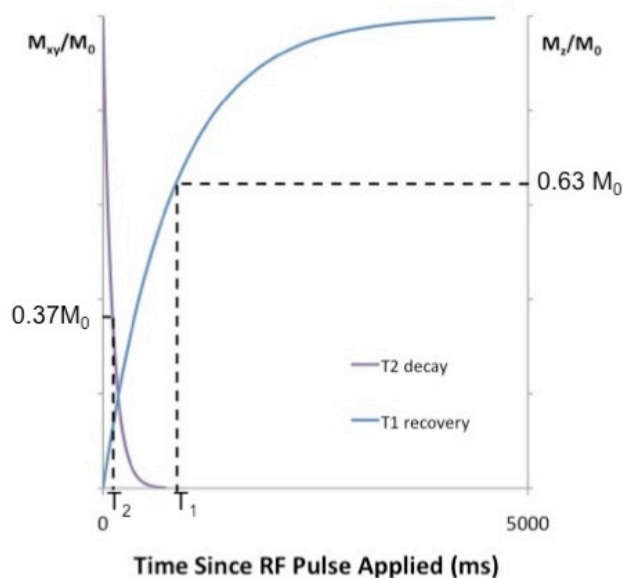


Figure 1.1: T_1 and T_2 relaxation curves.

Decay of transverse magnetization due to T_2 relaxation (dephasing of spins) (purple, left axis) and recovery of longitudinal magnetization due to T_1 relaxation (blue, right axis). T_2 is the time it takes for the transverse magnetization to decay by 63% and T_1 is the time for the longitudinal relaxation to recover to 63% of its initial value. Values calculated for white matter relaxation values of $T_1/T_2=1331/80$ ms. Figure adapted from (42).

1.4.2 Pulse Sequences

Pulse sequences are programmed manipulations of the gradient and RF coils. They are categorized by the method they use to generate an image as either spin-echo (SE) or gradient-echo (GRE), and by the timing of the echoes, as either T_1 weighted or T_2 (or T_2^*) weighted. The timing of the echoes is defined by the repetition time TR (the time between the excitations) and the echo time TE (the time between the excitation and reading the signal).

In a SE sequence (Figure 1.2), the spins are tipped into the xy plane by a 90° pulse, then allowed to dephase for a certain amount of time ($TE/2$). Then a 180° pulse is applied; this reverses the direction of the spins and so they begin to rephase and an echo is formed at

time TE. This is the signal received by the receive coil and then reconstructed using a Fourier transform to form the image. The magnitude of the echo is determined by how much T2 decay has occurred. Differences in magnetic field inhomogeneity do not affect the magnitude of the echo (42).

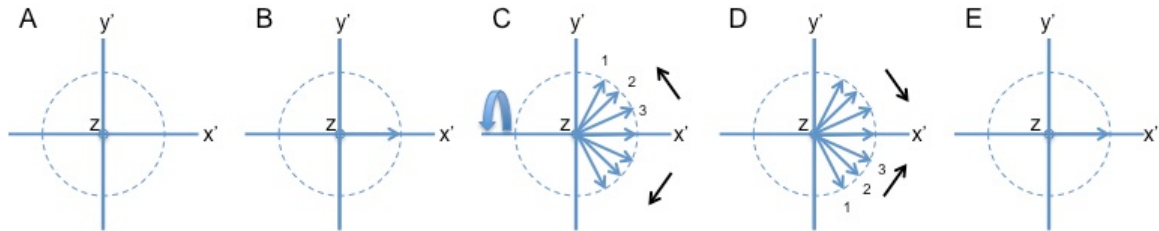


Figure 1.2: Vector diagram of spin-echo pulse sequence.

A) The magnetization is pointed along the z axis. B) A 90° RF pulse is applied, tipping the magnetization into the $x'y'$ plane. C) Spins have dephased and at time TE/2 180° pulse is applied to flip the vectors. D) Spins start to rephase. E) At time TE, spins have reached maximum rephasing and the signal is read. This simple model does not include T_2 effects. Figure adapted from (42).

In a GRE sequence (Figure 1.3), the spins are tipped into the xy plane by some angle α that is usually smaller than 90° . Then, instead of allowing the spins to dephase naturally, a negative gradient is applied to rapidly dephase the spins for a time, then a positive gradient is applied to rephase them at time TE. In contrast to SE, differences in spins due to magnetic field inhomogeneity are not rephased by the gradients, so the magnitude of the echo is determined by T_2^* (42). Because the dephasing is induced by the gradients instead of occurring naturally, GRE sequences are faster than SE and result in less power deposition because GRE sequences use fewer 90° and 180° pulses than SE sequences.

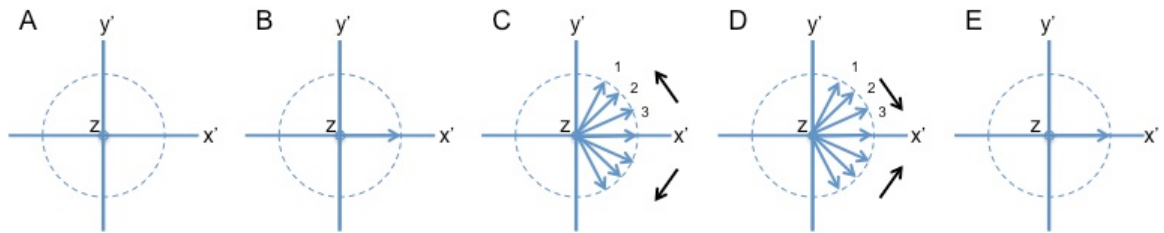


Figure 1.3: Vector diagram of gradient-echo pulse sequence.

A) Magnetization is pointed along the z direction. When an RF pulse is applied, the magnetization is tipped to lie on the x' axis (B). Then a negative gradient rapidly dephases the spins (C), followed by a positive gradient to rephase the spins (E). At the echo time (E), the spins have rephased. This simple model does not include T_2^* effects. Figure adapted from (42).

1.4.3 Balanced Steady State Free Precession Sequence (bSSFP)

This pulse sequence, also known by the manufacturers' names of TrueFISP (Siemens), balanced FFE (Phillips) and FIESTA (GE Healthcare), is unique because the dephasing induced by the gradients is balanced, which means that each positive RF or gradient pulse is balanced by a negative RF or gradient pulse and the residual transverse magnetization is focused at the end of each TR. This feature results in minimal magnetization loss between excitations (Figure 1.4); thus, bSSFP is the most signal-to-noise (SNR) efficient pulse sequence (42,43).

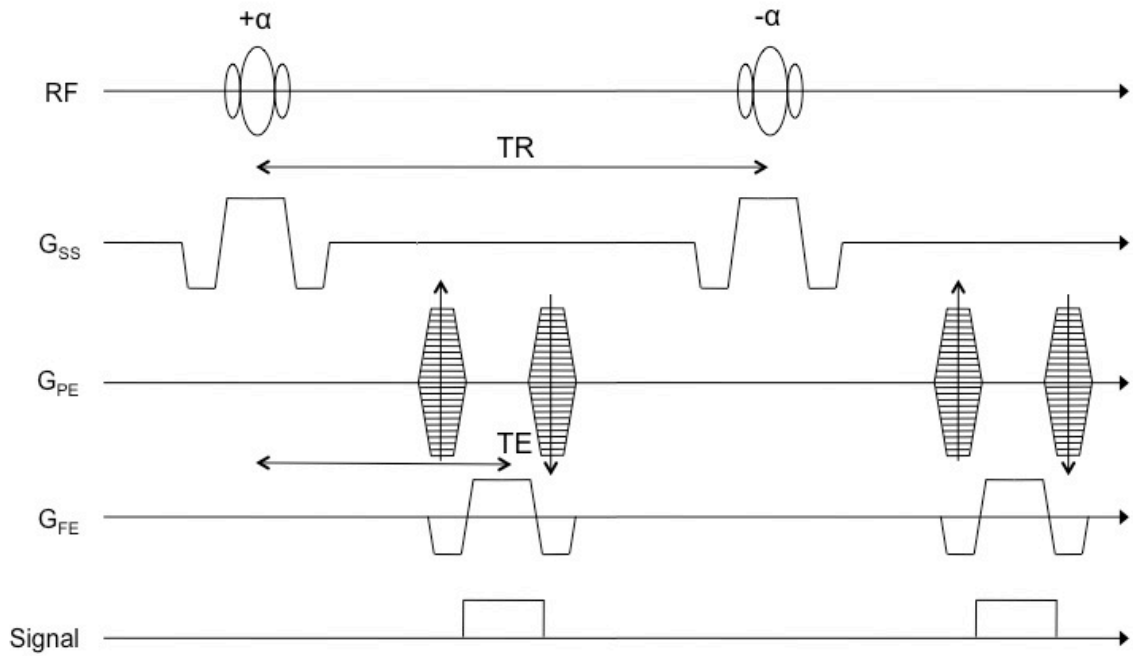


Figure 1.4: Pulse sequence diagram for balanced steady state free precession (bSSFP) sequence.

RF indicates radiofrequency pulse, G_{SS} slice select gradient, G_{PE} phase encode gradient, G_{FE} frequency encode gradient, TR repetition time, TE echo time. Adapted from (42,43).

The flip angle (α) that provides the largest signal for each flip angle can be optimized according to the formula:

$$\cos(\alpha) = \frac{\frac{T_1}{T_2} - 1}{\frac{T_1}{T_2} + 1} \quad (2)$$

Under the biologically relevant conditions that $TR \ll T_1, T_2$, and with the optimal flip angle used, the steady state magnetization (M_{SS}) is described by:

$$M_{SS} = \frac{1}{2} M_0 \sqrt{\frac{T_2}{T_1}} \quad (3)$$

where M_0 is the initial magnetization. Thus, the signal amplitude is proportional to $\sqrt{(T_2/T_1)}$ and so is the image contrast. Additionally, if T_2 and T_1 for the tissues are similar, the signal approaches 50% of the initial magnetization, which is much higher than any other pulse sequence can achieve (43).

One drawback of bSSFP is its sensitivity to off-resonance effects. These appear in the form of banding artifacts, in which thick bands of signal loss appear on the image. Inhomogeneities in the magnetic field create dephasing that is not rephased by the balancing gradients (because it was not caused by the pulse sequence), which leads to regions of signal dropout – when the dephasing approaches 2π the signal reaches zero. This can be corrected by employing phase cycling, so that the initial flipping of the magnetization onto the xy plane is distributed along the plane with each excitation; for example for 4 phase cycles, the magnetization could be flipped onto the x' -axis, the y' axis, the $-x'$ axis and the $-y'$ axis. When the images acquired using the 4 excitations are summed using a sum of squares reconstruction, the banding artifact is averaged out (43,44).

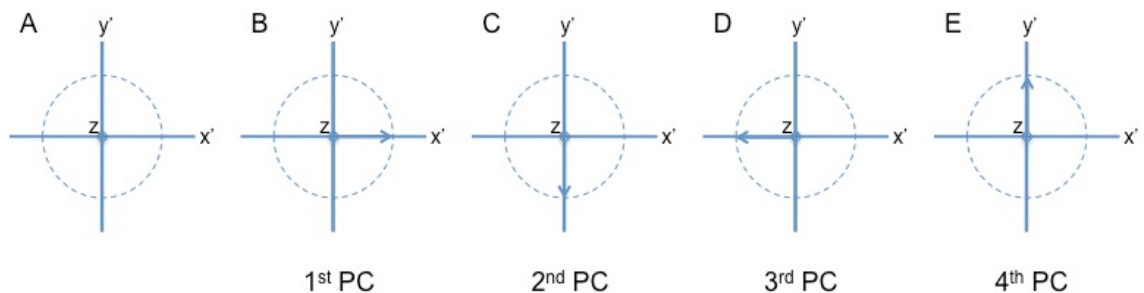


Figure 1.5: Example of a phase cycling scheme for 4 phase cycles.

A) Magnetization is initially along the z axis. B) In the first phase cycle, the magnetization is tipped onto the x' axis. C) In the second phase cycle, it is tipped onto the $-y'$ axis. It is tipped onto the D) $-x'$ and the E) $+y'$ axis in subsequent acquisitions. One complete image is acquired with each phase cycle setting and the images are added using a sum of squares reconstruction.

bSSFP is also sensitive to T_2 contrast agents because of its signal dependence on T_2 ; however, the images are not as affected as some other gradient echo sequences which allows for more precise localization of the signal due to a smaller blooming artifact (45).

bSSFP was not widely clinically used until recently because it requires rapid switching of gradients, which is not possible with older gradient systems. As well, steep gradients are required to obtain smaller voxels suitable for small-animal imaging. This thesis presents bSSFP scans that were obtained using a high-performance gradient insert (46,47) that has gradients ten times stronger than the native gradients in the 3T GEMR750 at our site, as well as integrated cooling to enable long scans with rapid switching of high-gradient fields.

1.4.4 Contrast Agents

The most common MR contrast agent in clinical use is gadolinium (Gd), a T_1 shortening contrast agent. It is administered as an IV injection of a gadolinium chelate (Gd-DTPA). Gd-DTPA first stays in blood vessels, then extravasates, but cannot cross the intact blood-brain barrier. Gd is a paramagnetic metal and decreases the T_1 of nearby nuclei; the extent of its effect is quantified by r_1 or longitudinal relaxivity. Water molecules constantly exchange in and out of proximity to the Gd so the effect is larger than the Gd atom. Where the T_1 is shorter, the image is brighter, so there are hyperintensities in the image where Gd is present. Clinically, Gd in various forms is used for the detection of brain tumours, in angiography, and for the detection of brain lesions due to multiple sclerosis (48-50). In addition, Gd is critical in more advanced methods such as dynamic contrast enhanced MRI (DCE-MRI), in which the kinetics of the wash-in and wash-out of Gd provide information about the blood vessels supplying tumours (51). Gadolinium agents are excreted through the kidneys, usually about 24 hours after administration. Nephrogenic systemic fibrosis is a rare but damaging side effect that is seen when Gd is administered to patients with decreased kidney function (52).

T_2 agents are superparamagnetic and act by producing large inhomogeneities in the magnetic field. This rapidly dephases the transverse magnetization and decreases T_2^* and T_2 , causing a region of signal loss in the image (42). The field perturbation is much larger

in extent than the particle itself and is quantified by r_2 , or transverse relaxivity – the larger the relaxivity, the larger the effect on the magnetic field. These agents are provided as particles in the nanometer to micrometer size range called superparamagnetic iron oxide particles (SPIO). Clinically, SPIO particles are administered IV and then are taken up by phagocytic cells. One application is liver tumour diagnosis; the iron particles are phagocytosed by healthy Kupffer cells in the liver causing normal liver tissue to appear hypointense and liver tumours appear bright. T2 agents are used in conjunction with T2 or T2* weighted sequences. SPIO particles have been approved by the FDA for imaging liver cancer but are no longer being manufactured (53).

1.5 Cellular Magnetic Resonance Imaging

The purpose of cellular MRI is to use contrast agents to obtain contrast between specific cell types and the tissue they are in. These cells can be either transplanted or already present in the body. This technique has been applied to a variety of cell types, including cancer cells (46), immune cells (54,55), neural progenitor cells (56), mesenchymal stromal cells (57) and others. The most common contrast agent used for cellular MRI is SPIO although other agents based on Gd nanoparticles or fluorine are also under investigation (58,59). Cellular MRI using transplanted cells overexpressing iron storage proteins is also being studied (60,61).

SPIO are divided into 3 main classifications by size: micron-sized iron oxide nanoparticles (MPIO) that are approximately 1 μm in diameter, SPIO that are in the 100-500 nm range, and ultra-small particles (USPIO) that are less than 30 nm in diameter. They are often available with a fluorescent tag for visualization by fluorescence microscopy. The particles are typically made of Fe_3O_4 embedded in polystyrene (typical for MPIO), or coated with dextran or dextran derivatives (SPIO and USPIO). Dextran-coated particles are biodegradable and after digestion by lysosomes in the cell, the iron is reused in cellular processes (62). MPIO coated with polystyrene are not degraded by the cells but can be taken up by bystander cells if the original cell undergoes apoptosis (55,63). The properties of a selection of iron oxide nanoparticles including their commercial availability are presented in Table 1.1.

Table 1.1: Properties of Selected Iron Oxide Nanoparticles

Particle	Size (nm)	Coating	Relaxivity (mmol ⁻¹ ·s ⁻¹)	Clinically approved?	Available?
Feridex	120-180	Dextran	r1 40 * r2 160*	Liver imaging	No
Resovist	45-60	Anionic dextran derivative	r1 7.2* r2 82*	Liver imaging	No
MoldayRhodamine	35	Dextran	r1 33 ** r2 71 **	No	Yes
Feraheme	17-31	Anionic dextran	r1 15* r2 89*	Iron replacement	Yes [†]
FeRex	50-150	Dextran	r1 25** r2 161**	No	Yes
Bangs Beads	1000	Polystyrene	r2 50 ^{††}	No	Yes

* at 1.5T, **0.47T, ^{††}4.7T, [†] only available in the US, and for iron replacement therapy

Sources: (63-67)

1.5.1 Cell Labeling

Cells can be labeled for cellular MRI either *ex vivo*, and then administered to the subject, or the contrast agent can be administered IV and then taken up by cells *in vivo*. There are three main methods of uptake of particles into cells which vary depending on the cell type and particle size. Phagocytic cells such as monocytes and macrophages employ phagocytosis to internalize large (>750 nm) foreign particles as part of their normal function (68). In non-phagocytic cells, the most common internalization process is clathrin-mediated endocytosis (CME), which occurs in all cell types and ends with the particle in a lysosome in the cytoplasm (68). This pathway has also been implicated in macrophage uptake of nanosized (~100 nm) particles (69). This can be both receptor-dependent or receptor-independent – the latter is more significant for non-targeted nanoparticles and slightly slower (68). A similar process occurs in small (~50-80 nm) depressions in the cell surface called caveolae and lined by caveolin. This is a more

regulated and signaling-intensive pathway and particles are sent into non-digestive vesicles (68).

In general, adherent cells are much easier to label *in vitro* than non-adherent cells because particles, especially large MPIO, tend to settle to the bottom of the culture dish and so there is less contact between the cells and the nanoparticle when labeling non-adherent cells. Thorek conducted a thorough study of the factors affecting particle uptake in non-adherent cells (T-cells in this case), studying particle sizes from 30 nm - 1.5 μm and various particle coatings. In general, the highest iron uptake was seen in a particle with a diameter of 107 nm and a positive charge (70).

Techniques from cell transfection with DNA have been adapted to cell labeling with iron oxide nanoparticles to enhance uptake. Transfection agents such as lipofectamine, poly-L-lysine and protamine sulfate can be used to coat particles with a cationic coating to increase uptake, although this can also result in particles attached to the outside of cells (71). Electroporation has also been used to improve labeling efficiency for some cells types. This method induces transient pores in the cell surface to allow nanoparticles to enter the cell, although the timing and strength of the electric charge must be carefully calibrated to avoid low cell viability (72). In magnetofection, the cells and label are co-incubated with the cell culture plate sitting on a strong magnet, which pulls the label down towards the cells and increases uptake (73).

At this point, cell tracking with SPIO is primarily a pre-clinical tool. Feridex particles were approved by the FDA for liver imaging; however, they went off-market in 2008 (53). In one clinical study of patients with melanoma, autologous DC were harvested and labeled with Feridex then injected intranodally. MRI was used to determine the success of the injections and to track the DC to adjacent lymph nodes (74). Both Feraheme and protamine sulfate are approved (separately) by the U.S. FDA for non-cell tracking applications.

Pulse sequences used for detecting iron-labeled cells must be sensitive to T2* or T2 effects, so sequences such as T2* weighted GRE and bSSFP are used. As well, small voxels and high SNR are required, although as the amount of iron per voxel increases –

either because of density of labeled cells or amount of iron per cell – voxels can be larger and the signal is still detectable (75). Sensitivity can be improved by increasing TR and TE (47,76).

1.5.2 Cellular Imaging of Immune Cells

Natural killer cells have previously been labeled with iron nanoparticles and tracked for immunotherapy applications by three groups. The first study used parental NK-92 cells and NK-92 cells that were stably transfected to express a ligand for the Her2 receptor expressed by some breast cancers (NK-92-scFv(FRP5)- ζ). An orthotopic mouse model of breast cancer using Her2 positive cells was used. The NK cells were labeled with Feridex and Resovist using simple incubation, electroporation and transfection agents; the optimal combination of uptake and cell viability was achieved using Resovist and lipofectamine. Targeted and non-targeted NK-92 were injected IV then the mice were scanned 1 day after administration. The targeted NK-92 were detectable by MRI and histology while the non-targeted NK cells were not (64). In a similar experiment by the same group, NK-92 were transfected to target EpCAM on prostate cancer cells (NK-92-scFv(MOC31)- ζ), labeled with Feridex and Lipofectamine, and then tracked to tumours in a rat model of prostate cancer (77). Another group used MRI to evaluate the delivery of SPIO-labeled NK-92 cells that were injected intra-arterially via a hepatic catheter to treat liver metastases in a rat model (78). More recently, a third group used NK-92-scFv(FRP5)- ζ (targeted to the Her2 receptor) that were labeled with SPIO and liposomes and tracked to a brain metastatic model of breast cancer after the blood-brain barrier was disrupted using focused ultrasound (79). These experiments were conducted at 3T and 7T, using T2* weighted or FFE GE sequences. Similar experiments have used positron emission tomography (PET) and optical imaging to track targeted NK in small animal models of breast and prostate cancer (80,81), as well as single photon emission computed tomography (SPECT) tracking of NK in small human pilot studies (25,82).

MR cell tracking has also been used for detection of other immune cell types. T-cells have been labeled with Feridex using poly-L-lysine and Resovist using liposomes for cancer and central nervous system applications (83-85). Dendritic cells can be labeled

with SPIO or MPIO for monitoring their migration to lymph nodes, although labeling has some functional effects on the DC (54,86-88).

1.5.3 Hyperpolarized Spectroscopy

MRI as described above allows for localization of tissues, tumours or cells. Spectroscopy using hyperpolarized contrast agents provides functional information about tissue metabolism. In 2D chemical shift imaging (CSI), unlike with conventional MR imaging, a spectrum of resonance frequencies is created for each voxel in the field of view. The chemical environment of the nuclei can be determined based on the location of the resonance peaks, because nuclei are exposed to slightly different magnetic fields depending on the configuration of electrons in the molecule (42). Images of this type can be acquired by exciting any MR suitable nucleus. In order to perform CSI for ^{13}C at 3T, an RF coil that can be tuned to either the hydrogen Larmor frequency (127.6 MHz) or the carbon Larmor frequency (32.12 MHz) is used.

One common application of spectroscopy uses substrates involved in cellular energy metabolism. This method incorporates the use of ^{13}C -enriched endogenous compounds. While ^{12}C is the most abundant isotope of carbon (98.9%), it has no nuclear magnetic moment, so it is not visible with MRI. Carbon-13 (^{13}C) has a magnetic moment but its natural abundance is only 1.1%, so compounds must be synthesized that are enriched in ^{13}C . Even with this enrichment, however, the density of ^{13}C nuclei is too low for spectroscopy; even in a 3T magnetic field the amount of polarization is not sufficient (89). This is mainly the result of the smaller nuclear magnetic dipole moment of ^{13}C compounds compared with ^1H . In order to overcome this limitation, ^{13}C compounds are hyperpolarized; this increases the signal by $\geq 10,000$ times (90). Rapid MRSI is used to temporally and spatially map the biodistribution of the hyperpolarized probe and its metabolic products. Only signal from the injected hyperpolarized probe and its metabolites are observed, resulting in a sparse and well-resolved spectrum.

At our site, metabolites enriched in ^{13}C are hyperpolarized using dynamic nuclear polarization (DNP), although other methods exist. Briefly, in this process, the ^{13}C -enriched metabolite is mixed with a trityl radical and cooled to a glass at a very low

temperature in a high magnetic field (3T); the electron spins of the free radical are easily polarized by the magnetic field. The polarization is then transferred to the ^{13}C nuclei by microwave irradiation (90,91). Then the compound is rapidly thawed to body temperature and dissolved in a buffer solution at physiological pH and quickly transported to the magnet for injection into the subject (89,90,92). Many different metabolites can be hyperpolarized, allowing for different aspects of metabolism to be studied. In order to be hyperpolarizable and useful for spectroscopy the molecule must form a glass easily and have a relatively long T_1 in solution at room temperature. One of the first and most commonly ^{13}C -enriched compounds is $[1-^{13}\text{C}]$ pyruvate, which has a T_1 of about 65 s at 3T and is readily polarizable to levels greater than 20% (93).

Pyruvate is important because it is located at a fork in the pathway that metabolizes glucose to adenosine triphosphate (ATP), the molecule use for energy in cells. Glucose is metabolized differently depending on the type and proliferative status of the tissue (Figure 1.6). In non-proliferative tissue, pyruvate is converted to AcetylCo-A by the enzyme pyruvate dehydrogenase and enters the citric acid cycle, which is the most efficient way to convert glucose to ATP but requires oxygen. However, in tumours, metabolism tends to be through the process of aerobic glycolysis, which begins with the conversion of pyruvate to lactate through the action of the enzyme lactate dehydrogenase. This is called the Warburg effect and has been observed in multiple tumour types and is a hallmark of cancer (94) although the precise reason that tumours use a less-efficient ATP production pathway is not fully understood (95).

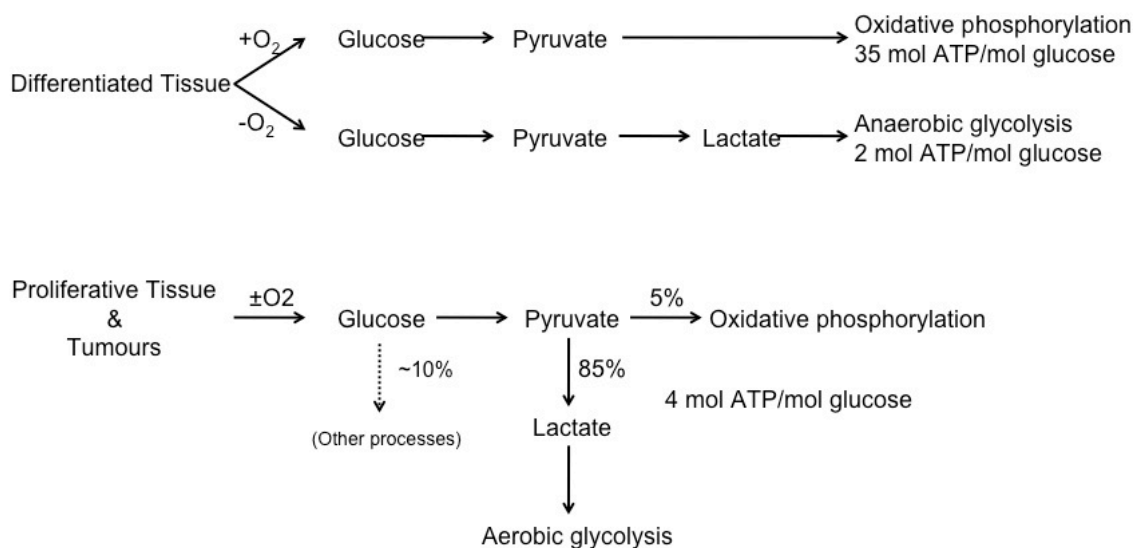


Figure 1.6: Metabolic fate of pyruvate changes depending on tissue type and proliferation.

In oxygenated differentiated tissue, glucose is metabolized through oxidative phosphorylation (citric acid cycle), which produces the most ATP of the three pathways. In deoxygenated differentiated tissue, pyruvate is instead converted to lactate and then undergoes anaerobic glycolysis. In proliferative tissue and tumours, glucose is primarily metabolized through glycolysis with or without the presence of oxygen. Adapted from (95).

In this thesis, pyruvate labeled at the first carbon is used [$1\text{-}^{13}\text{C}$]pyruvate; this is converted by the enzyme lactate dehydrogenase to [$1\text{-}^{13}\text{C}$]lactate inside the cell. The observed signal for [$1\text{-}^{13}\text{C}$]pyruvate is a single peak at 171 ppm and for [$1\text{-}^{13}\text{C}$]lactate is at 183 ppm. For each voxel, the ratio of the area under the lactate and pyruvate peaks is used to determine the relative amounts of lactate and pyruvate. Using a ratiometric approach compensates for differences in injection volume or polarization between samples and allows for comparison between experiments. An increased ratio of lactate to pyruvate indicates that the tissue is using aerobic or anaerobic glycolysis instead of the citric acid cycle as an energy source, and thus identifies tumours.

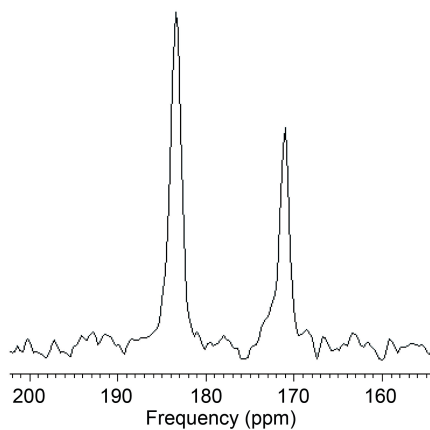


Figure 1.7: Sample lactate and pyruvate spectrum.

The lactate peak is located at 183 ppm and the pyruvate peak at 171 ppm. In this spectrum acquired at 3T in a mouse with a prostate tumour, the area under the lactate peak is larger than that under the pyruvate peak.

[1-¹³C]pyruvate spectroscopy has been used in mouse models of prostate cancer to grade tumours and to locate metastases, and to monitor response to treatment in models of lymphoma, glioma and breast cancer (96-99). In humans, it is under study in prostate cancer patients ((100), [clinicaltrials.gov NCT01229618](https://clinicaltrials.gov/ct2/show/study/NCT01229618)). Non-cancer applications include cardiac function and inflammation due to radiation-induced lung injury and arthritis (92,101-103).

1.6 Model

The cancer model in this thesis is PC-3M cells injected either SC or orthotopically in nude mice. These cells express the MIC A/B ligand that binds to the NKG2D activating receptor on NK cells. For the orthotopic model, the prostate was surgically exposed and cells were injected into the left dorsolateral lobe, then the incision was re-sutured and the tumour was allowed to grow for up to 30 days (Figure 1.8).

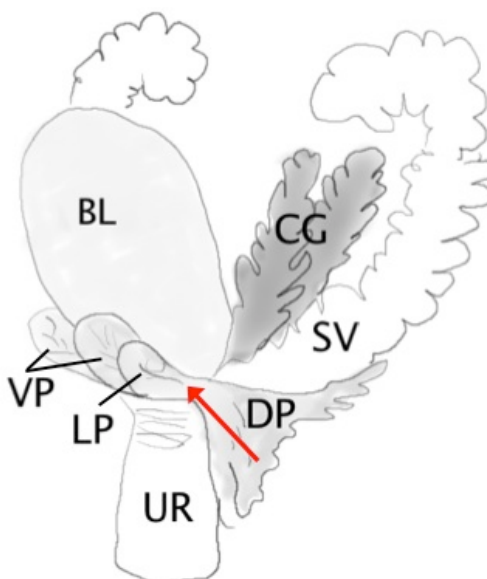


Figure 1.8 The mouse prostate.

Schematic of mouse prostate and surrounding tissues. The injection site used in this model is indicated by the arrow. BL: bladder, VP: ventral prostate, DP: dorsal prostate, SV: seminal vesicles, UR: urethra, CG: coagulating gland (adapted from (104)).

The human NK cell line used is KHYG-1. This cell line was derived from a patient with an NK cell leukemia (22). It has been found to have increased cytotoxicity relative to NK-92 and YT, perhaps because the granzymes in the cytoplasm are constitutively polarized, and thus are primed to release their cytotoxic cargo upon activation (105). KHYG-1 expresses NKG2D and NKp44 among other cytotoxicity receptors (105).

The SPIO used to label the KHYG-1 is MoldayRhodamine, which has a dextran coat and is labeled with a Rhodamine tag for fluorescence microscopy validation (Table 1.1). For the hyperpolarized ^{13}C spectroscopy experiments, $[1-^{13}\text{C}]$ pyruvate was used to examine tumour metabolism.

1.7 Purpose of Thesis

In this thesis we use MRI techniques to track and monitor NK cells and NK cell therapy in a model of prostate cancer. Previous studies by other groups have used MRI and PET to track targeted NK-92 cells to prostate and breast cancer mouse and rat models, but this is the first study to use non-targeted NK cells administered systemically globally, the first to label KHYG-1 NK cells, and the first to administer them *in vivo*. This is also the first administration of $[1-^{13}\text{C}]$ pyruvate spectroscopy in a xenograft model of prostate cancer.

1.7.1 Objectives

- 1- To label KHYG-1 cells with iron oxide nanoparticles
- 2- To use the bSSFP sequence to image the healthy mouse prostate in a reasonable scan time with high SNR and contrast
- 3- To determine if KHYG-1 will accumulate in PC-3M tumours after they are administered to mice bearing tumours
- 4- To use spectroscopic imaging with hyperpolarized carbon-13 MRI to image metabolism in PC-3M tumours and determine sensitivity for monitoring disease and treatment progress

In Chapter 2, iron oxide labeled KHYG-1 NK cells were injected into mice with subcutaneous PC-3M tumours. MRI and histology techniques were used to monitor the accumulation of the NK cells in the tumours. This chapter is derived from two published papers (McFadden C et al, Labeling of multiple cell lines using a new iron oxide agent for cell tracking by MRI. Contrast Media and Molecular Imaging 2011, Nov;6(6):514-22

and Mallett et al, Migration of iron-labeled KHYG-1 natural killer cells to subcutaneous tumors in nude mice, as detected by magnetic resonance imaging. *Cytherapy* 2012, Jul;14(6):743-51) as well as unpublished work.

In Chapter 3, the bSSFP sequence was optimized for use in imaging the mouse prostate. This was published in PLoSOne as: Mallett CL and Foster PJ. Optimization of the balanced steady state free precession (bssfp) pulse sequence for magnetic resonance imaging of the mouse prostate at 3T. *PLoS One* 2011;6(4):e18361.

In Chapter 4, the optimized pulse sequence was used to characterize the growth and metastasis of an orthotopic model for prostate cancer. As well, hyperpolarized ^{13}C spectroscopic imaging was used to probe pyruvate metabolism in the tumours. This work is in preparation for submission to *The Prostate* for consideration for publication.

The appendices include additional results from a longitudinal pilot study of hyperpolarized $[1-^{13}\text{C}]$ pyruvate in mice with prostate tumours treated by direct injection of KHYG-1.

1.8 References

1. Canadian Cancer Society Steering Committee. Canadian cancer statistics 2010.
2. Siegel R, Naishadham D, Jemal A. Cancer statistics, 2012. *CA Cancer J Clin* 2012;62(1):10-29.
3. Murphy K, Travers P, Walport M. Janeway's immunobiology. 7th ed. New York: Garland Science; 2008.
4. Dunn GP, Old LJ, Schreiber RD. The immunobiology of cancer immunosurveillance and immunoediting. *Immunity* 2004, Aug;21(2):137-48.

5. Albertsson PA, Basse PH, Hokland M, Goldfarb RH, Nagelkerke JF, Nannmark U, Kuppen PJK. NK cells and the tumour microenvironment: Implications for nk-cell function and anti-tumour activity. *Trends in Immunology* 2003;24(11):603-9.
6. Sallman DA, Djeu JY. Immunological sculpting: Natural killer cell receptors and ligands . In: Pendergast JC, Jaffee EM, editors. *Cancer Immunotherapy*. Oxford: Elsevier; 2007. p. 63-81.
7. Wu JD, Higgins LM, Steinle A, Cosman D, Haugk K, Plymate SR. Prevalent expression of the immunostimulatory MHC class I chain # x02013; related molecule is counteracted by shedding in prostate cancer. *Journal of Clinical Investigation* 2004;114(4):560.
8. Kalinski P, Mailliard RB, Giermasz A, Zeh HJ, Basse P, Bartlett DL, et al. Natural killer-dendritic cell cross-talk in cancer immunotherapy. *Expert Opin Biol Ther* 2005, Oct;5(10):1303-15.
9. Fernandez NC, Lozier A, Flament C, Ricciardi-Castagnoli P, Bellet D, Suter M, et al. Dendritic cells directly trigger NK cell functions: Cross-talk relevant in innate anti-tumor immune responses in vivo. *Nat Med* 1999, Apr;5(4):405-11.
10. Whiteside TL. The tumor microenvironment and its role in promoting tumor growth. *Oncogene* 2008, Oct 6;27(45):5904-12.
11. Gabrilovich DI, Nagaraj S. Myeloid-derived suppressor cells as regulators of the immune system. *Nat Rev Immunol* 2009, Mar;9(3):162-74.
12. Hoechst B, Voigtlaender T, Ormandy L, Gamrekelashvili J, Zhao F, Wedemeyer H, et al. Myeloid derived suppressor cells inhibit natural killer cells in patients with hepatocellular carcinoma via the nkp30 receptor. *Hepatology* 2009, Sep;50(3):799-807.
13. Mantovani A, Sica A, Allavena P, Garlanda C, Locati M. Tumor-associated macrophages and the related myeloid-derived suppressor cells as a paradigm of the diversity of macrophage activation. *Hum Immunol* 2009, May;70(5):325-30.

14. Blades RA, Keating PJ, McWilliam LJ, George NJR, Stern PL. Loss of HLA class I expression in prostate cancer: Implications for immunotherapy. *Urology* 1995;46(5):681-7.
15. Sznol M, Parkinson DR. Clinical applications of IL-2. *Oncology (Williston Park)* 1994, Jun;8(6):61-7; discussion 67, 71, 74-5.
16. Zaidi MR, Merlino G. The two faces of interferon- γ in cancer. *Clin Cancer Res* 2011, Oct 1;17(19):6118-24.
17. Dranoff G. GM-CSF-secreting melanoma vaccines. *Oncogene* 2003, May 19;22(20):3188-92.
18. Sonpavde G, Kantoff PW. Immunotherapy for castration-resistant prostate cancer. *The Urologic Clinics of North America* 2012;39(4):465-81.
19. Yee C, Thompson JA, Byrd D, Riddell SR, Roche P, Celis E, Greenberg PD. Adoptive T cell therapy using antigen-specific CD8⁺ T cell clones for the treatment of patients with metastatic melanoma: In vivo persistence, migration, and antitumor effect of transferred T cells. *Proc Natl Acad Sci U S A* 2002, Dec 10;99(25):16168-73.
20. Hong JJ, Rosenberg SA, Dudley ME, Yang JC, White DE, Butman JA, Sherry RM. Successful treatment of melanoma brain metastases with adoptive cell therapy. *Clin Cancer Res* 2010, Oct 1;16(19):4892-8.
21. Gong JH, Maki G, Klingemann HG. Characterization of a human cell line (NK-92) with phenotypical and functional characteristics of activated natural killer cells. *Leukemia* 1994, Apr;8(4):652-8.
22. Yagita M, Huang C, Umehara H, Matsuo Y, Tabata R, Miyake M, et al. A novel natural killer cell line (KHYG-1) from a patient with aggressive natural killer cell leukemia carrying a p53 point mutation. *Leukemia* 2000;14(5):922-30.

23. Yodoi J, Teshigawara K, Nikaido T, Fukui K, Noma T, Honjo T, et al. TCGF (IL 2)-receptor inducing factor (s). I. Regulation of IL 2 receptor on a natural killer-like cell line (YT cells). *The Journal of Immunology* 1985;134(3):1623.
24. Miller JS, Soignier Y, Panoskaltsis-Mortari A, McNearney SA, Yun GH, Fautsch SK, et al. Successful adoptive transfer and in vivo expansion of human haploidentical NK cells in patients with cancer. *Blood* 2005, Apr 15;105(8):3051-7.
25. Matera L, Galetto A, Bello M, Baiocco C, Chiappino I, Castellano G, et al. In vivo migration of labeled autologous natural killer cells to liver metastases in patients with colon carcinoma. *J Transl Med* 2006;4:49.
26. Brand JM, Meller B, Von Hof K, Luhm J, Bähre M, Kirchner H, Frohn C. Kinetics and organ distribution of allogeneic natural killer lymphocytes transfused into patients suffering from renal cell carcinoma. *Stem Cells Dev* 2004, Jun;13(3):307-14.
27. Epstein JI, Allsbrook WC, Amin MB, Egevad LL, ISUP Grading Committee. The 2005 international society of urological pathology (ISUP) consensus conference on gleason grading of prostatic carcinoma. *Am J Surg Pathol* 2005, Sep;29(9):1228-42.
28. Pierorazio PM, Walsh PC, Partin AW, Epstein JI. Prognostic gleason grade grouping: Data based on the modified gleason scoring system. *BJU Int* 2013, Apr:n/a.
29. Bubendorf L, Schöpfer A, Wagner U, Sauter G, Moch H, Willi N, et al. Metastatic patterns of prostate cancer: An autopsy study of 1,589 patients. *Human Pathology* 2000, May;31(5):578-83.
30. Kantoff P, Higano CS. Integration of immunotherapy into the management of advanced prostate cancer. *Urol Oncol* 2012;30(5 Suppl):S41-7.
31. Patel PH, Kockler DR. Sipuleucel-T: A vaccine for metastatic, asymptomatic, androgen-independent prostate cancer. *Ann Pharmacother* 2008, Jan;42(1):91-8.

32. Kantoff PW, Higano CS, Shore ND, Berger ER, Small EJ, Penson DF, et al. Sipuleucel-T immunotherapy for castration-resistant prostate cancer. *N Engl J Med* 2010, Jul 23;363(5):411-22.
33. Sakuishi K, Apetoh L, Sullivan JM, Blazar BR, Kuchroo VK, Anderson AC. Targeting tim-3 and PD-1 pathways to reverse T cell exhaustion and restore anti-tumor immunity. *J Exp Med* 2010, Sep 27;207(10):2187-94.
34. Greenberg NM, DeMayo F, Finegold MJ, Medina D, Tilley WD, Aspinall JO, et al. Prostate cancer in a transgenic mouse. *Proceedings of the National Academy of Science USA* 1995, Apr;92(8):3439-43.
35. Irshad S, Abate-Shen C. Modeling prostate cancer in mice: Something old, something new, something premalignant, something metastatic. *Cancer Metastasis Rev* 2012, Nov 1.
36. Croy BA, Linder KE, Yager JA. Primer for non-immunologists on immune-deficient mice and their applications in research. *Comp Med* 2001, Aug;51(4):300-13.
37. Stephenson RA, Dinney CPN, Gohji K, Ordonez NG, Killion JJ, Fidler IJ. Metastatic model for human prostate cancer using orthotopic implantation in nude mice. *JNCI Journal of the National Cancer Institute* 1992;84(12):951.
38. Waters DJ, Janovitz EB, Chan TC. Spontaneous metastasis of PC-3 cells in athymic mice after implantation in orthotopic or ectopic microenvironments. *Prostate* 1995, May;26(5):227-34.
39. Thalmann GN, Sikes RA, Wu TT, Degeorges A, Chang SM, Ozen M, et al. LNCaP progression model of human prostate cancer: Androgen-independence and osseous metastasis. *Prostate* 2000, Jul 1;44(2):91-103 Jul 1;44(2).
40. Kaighn ME, Narayan KS, Ohnuki Y, Lechner JF, Jones LW. Establishment and characterization of a human prostatic carcinoma cell line (PC-3). *Invest Urol* 1979, Jul;17(1):16-23.

41. Kozlowski JM, Fidler IJ, Campbell D, Xu Z, Kaighn ME, Hart IR. Metastatic behavior of human tumor cell lines grown in the nude mouse. *Cancer Res* 1984, Aug;44(8):3522-9.
42. McRobbie DW, Moore EA, Graves MJ, Prince MR. MRI from picture to proton. 2nd ed. Cambridge: Cambridge University Press; 2007.
43. Scheffler K, Lehnhardt S. Principles and applications of balanced SSFP techniques. *Eur Radiol* 2003, Nov;13(11):2409-18.
44. Bangerter NK, Hargreaves BA, Vasanawala SS, Pauly JM, Gold GE, Nishimura DG. Analysis of multiple-acquisition SSFP. *Magn Reson Med* 2004, May;51(5):1038-47.
45. Ribot EJ, Martinez-Santesteban FM, Simeone C, Steeg PS, Chambers AF, Rutt BK, Foster PJ. In vivo single scan detection of both iron-labeled cells and breast cancer metastases in the mouse brain using balanced steady-state free precession imaging at 1.5 T. *J Magn Reson Imaging* 2011, Jul;34(1):231-8.
46. Bernas LM, Foster PJ, Rutt BK. Imaging iron-loaded mouse glioma tumors with bssfp at 3 T. *Magn Reson Med* 2010, Jul;64(1):23-31.
47. Ramadan SS, Heyn C, MacKenzie LT, Chambers AF, Rutt BK, Foster PJ. Ex-vivo cellular MRI with b-ssfp: Quantitative benefits of 3 T over 1.5 T. *Magnetic Resonance Materials in Physics, Biology and Medicine* 2008;21(4):251-9.
48. Anzalone N, Gerevini S, Scotti R, Vezzulli P, Picozzi P. Detection of cerebral metastases on magnetic resonance imaging: Intraindividual comparison of gadobutrol with gadopentetate dimeglumine. *Acta Radiol* 2009, Oct;50(8):933-40.
49. Hentsch A, Aschauer MA, Balzer JO, Brossmann J, Busch HP, Davis K, et al. Gadobutrol-enhanced moving-table magnetic resonance angiography in patients with peripheral vascular disease: A prospective, multi-centre blinded comparison with digital subtraction angiography. *Eur Radiol* 2003, Sep;13(9):2103-14.

50. Rovira A, León A. MR in the diagnosis and monitoring of multiple sclerosis: An overview. *Eur J Radiol* 2008, Sep;67(3):409-14.
51. Shukla-Dave A, Hricak H. Role of MRI in prostate cancer detection. *NMR Biomed* 2013, Mar 13.
52. Chopra T, Kandukurti K, Shah S, Ahmed R, Panesar M. Understanding nephrogenic systemic fibrosis. *Int J Nephrol* 2012;2012:912189.
53. AMAG Pharmaceuticals. Feridex I.V.
[Http://www.amagpharma.com/products/feridex_iv.php](http://www.amagpharma.com/products/feridex_iv.php) 2013.
54. Rohani R, de Chickera SN, Willert C, Chen Y, Dekaban GA, Foster PJ. In vivo cellular MRI of dendritic cell migration using micrometer-sized iron oxide (MPIO) particles. *Mol Imaging Biol* 2011, Aug;13(4):679-94.
55. Shapiro EM, Skrtic S, Koretsky AP. Sizing it up: Cellular MRI using micron-sized iron oxide particles. *Magn Reson Med* 2005, Feb;53(2):329-38.
56. Miyoshi S, Flexman JA, Cross DJ, Maravilla KR, Kim Y, Anzai Y, et al. Transfection of neuroprogenitor cells with iron nanoparticles for magnetic resonance imaging tracking: Cell viability, differentiation, and intracellular localization. *Mol Imaging Biol* 2005;7(4):286-95.
57. Gonzalez-Lara LE, Xu X, Hofstetrova K, Pniak A, Brown A, Foster PJ. In vivo magnetic resonance imaging of spinal cord injury in the mouse. *Journal of Neurotrauma* 2009;26(5):753-62.
58. Korkusuz H, Ulbrich K, Welzel K, Koeberle V, Watcharin W, Bahr U, et al. Transferrin-coated gadolinium nanoparticles as MRI contrast agent. *Mol Imaging Biol* 2013, Apr;15(2):148-54.
59. Srinivas M, Boehm-Sturm P, Figdor CG, de Vries IJ, Hoehn M. Labeling cells for in vivo tracking using (19)F MRI. *Biomaterials* 2012, Dec;33(34):8830-40.

60. Cohen B, Dafni H, Meir G, Harmelin A, Neeman M. Ferritin as an endogenous MRI reporter for noninvasive imaging of gene expression in C6 glioma tumors. *Neoplasia* 2005, Feb;7(2):109-17.
61. Zurkiya O, Chan AW, Hu X. MagA is sufficient for producing magnetic nanoparticles in mammalian cells, making it an MRI reporter. *Magn Reson Med* 2008, Jun;59(6):1225-31.
62. Weissleder R, Stark DD, Engelstad BL, Bacon BR, Compton CC, White DL, et al. Superparamagnetic iron oxide: Pharmacokinetics and toxicity. *American Journal of Roentgenology* 1989, Jan;152(1):167-3.
63. Hinds KA, Hill JM, Shapiro EM, Laukkanen MO, Silva AC, Combs CA, et al. Highly efficient endosomal labeling of progenitor and stem cells with large magnetic particles allows magnetic resonance imaging of single cells. *Blood* 2003, Aug 1;102(3):867-72.
64. Daldrup-Link HE, Meier R, Rudelius M, Piontek G, Piert M, Metz S, et al. In vivo tracking of genetically engineered, anti-her2/neu directed natural killer cells to HER2/neu positive mammary tumors with magnetic resonance imaging. *Eur Radiol* 2005, Jan;15(1):4-13.
65. BioPAL. Relaxation values for biopal products. [www.biopal.com/images/relaxation Values for Biopal Products.pdf](http://www.biopal.com/images/relaxation%20Values%20for%20Biopal%20Products.pdf) 2013, Mar 19.
66. Weinstein JS, Varallyay CG, Dosa E, Gahramanov S, Hamilton B, Rooney WD, et al. Superparamagnetic iron oxide nanoparticles: Diagnostic magnetic resonance imaging and potential therapeutic applications in neurooncology and central nervous system inflammatory pathologies, a review. *J Cereb Blood Flow Metab* 2010, Jan;30(1):15-35.
67. Szpak A, Kania G, Skórka T, Tokarz W, Zapotoczny S, Nowakowska M. Stable aqueous dispersion of superparamagnetic iron oxide nanoparticles protected by charged chitosan derivatives. *J Nanopart Res* 2013, Jan;15(1):1372.
68. Hillaireau H, Couvreur P. Nanocarriers' entry into the cell: Relevance to drug delivery. *Cell Mol Life Sci* 2009, Sep;66(17):2873-96.

69. Yang CY, Tai MF, Lin CP, Lu CW, Wang JL, Hsiao JK, Liu HM. Mechanism of cellular uptake and impact of ferucarbotran on macrophage physiology. *PLoS One* 2011;6(9):e25524.
70. Thorek DL, Tsourkas A. Size, charge and concentration dependent uptake of iron oxide particles by non-phagocytic cells. *Biomaterials* 2008, Sep;29(26):3583-90.
71. Janic B, Rad AM, Jordan EK, Iskander AS, Ali MM, Varma NR, et al. Optimization and validation of fepro cell labeling method. *PLoS One* 2009;4(6):e5873.
72. Walczak P, Kedziorek DA, Gilad AA, Lin S, Bulte JW. Instant MR labeling of stem cells using magnetoelectroporation. *Magn Reson Med* 2005, Oct;54(4):769-74.
73. Siegers GM, Ribot EJ, Keating A, Foster PJ. Extensive expansion of primary human gamma delta T cells generates cytotoxic effector memory cells that can be labeled with feraheme for cellular MRI. *Cancer Immunol Immunother* 2013, Mar;62(3):571-83.
74. de Vries IJ, Lesterhuis WJ, Barentsz JO, Verdijk P, van Krieken JH, Boerman OC, et al. Magnetic resonance tracking of dendritic cells in melanoma patients for monitoring of cellular therapy. *Nat Biotechnol* 2005, Nov;23(11):1407-13.
75. Heyn C, Bowen CV, Rutt BK, Foster PJ. Detection threshold of single spio-labeled cells with FIESTA. *Magnetic Resonance in Medicine* 2005;53(2):312-20.
76. Ribot EJ, Martinez-Santesteban FM, Simeone C, Steeg PS, Chambers AF, Rutt BK, Foster PJ. In vivo single scan detection of both iron-labeled cells and breast cancer metastases in the mouse brain using balanced steady-state free precession imaging at 1.5 T. *J Magn Reson Imaging* 2011, Jul;34(1):231-8.
77. Meier R, Golovko D, Tavri S, Henning TD, Knopp C, Piontek G, et al. Depicting adoptive immunotherapy for prostate cancer in an animal model with magnetic resonance imaging. *Magn Reson Med* 2011, Mar;65(3):756-63.

78. Sheu AY, Zhang Z, Omary RA, Larson AC. MRI-Monitored transcatheter intra-arterial delivery of spio-labeled natural killer cells to hepatocellular carcinoma: Preclinical studies in a rodent model. *Invest Radiol* 2012, Dec 14.
79. Alkins RD, Burgess A, Ganguly M, Francia G, Kerbel RS, Wels WS, Hynynen K. Focused ultrasound delivers targeted immune cells to metastatic brain tumors. *Cancer Res* 2013, Jan 9.
80. Meier R, Piert M, Piontek G, Rudelius M, Oostendorp RA, Senekowitsch-Schmidtke R, et al. Tracking of [18F]fdg-labeled natural killer cells to HER2/neu-positive tumors. *Nucl Med Biol* 2008, Jul;35(5):579-88.
81. Tavri S, Jha P, Meier R, Henning TD, Müller T, Hostetter D, et al. Optical imaging of cellular immunotherapy against prostate cancer. *Mol Imaging* 2009;8(1):15-26.
82. Meller B, Frohn C, Brand JM, Lauer I, Schelper LF, von Hof K, et al. Monitoring of a new approach of immunotherapy with allogenic (111)in-labelled NK cells in patients with renal cell carcinoma. *Eur J Nucl Med Mol Imaging* 2004, Mar;31(3):403-7.
83. Berger C, Rausch M, Schmidt P, Rudin M. Feasibility and limits of magnetically labeling primary cultured rat T cells with ferumoxides coupled with commonly used transfection agents. *Mol Imaging* 2006;5(2):93-104.
84. Beer AJ, Holzapfel K, Neudorfer J, Piontek G, Settles M, Krönig H, et al. Visualization of antigen-specific human cytotoxic T lymphocytes labeled with superparamagnetic iron-oxide particles. *Eur Radiol* 2008, Jun;18(6):1087-95.
85. Anderson SA, Shukaliak-Quandt J, Jordan EK, Arbab AS, Martin R, McFarland H, Frank JA. Magnetic resonance imaging of labeled t-cells in a mouse model of multiple sclerosis. *Ann Neurol* 2004, May;55(5):654-9.
86. Baumjohann D, Hess A, Budinsky L, Brune K, Schuler G, Lutz MB. In vivo magnetic resonance imaging of dendritic cell migration into the draining lymph nodes of mice. *Eur J Immunol* 2006, Sep;36(9):2544-55.

87. de Chickera S, Willert C, Mallet C, Foley R, Foster P, Dekaban GA. Cellular MRI as a suitable, sensitive non-invasive modality for correlating in vivo migratory efficiencies of different dendritic cell populations with subsequent immunological outcomes. *Int Immunol* 2012, Jan;24(1):29-41.
88. de Chickera SN, Snir J, Willert C, Rohani R, Foley R, Foster PJ, Dekaban GA. Labelling dendritic cells with SPIO has implications for their subsequent in vivo migration as assessed with cellular MRI. *Contrast Media Mol Imaging* 2011;6(4):314-27.
89. Kurhanewicz J, Vigneron DB, Brindle K, Chekmenev EY, Comment A, Cunningham CH, et al. Analysis of cancer metabolism by imaging hyperpolarized nuclei: Prospects for translation to clinical research. *Neoplasia* 2011, Feb;13(2):81-97.
90. Ardenkjaer-Larsen JH, Fridlund B, Gram A, Hansson G, Hansson L, Lerche MH, et al. Increase in signal-to-noise ratio of > 10,000 times in liquid-state NMR. *Proc Natl Acad Sci U S A* 2003, Sep 2;100(18):10158-63.
91. Månsson S, Johansson E, Magnusson P, Chai CM, Hansson G, Petersson JS, et al. ¹³C imaging-a new diagnostic platform. *Eur Radiol* 2006, Jan;16(1):57-67.
92. Thind K, Chen A, Friesen-Waldner L, Ouriadov A, Scholl TJ, Fox M, et al. Detection of radiation-induced lung injury using hyperpolarized (¹³) C magnetic resonance spectroscopy and imaging. *Magn Reson Med* 2012, Oct 16.
93. Schroeder MA, Clarke K, Neubauer S, Tyler DJ. Hyperpolarized magnetic resonance: A novel technique for the in vivo assessment of cardiovascular disease. *Circulation* 2011, Oct 4;124(14):1580-94.
94. Hanahan D, Weinberg RA. Hallmarks of cancer: The next generation. *Cell* 2011, Mar 4;144(5):646-74.
95. Vander Heiden MG, Cantley LC, Thompson CB. Understanding the warburg effect: The metabolic requirements of cell proliferation. *Science* 2009, May 22;324(5930):1029-33.

96. Albers MJ, Bok R, Chen AP, Cunningham CH, Zierhut ML, Zhang VY, et al. Hyperpolarized ¹³C lactate, pyruvate, and alanine: Noninvasive biomarkers for prostate cancer detection and grading. *Cancer Res* 2008, Oct 15;68(20):8607-15.
97. Parkin DM, Bray F, Ferlay J, Pisani P. Global cancer statistics, 2002. *CA Cancer J Clin* 2005;55(2):74-108.
98. Chen AP, Chu W, Gu YP, Cunningham CH. Probing early tumor response to radiation therapy using hyperpolarized [1-(¹³C)]pyruvate in MDA-MB-231 xenografts. *PLoS One* 2013;8(2):e56551.
99. Day SE, Kettunen MI, Gallagher FA, Hu DE, Lerche M, Wolber J, et al. Detecting tumor response to treatment using hyperpolarized ¹³C magnetic resonance imaging and spectroscopy. *Nat Med* 2007, Nov;13(11):1382-7.
100. Harzstark AL, Weinberg VK, Grycz K, Hurd RE, Ardenkjaer-Larsen JH, Murray J, et al. A first-in-human phase I imaging study using hyperpolarized ¹³C-pyruvate (h-py) in patients (pts) with localized prostate cancer (l-pca) (abstract). *ASCO Meeting Abstracts* 30(15S):4600.
101. Månsson S, Petersson JS, Scheffler K. Fast metabolite mapping in the pig heart after injection of hyperpolarized ¹³C-pyruvate with low-flip angle balanced steady-state free precession imaging. *Magn Reson Med* 2012, Dec;68(6):1894-9.
102. Larson PE, Gold GE. Science to practice: Can inflammatory arthritis be monitored by using MR imaging with injected hyperpolarized ¹³C-pyruvate? *Radiology* 2011, May;259(2):309-10.
103. MacKenzie JD, Yen YF, Mayer D, Tropp JS, Hurd RE, Spielman DM. Detection of inflammatory arthritis by using hyperpolarized ¹³C-pyruvate with MR imaging and spectroscopy. *Radiology* 2011, May;259(2):414-20.
104. Sugimura Y, Cunha GR, Donjacour AA. Morphogenesis of ductal networks in the mouse prostate. *Biol Reprod* 1986, Jun;34(5):961-71.

105. Suck G, Branch DR, Smyth MJ, Miller RG, Vergidis J, Fahim S, Keating A. KHYG-1, a model for the study of enhanced natural killer cell cytotoxicity. *Exp Hematol* 2005, Oct;33(10):1160-71.

Chapter 2

2 Labeling of KHYG-1 with Molday-Rhodamine and MRI of Migration to Subcutaneous PC-3M Tumours in Nude Mice*

2.1 Introduction

Natural killer cells (NK) are a potential immunotherapy for both solid tumours and blood-borne malignancies (1-6). NK cells kill target cells by recognizing inhibitory and activating receptors on the target cell surface, without a need for prior antigen sensitization (7). Upon recognition of target cells, NK release granules containing perforins and granzymes that trigger apoptosis in the target cells. Killing can also result from the release of death ligands such as tumour necrosis factor (TNF) (8). Prostate cancer is the most common non-melanoma cancer in Canadian men (9). In this pilot study, we investigate the use of magnetic resonance imaging (MRI) to track KHYG-1 NK cells in a mouse model of prostate cancer.

Several avenues of NK cell therapy are possible, including *in vivo* and/or *ex vivo* expansion of patient or donor NK cells (eg (3,10)) or administration of cytotoxic cell lines (eg (4)). Cytotoxic cell lines (such as NK-92, YT, NKL, KHYG-1 and NKG) (11-15) can be expanded *ex vivo* in compliance with GMP (16) and have the advantage of expressing a different receptor repertoire than the patient's own NK cells, which have already allowed immune evasion of the tumour cells. In Phase I/II clinical trials, NK cell therapy has been found to be non-toxic in patients with a variety of solid tumours including neuroblastoma, renal cell cancer, melanoma, non-small cell lung cancer, breast cancer and ovarian cancer (2-5). Adverse events such as lymphopenia and fever are related to the preparatory myeloablative therapy (eg high doses of cyclophosphamide and

* This chapter contains material from previously published work as well as unpublished data. The papers are: Mallett CL et al (2012) *Migration of iron-labeled KHYG-1 natural killer cells to subcutaneous tumors in nude mice, as detected by magnetic resonance imaging* *Cytotherapy* **14**:6, 743-51, and McFadden C et al (2011) *Labeling of multiple cell lines using a new iron oxide agent for cell tracking by MRI* *Contrast Media and Molecular Imaging* **6**:6, 514-522.

fludarabine) and IL-2 administered to allow for *in vivo* expansion of the transplanted cells (3); some success has been achieved when the myeloablative therapy is not performed but more work is needed (5).

Despite these studies, there are currently unanswered questions about the fate of NK cells after therapy, including the timing of their homing to tumours and their activity once the tumour has been reached (17). Cell distribution and fate have been examined in humans using nuclear medicine techniques (1,18). Proliferation of transplanted allogenic NK cells can be quantified by measuring donor chimerism in the peripheral circulation (3,6). Animal models have been used in imaging studies to examine homing to tumours in a variety of solid tumour models using nuclear medicine, optical imaging, fluorescence and magnetic resonance imaging (MRI) (19-25).

Of these imaging modalities, MRI is a non-irradiative and non-invasive method of cell tracking that has potential for clinical translation. Cells are labeled *in vitro* with a superparamagnetic iron oxide contrast agent and then administered to the animal. The iron oxide causes susceptibility artifacts, which appear as signal voids in the image. Single cells have been detected using this method (26-28), although it is more common to track the accumulation of larger numbers of cells, including cancer cells, stem cells, and macrophages in a target tissue (29-32).

In this study we have used the KHYG-1 NK cell line, which was established from a human NK cell leukemia (14) and has enhanced *in vitro* cytotoxicity toward the leukemia cell line K562 compared to other NK cell lines NK-92 and YT (33). The purpose of this study was to use cellular MRI and histology to monitor accumulation of KHYG-1 NK cells in prostate tumours, comparing three routes of administration. We established subcutaneous tumours in nude mice using the human prostate cancer cell line PC-3M (34) and injected KHYG-1 cells labeled with an iron oxide contrast agent, MoldayION RhodamineB. Tumour size and appearance and presence of NK cells were measured by MRI, using the iron-sensitive and SNR efficient bSSFP sequence, and by histology. Next, KHYG-1 were directly administered to subcutaneous (SC) tumours to determine if there

would be a treatment effect. To the best of our knowledge, this was the first report of *in vivo* administration of KHYG-1 NK cells.

2.2 Methods

2.2.1 Cell Culture

PC-3M cells (NCI, Frederick, MD) were cultured in RPMI-1640 supplemented with 10% fetal bovine serum (FBS). KHYG-1 (gift from Dr. Armand Keating, Princess Margaret Hospital, Toronto, Canada) were cultured in RPMI supplemented with 10% FBS and 100 IU of IL-2 per 500 mL (Proleukin, Novartis, Dorval, QC, Canada). All cells were maintained at 37°C and 5% CO₂.

2.2.2 KHYG-1 Labeling with Iron Oxide Nanoparticle

KHYG-1 were labeled with MoldayION-RhodamineB (BioPal, Worcester, MA, USA), which is considered an ultra-small superparamagnetic iron oxide (USPIO) and has a colloidal diameter of 35 nm, with relaxivity values of $r_1 = 30.4 \text{ mM}^{-1}\text{s}^{-1}$ and $r_2 = 75.8 \text{ mM}^{-1}\text{s}^{-1}$ (35). Labeling was achieved by co-incubating the cells at a concentration of $2 \times 10^6/\text{mL}$ with MoldayION RhodamineB at a concentration of 50 $\mu\text{g Fe/mL}$ for 24 hours, in a 75-cm² flask or 6-well plate depending on the quantity of cells required. Cells were washed 3 times in HBSS after harvest. Cell suspensions were spun onto slides for staining with Perls' Prussian Blue, and cell labeling efficiency was calculated by counting labeled and unlabeled cells in random fields of view from different batches of labeled cells. Cell viability was measured using trypan blue exclusion and using a flow-cytometry assay to measure expression of annexinV and 7AAD. For this assay, cells were washed three times in 5ml HBSS and then treated with 0.25% trypsin-EDTA. An equal volume of media was added and the suspension was centrifuged for 5 minutes. The cell pellet was washed once with 5 ml of HBSS and spun for 5 minutes. The pellet was then washed once with Annexin V binding buffer and then counted. Approximately 1×10^6 cells were treated with 7-AAD and/or Annexin V for 15 min and then put through a cell strainer with 400 μl of binding buffer to remove clumped cells from the working

suspension. Data was acquired using a BD FACSCalibur flow cytometer (BD BioScience, USA) and then analyzed using Flowjo software.

2.2.3 Electron Microscopy

Cells were fixed overnight in 2.5% glutaraldehyde in 0.1M sodium cacodylate buffer at 4 °C, washed in 0.1 M sodium cacodylate buffer, post-fixed in 1% osmium tetroxide in 0.1 M cacodylate buffer for 1 h, washed in the buffer and enrobed in noble agar. After washing in distilled water, they were stained in 2% uranyl acetate for 2 h, dehydrated in a graded series of ethanols, cleared in propylene oxide and embedded in Epon 812 resin. Sections of 60–90 nm were mounted on 300 mesh formvar–carbon coated copper grids, stained with 2% uranyl acetate followed by lead citrate, and viewed in a Philips 410 transmission electron microscope.

2.2.4 Cytotoxicity Assay

The toxicity of the labeled and unlabeled KHYG-1 cells was tested by measuring cytotoxicity to PC-3M cells *in vitro* using an MTT assay kit (Sigma-Aldrich, Canada). The experiment was performed in triplicate with three wells per condition in each assay. KHYG-1 cells were labeled with Molday as above, with 50 µg/mL of Fe in a six well plate. PC-3M cells were plated at 1.6×10^4 /well in 24 well plates and allowed to adhere overnight. The PC-3M media was aspirated and replaced with media (control wells) and labeled and unlabeled KHYG-1 cells at a KHYG-1:PC-3M ratio of 15:1. After 24 h of co-culture, the KHYG-1 were aspirated and the plates were washed three times with HBSS, then 250µl of PC-3M media was added to each well, with 25 µl of the MTT reagent. The formazen reaction was allowed to proceed for 4 h, then 250 µl of the MTT solubilization solution was added to each well and the plates were incubated overnight. A sample of each well was pipetted into a well of a 96-well plate for reading at 590 and 650 nm (background) to measure the relative number of viable cells. Absorbance was normalized to the absorbance of control wells containing only media (plus the MTT reagents).

2.2.5 *In vivo* tracking experiments

Male nude mice (nu/nu, Charles River Laboratories) aged 6-8 weeks were housed in a specific pathogen free barrier facility. All animal experiments were approved by the Animal Use Subcommittee of the University Council on Animal Care at The University of Western Ontario following the guidelines of the Canadian Council on Animal Care (protocol # 2010-210).

For the subcutaneous tumour model, 2 million PC-3M suspended in 200 μ L of HBSS were injected subcutaneously in the right flank of nude mice at day 0. Control tumours, in mice that did not receive any injection of KHYG-1, were established in the right and left flanks of the mice (6 tumours in 3 mice). On day 8, labeled KHYG-1 were injected either intravenously (IV) (20 million cells in 200 μ L HBSS, 11 mice), intra-peritoneally (IP) (20 million cells in 200 μ L HBSS, 5 mice) or SC in the leg near the tumour (2 million cells in 200 μ L HBSS, 3 mice). One additional mouse received an IV injection of 20 million unlabeled KHYG-1 cells. (Four of twelve mice died shortly after IV administration of KHYG-1, presumably of an embolism in the lungs.) A few modifications to this protocol were used: one of the above mice received 20 million KHYG-1 IP labeled with MoldayCoumarin instead of MoldayRhodamine and one mouse received 40 million KHYG-1 IP labeled with MoldayRhodamine instead of 20 million.

2.2.6 Magnetic Resonance Imaging

MRI scans were performed the day before tumour induction and on days 7, 9 and 12 afterward. Scans were performed on a 3T GE Excite MR750 system using a custom-built high-performance gradient insert with an inner diameter of 17.5 cm, maximum gradient strength of 500 mT/m and peak slew rate of 3,000 T/m/s, and a custom solenoidal whole-mouse body RF coil 4 cm in length and 3 cm in diameter. Mice were anaesthetized with isoflurane (2% in oxygen) and placed supine in the coil with tape applied to stretch the skin over the subcutaneous tumours; warm saline bags were taped near the RF coil to maintain body temperature. Rarely, mice were positioned prone in the RF coil to better position the tumours for imaging. The balanced steady state free precession (bSSFP) sequence was used with the following parameters: field of view 6x6 cm, 200 μ m

isotropic voxels, TR/TE = 4.6/2.3 ms, bandwidth = ± 62.5 kHz, 2 averages, 4 phase cycles (with sum of squares reconstruction), 36 minute scan (called the short TR acquisition for the remainder of the chapter). A second sequence, henceforth called the long TR acquisition, was also tested with the following parameters changed: field of view 5x5 cm, TR/TE=12/6 ms, bandwidth 31.25 kHz, scan time 60 minutes (voxel size, signal averaging and phase cycling were the same as for the short TR sequence).

MR images were analyzed using Osirix version 3.7.1 (36); at each time point, tumours were manually segmented every 100 μm and the volume was calculated using the ROI volume tool.

2.2.7 Direct injection experiment

Six female nude mice were injected on both flanks with PC-3M as above. Six days after tumour cell injection, mice were divided into 2 groups – 3 control mice (6 tumours) and 3 treatment mice (6 tumours); groups were determined to keep volumes as similar as possible. Mice were treated by injecting directly into the tumour either 35 μL saline (control) or 5 million KHYG-1 in 35 μL HBSS (treatment). The treatment group were additionally treated with 25,000 IU of rhIL-2 IP daily for 6 days. For all groups, tumours were measured using calipers and the volume was calculated according to the formula: $V=1/2(L*W^2)$, where L is the long axis of the tumour and W is the short axis (37). Treatment was repeated on day 12.

2.2.8 Histology

For the tracking experiment, mice were sacrificed after imaging at time points ranging from 13-20 days after tumour injection (5-13 days after KHYG-1 administration). Approximately half were perfused with 4% paraformaldehyde (PFA), while the rest were sacrificed by euthanyl injection (as indicated in figure captions). Tumours were removed, preserved in 10% formalin, and then passed through a sucrose gradient (10%-30%) for dehydration and cryoprotection. Tissues were embedded in OCT and frozen sections were cut at a thickness of 16 μm using a cryostat. To detect NK cells, slides were stained with purified mouse antihuman CD56 (NCAM) (1:100 dilution) (BioLegend, San Diego, CA, USA). The secondary antibody was biotinylated donkey anti-mouse IgG (H+L)

(1:500 dilution) (Jackson Immune Research Laboratories, Bar Harbor, ME, USA). Blocking was done with 10% normal goat serum (Cedarlane, Burlington, ON, Canada). The chromophores were DAB (Liquid DAB-Plus substrate kit, Invitrogen, Carlsbad, CA, USA), Alkaline-phosphatase (AP kit, Vector Labs, Burlingame, CA, USA) or StreptAvidin AlexaFluor 488 (Invitrogen, Carlsbad, CA, USA). TUNEL staining was performed using the ApopTag Plus Peroxidase in situ Apoptosis Detection Kit (Chemicon International, Billerica, MA, USA). Perls' Prussian Blue (PPB) staining for iron was performed using a 1:1 solution of 2% HCl and 2% potassium ferrocyanide solution for 30-45 minutes, with nuclear fast red or eosin counterstaining. Slides were examined on a Zeiss Axio Imager microscope (Germany) with a Retiga EXi Digital CCD camera (Q Imaging, Vancouver, BC, Canada).

For the direct injection experiment, mice were sacrificed by euthanyl injection on day 18 after tumour cell injection and the tumours were fixed in formalin for at least 24 hours, then embedded for paraffin sectioning. Sections were stained for CD56 as above with a red indicator and counterstained with hematoxylin. TUNEL staining was performed as above.

2.2.9 Statistics

Statistical analysis was performed using GraphPad Prism version 5.0b (GraphPad, San Diego, CA). The labeled and unlabeled cytotoxicity were compared using a one-way analysis of variance. To measure volume change in the tracking experiment and the direct injection experiment, a two-way analysis of variance was used with Tukey post-hoc tests.

2.3 Results

2.3.1 Cell Labeling and Cytotoxicity

After incubation with MoldayION RhodamineB, KHYG-1 were labeled with high efficiency (Figure 2.1). The label was contained in vacuoles in the cytoplasm as seen in the electron micrograph images. Using both the trypan blue assay and the flow-cytometry annexin 7AAD assay, there was no decrease in viability of the KHYG-1 cells with

labeling, with over 90% viability in all cases. There was no difference in *in vitro* cytotoxicity toward PC-3M cells between labeled and unlabeled cells (Figure 2.2).

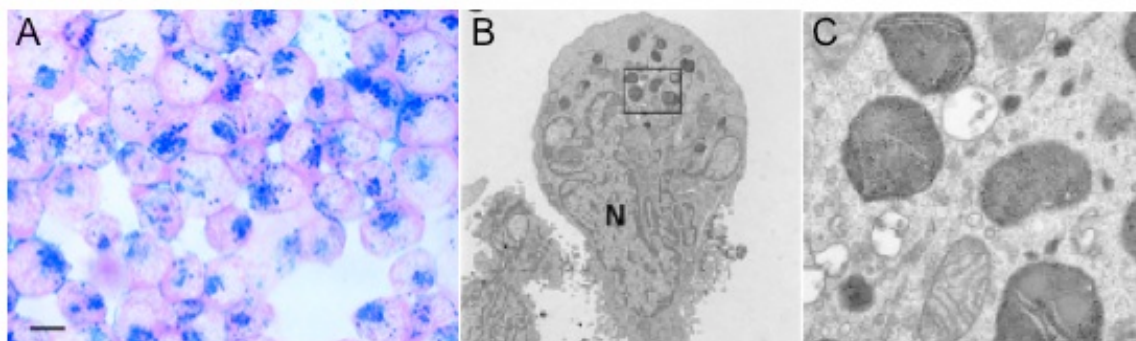


Figure 2.1: KHYG-1 labeling with MoldayION RhodamineB was highly efficient.

A: Cytospin slide stained with Perls' Prussian Blue (for iron) and eosin. Scale bar is 10 μ m. B: Transmission electron micrograph of cell with endosomes visible (6500X). Box is magnified in C (44,500X).

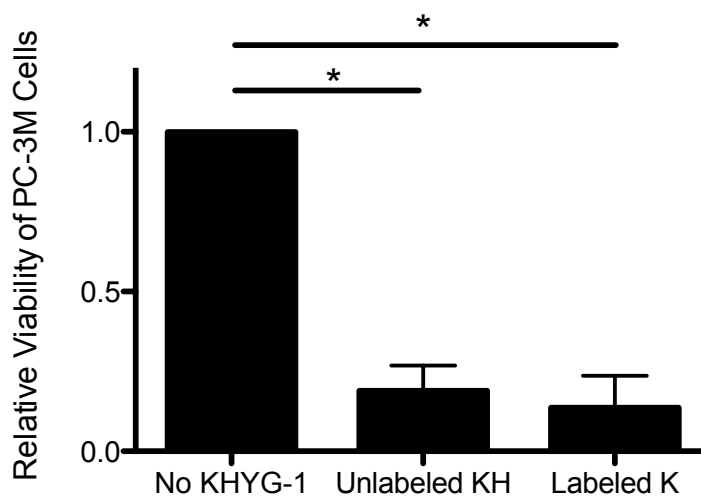


Figure 2.2: Molday labeling did not affect KHYG-1 cytotoxicity to PC-3M cells.

Viability of PC-3M cells in control wells was compared to that of cells co-cultured with unlabeled and labeled KHYG-1 at a ratio of 15:1 KHYG-1: PC-3M. Labeling had no effect on cytotoxicity. Error bars are standard deviation of 3 replicates. * indicates significant difference, $p < 0.01$.

2.3.2 Migration of KHYG-1 to PC-3M Tumours

Tumour sections were stained for CD56 to detect NK cells. KHYG-1 cells were present after each route of administration (Figure 2.3). Following SC administration, there were KHYG-1 in the tumour lobes closest to the site of injection and at the tumour edge (Figure 2.3 A, B). After IV administration there were KHYG-1 in the centre of the tumour (Figure 2.3C, D). There was some heterogeneous accumulation of KHYG-1 after IP administration (Figure 2.3 E, F). The majority of the CD56 positive cells in this section were not stained by the TUNEL reagent, suggesting that there are live NK cells 10 days after administration (Figure 2.3E, F). (The other sections in this panel were not double-stained.) Unlabeled KHYG-1 showed a similar migration to the tumour after IV administration, with accumulation of KHYG-1 in the centre of the tumour, and several CD56 positive, TUNEL negative cells were observed (Figure 2.4). No difference was observed for the KHYG-1 labeled with Molday-Coumarin or for the mouse that received 40 million cells IP.

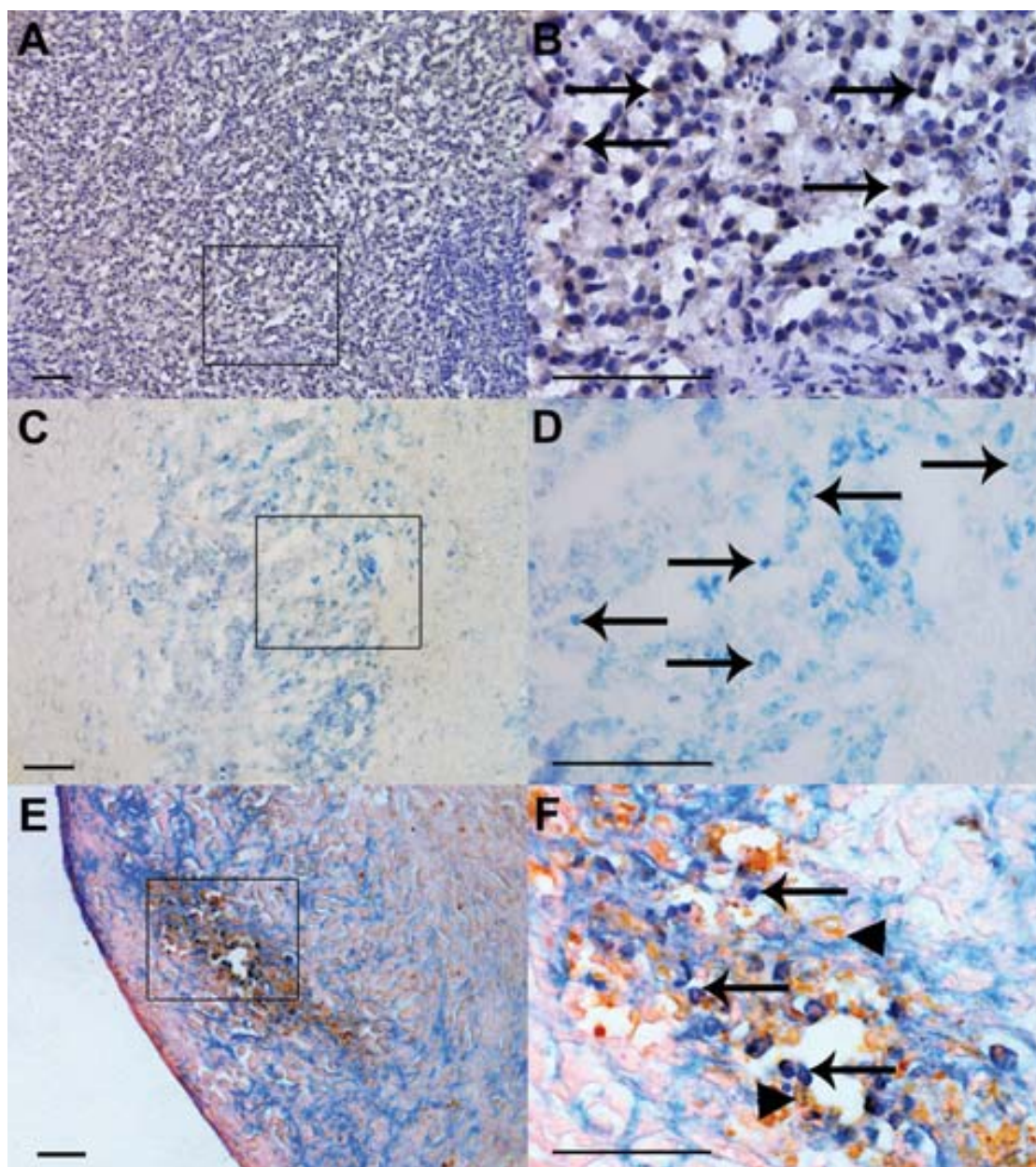


Figure 2.3: KHYG-1 were present in tumours after all routes of administration. A, B: 5 days after subcutaneous injection of 2 million MoldayION RhodamineB-labeled KHYG-1 (non-perfused mouse). Stained with DAB anti-CD56, hematoxylin counterstain; C, D: 5 days after intravenous injection of 20 million MoldayION RhodamineB-labeled KHYG-1 (perfused mouse). Stained with AP anti-CD56; E, F: 12 days after intraperitoneal injection of 20 million MoldayION RhodamineB-labeled KHYG-1 (perfused mouse). Stained with AP anti-CD56, DAB TUNEL, eosin counterstain. Arrows indicate KHYG-1 cells, arrowheads indicate TUNEL positive cells, and boxes indicate magnified regions. Scale bars are 100 μm .

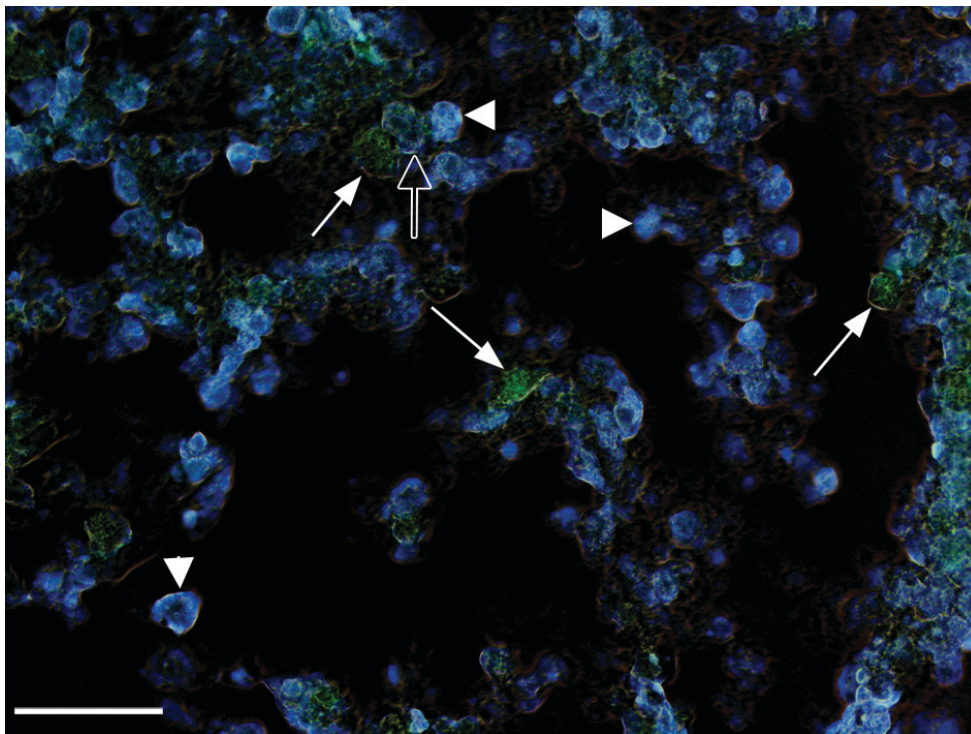


Figure 2.4: There are live NK cells in the tumours.

Overlay of fluorescence and brightfield (with colours inverted) images of a slide stained with anti-CD56 (green) and TUNEL (DAB, colour inverted to white) from a tumour 5 days after IV injection of unlabeled KHYG-1 cells (perfused mouse). KHYG-1 are distributed throughout the tumour (solid arrows). There are many dead cells (arrowheads), but few are CD56 positive (hollow arrow). Scale bar is 50 μm .

2.3.3 *In vivo* Longitudinal MRI

Tumour volumes were measured from the MR images. On day 7 after tumour injection, the mean tumour volume was $10 \pm 11 \text{ mm}^3$ (average of 26/34 tumours). KHYG-1 were administered the following day. At day 12 after tumour injection (4 days after KHYG-1 administration), the average tumour volume was significantly larger than at baseline at $51 \pm 75 \text{ mm}^3$ (average of 27/31 tumours). At both time points, some tumours were not clearly visible in the MR images, due to motion artifact (particularly in the long TR scans), and distortions from the tumours being at the skin-air interface. The volume of these tumours was not measured. There was no difference in volume between treated and

untreated tumours or between the tumours that were treated via different routes of administration (2-way analysis of variance, $p > 0.05$).

Figure 2.5 shows representative MR images (short TR sequence) of a mouse that received a subcutaneous injection of iron-labeled KHYG-1 cells. Figure 2.5A and Figure 2.5B shows images acquired at 24 hours (A) and 4 days (B) post NK injection. A large region of signal loss was observed at the site of injection (arrowheads) at both time points. This area is larger at 24 hours post injection. In Figure 2.5B signal loss appeared along the margin of the tumour and between the lobes. This change in the appearance of the signal void due to KHYG-1 cells implies that the cells have moved over time, migrating toward and into the tumour tissue. These regions of signal loss corresponded to locations that stained strongly for CD56 positive cells (Figure 2.5C, Figure 2.5D). Similarly, a piece of connective tissue that was rhodamine positive was also positive for KHYG-1 (Figure 2.5E, Figure 2.5F).

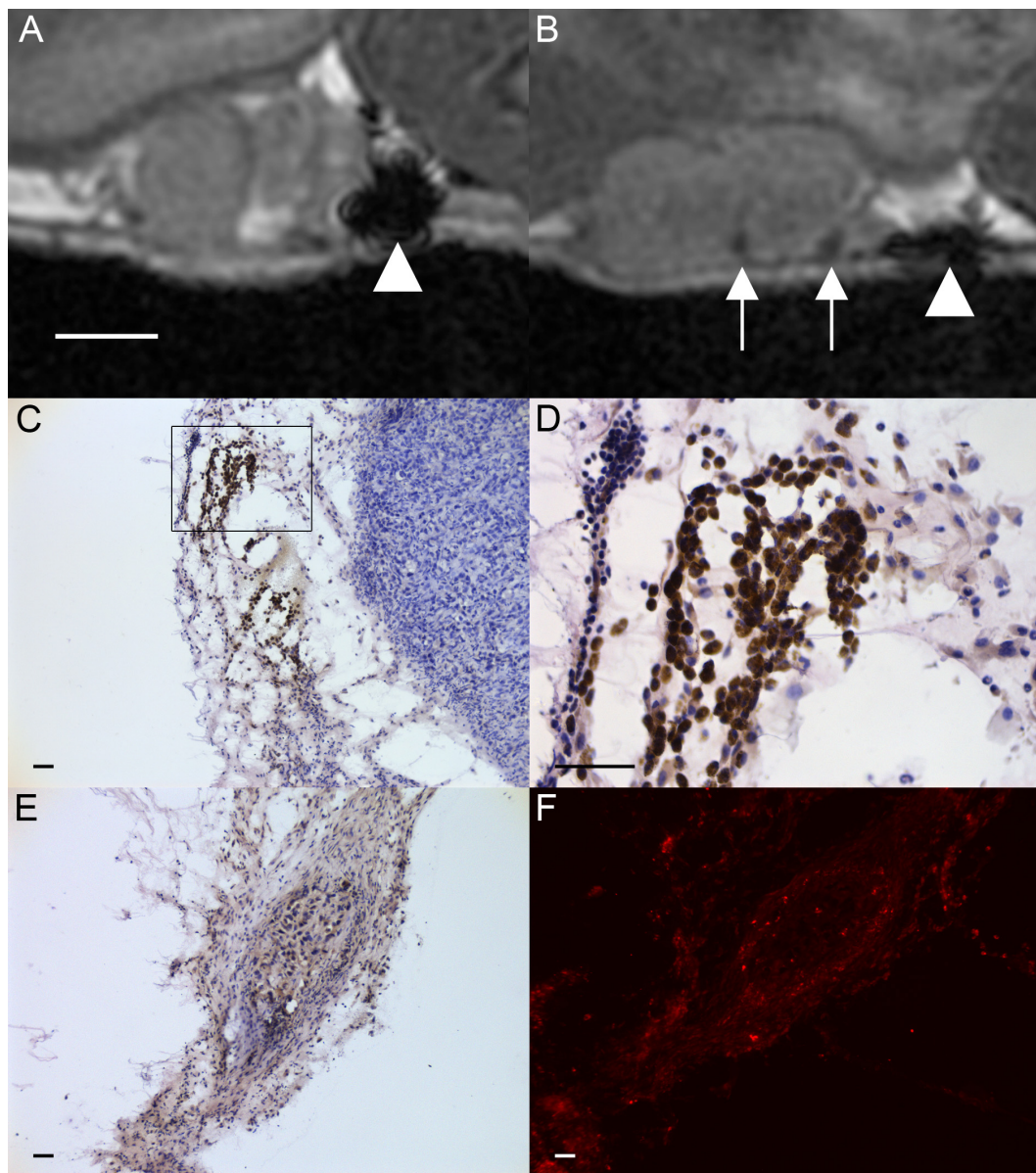


Figure 2.5: Signal loss at edge of tumour after subcutaneous injection of labeled KHYG-1 cells and histological validation of KHYG-1 in tumour margins.

(A) MRI image of centre slice through tumour day 1 after SC KHYG-1 injection (2 million cells). (B) MRI image of centre slice through tumour day 4 after SC KHYG-1 injection. Solid white arrows indicate signal loss at the tumour margins and between tumour lobes. White arrowhead indicates large region of signal loss close to injection site. Anti-CD56 (DAB) staining of the same tumour at 10x (C) and (D) 40x shows accumulation of natural killer cells in tumour margin. Similarly, anti-CD56 staining from connective tissue (E) corresponds to a region of high rhodamine fluorescence in an adjacent section (F). Histology from a tumour 5 days after KHYG-1 injection, non-perfused mouse. Scale bar is 2.5 mm in MR images and 50 μ m in histology images.

Despite the histological confirmation of KHYG-1 in the centre of the tumours as seen in Figure 2.3, there was no change in MR signal from the iron oxide label. For example, Figure 2.6 compares the MR signal (short TR sequence) in mice that received SC and IV KHYG-1. For the tumour that received SC KHYG-1 (Figure 2.6A-B), there were no signal voids in the centre of the tumour 4 days after KHYG-1 administration; however, there was a strong dispersal of rhodamine signal inside the tumour. Similarly, there was no change in the MR appearance of the tumour 4 days after IV administration of labeled KHYG-1, and there was a strong rhodamine signal in the tumour. There was a persistent black spot in the centre of that tumour that is likely due to a blood vessel.

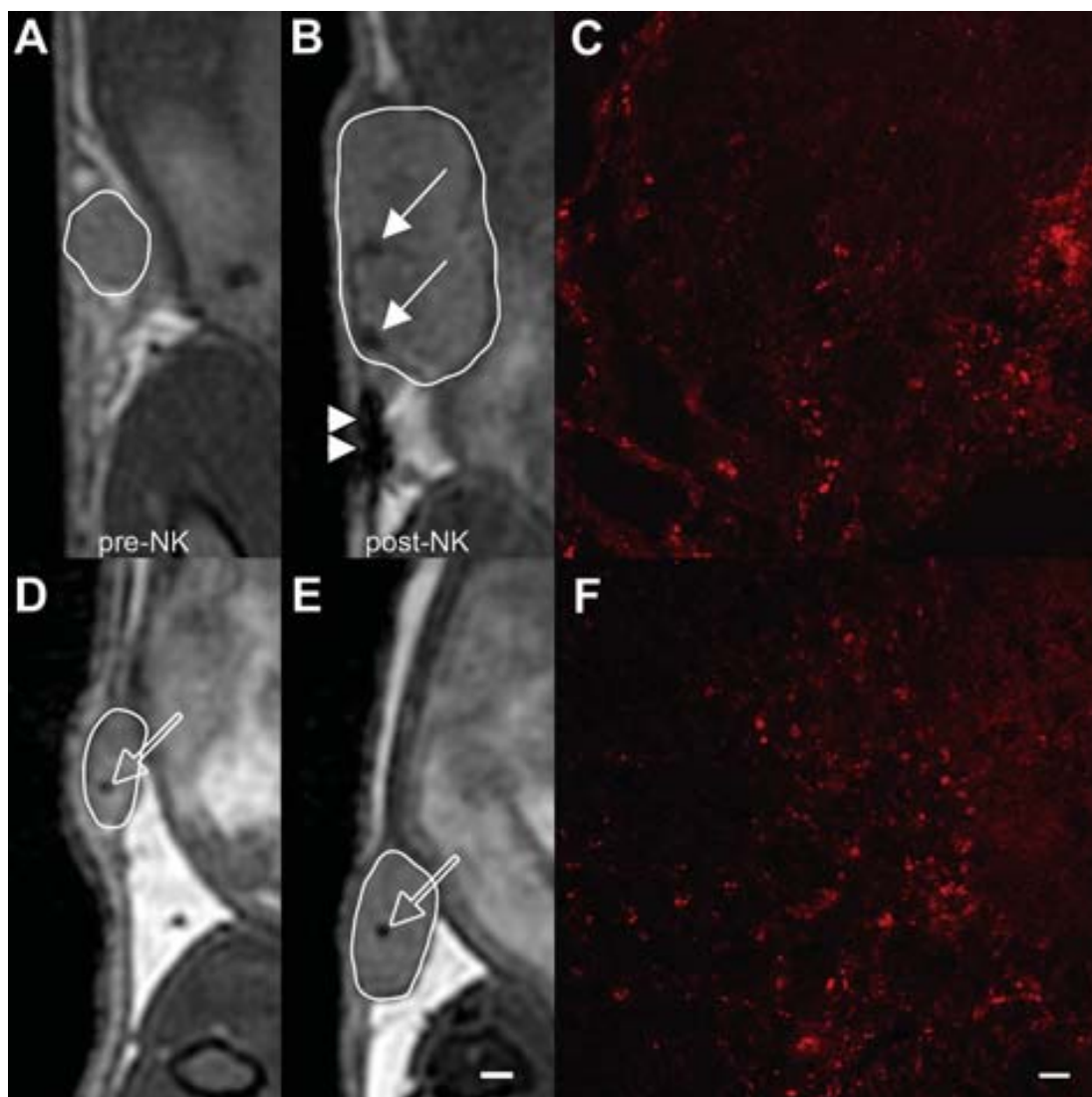


Figure 2.6: Labeled KHYG-1 are in the tumour but not detectable by MRI.

There are no new signal voids in the centre of the tumour 4 days after labeled KHYG-1 administration despite strong rhodamine fluorescence in these tumours from mice that received SC (top row) and IV (bottom row) injections of labeled KHYG-1. A, D: MRI images from the day before KHYG-1 administration; B, E: MRI images from 4 days after KHYG-1 administration; C, F: Rhodamine fluorescence images from the centre of the tumours 5 days after KHYG-1 administration (non-perfused mice). Some signal loss is visible around the edges of tumour that received SC KHYG-1 (B): there is a large void corresponding to the site of injection (arrowheads), and signal loss around the margin of the tumour and between the lobes (solid arrows). There is a persistent spot of signal loss pre- and post-IV administration of KHYG-1 (D, E), likely due to a blood vessel in the tumour (hollow arrows). Magnetic resonance images are from the centre of the tumour at both time points. Scale bar in MR images indicates 2.5 mm, in fluorescence microscopy images indicates 50 μm .

The rhodamine signal in the tumour centre is colocalized with intracellular iron, as determined by a PPB stain. (Figure 2.7) shows a tumour section from a mouse that received labeled KHYG-1 SC. The pattern of rhodamine fluorescence corresponds to the location of iron staining, seen in blue.

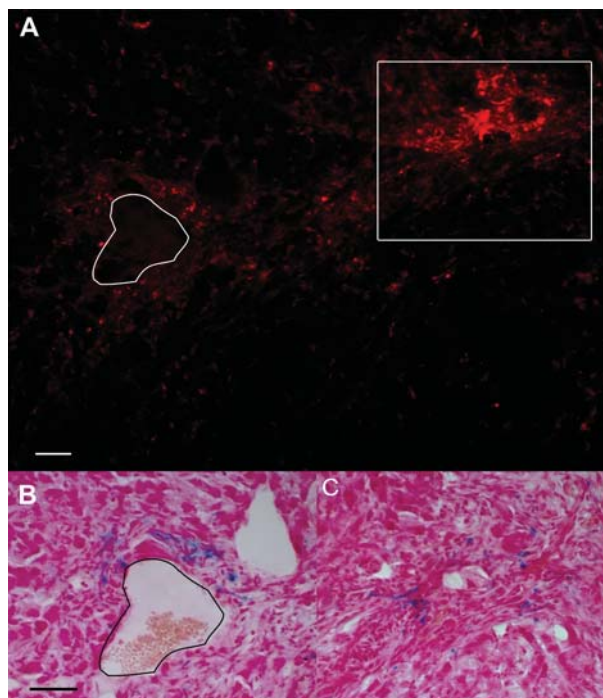


Figure 2.7: Rhodamine and iron are co-localized.

Tissue sections from a mouse that received SC MoldayION RhodamineB-labeled KHYG-1 (non-perfused mouse). A: Rhodamine fluorescence image. In a nearby section stained with PPB, the iron staining matches the rhodamine positive regions. B: Magnified image of the centre-left region including the large blood vessel. C: Magnified image of the region enclosed by the box. Scale bar indicates 50 μm .

2.3.4 Additional MRI Findings

A bSSFP sequence with a long TR was also tested to determine if it was more sensitive to the labeled KHYG-1 cells. In mice that were scanned with both sequences, there was no difference in appearance of the tumour between the two sequences (not shown). Nor was there a difference in the MR appearance of other organs such as the liver and spleen that are also expected to accumulate iron labeled cells, with none of them showing visible

signal loss with either sequence. In several of the tumours from mice that had IV and SC administration of labeled KHYG-1, a pattern of branching signal loss was seen in the centre of the tumour; however, this was also seen in a control tumour, albeit at a lower intensity (Figure 2.8).

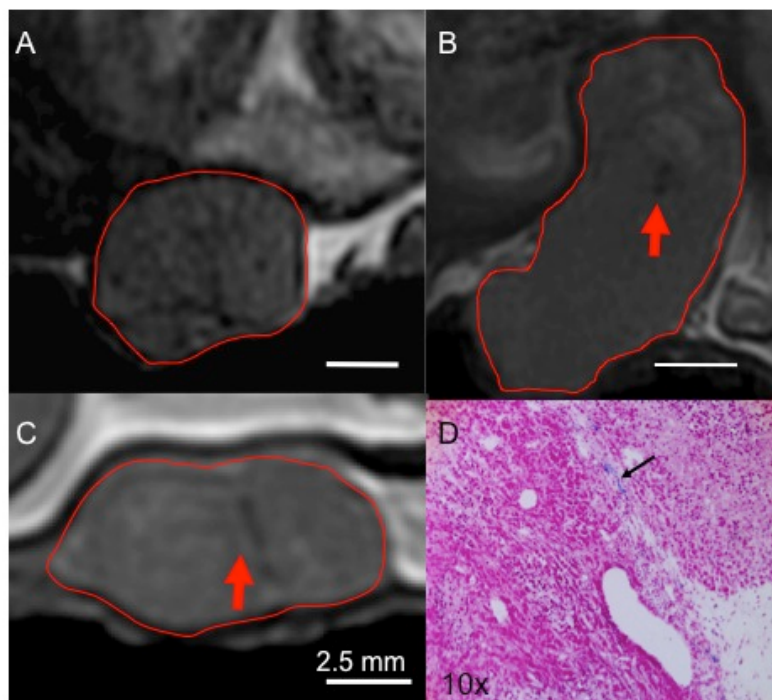


Figure 2.8: Additional MR signal loss patterns.

A: In a tumour from a mouse that received labeled KHYG-1 IV, a branching pattern that appears to correspond to blood vessels is visible. B: In a control tumour, a similar, but fainter branching pattern is seen (red arrow). C: In a tumour from a mouse that received labeled KHYG-1 IP, there is a region of signal loss between the lobes. D: This corresponds to a region in a Perls's stained section that contains iron (indicated by black arrow). Scale bars are 2.5 mm in MR images and section is at 10X magnification. Images acquired with short TR sequence.

2.3.5 Direct Injection Experiment

There was a significant difference in tumour volume between the treated and control tumours starting from day 10 after the treatment began although a trend can be visually identified sooner (Figure 2.9).

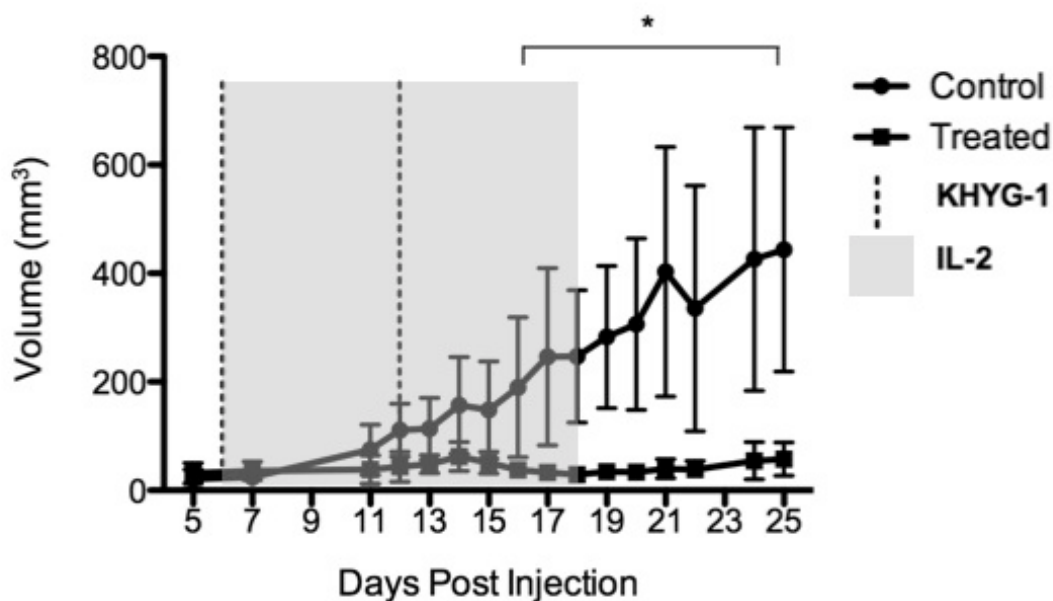


Figure 2.9: Effect of KHYG-1 direct injection on tumour volume.

Tumour volume was measured with calipers. Dashed line indicates intratumoural injection of saline or KHYG-1. Grey box indicates daily IL-2 administration (treated group only). Plotted as average of 6 tumours per group, with standard deviation. * indicates significant difference between groups in a repeated measures analysis of variance ($p < 0.05$).

When the tumours were stained for the presence of NK cells and for apoptosis, the staining showed that there were regions of NK cells in a large group, presumably where they were injected. By day 12 after the start of treatment, the NK cells were dead (Figure 2.10).

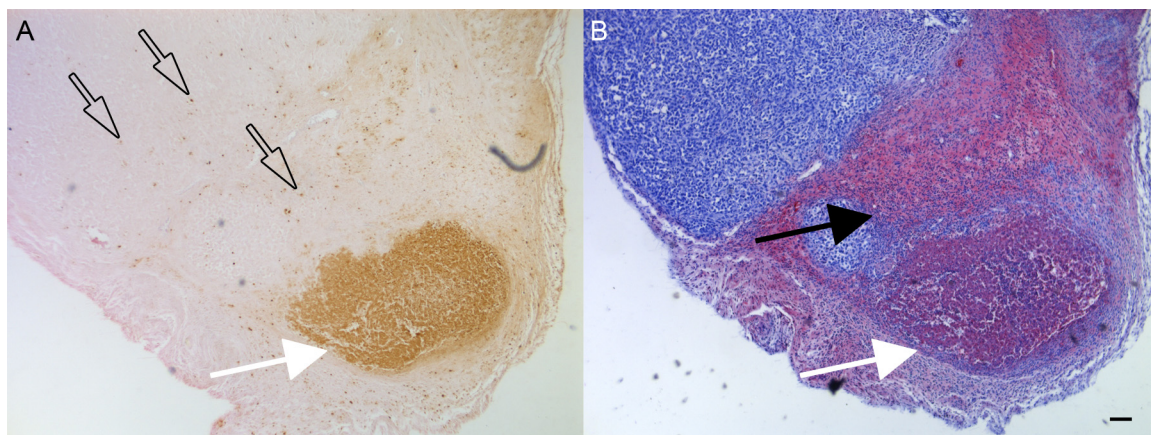


Figure 2.10: Histology of intratumoural injection site.

Section is from 12 days after the start of treatment (d18 of tumour growth). It was stained for dead cells (A) (TUNEL, brown) and for NK cells (B) (anti-CD56 in pink with blue hematoxylin counterstain). There is a large pocket of dead NK cells in the bottom right of the image (solid white arrows), as well as a region that is positive for live NK cells just above the pocket (solid black arrows). The two regions of NK cells may be because there were two separate injections of NK cells. As well, there are scattered dead cells in the rest of the tumour (hollow black arrows). Scale bar is 100 μm .

2.4 Discussion

In this paper we present the first results from a pilot study of administration of the KHYG-1 NK cell line in a mouse model of prostate cancer. KHYG-1 were labeled with MoldayION RhodamineB, an iron oxide contrast agent, for cell tracking with MRI. There was no effect on cell viability or function. KHYG-1 accumulation in a tumour after SC injection was detected using MRI and confirmed with histology. KHYG-1 migration to the tumours after IV and IP injection was confirmed by histology but could not be definitively detected by MRI.

Cytotoxic NK cell lines are under investigation for treatment of a variety of cancers, with some success. A phase I study of NK-92 in renal cell carcinoma and melanoma patients achieved substantial *in vitro* NK-92 expansion, and, although the study was not designed to detect efficacy, there was a transient decrease in tumour size in one of the 12 patients (4). NK-92 increased survival of To-SCID mice when administered IV 3 hours before melanoma cells were injected (16). In a nude mouse model of ovarian cancer, the newly

established NK cell line NKG increased survival time when administered both simultaneously with the cancer cells, and after the tumours were established (15). An additional advantage of cytotoxic NK cells lines compared to ex-vivo expanded donor cells is the ability to modify the cells for targeting. NK-92 cells have been transfected to target specific tumour antigens, including CD20 on B cell malignancies, EpCAM on prostate cancers and HER2 on breast cancers (21,22,38). As well, NK-92 can be modified to be IL-2 independent (16). No IL-2 was administered in our study, which likely affected the toxicity of the cells, although NK-92 retain about 10% of their cytotoxicity 3 days after IL-2 withdrawal (12).

These genetic modifications could also be applied to the KHYG-1 cell line for application as a human cancer immunotherapy. KHYG-1 is a relatively new NK cell line (14), and is of interest as a cancer immunotherapy because of higher *in vitro* cytotoxic potential against several leukemia cell lines than NK-92 (33). This has been attributed in part to constitutive activation of the ERK2 promoter, a key kinase in the release of granzymes, which results in increased activation of KHYG-1 relative to the NK cell lines YT and NK-92 (33). KHYG-1 appears to be cytotoxic via the granzyme M/perforin pathway, in contrast to the granzyme B pathway employed by NK-92; this may allow KHYG-1 to target cells that escape toxicity from the granzyme B pathway (33). In addition, KHYG-1 has an increased expression of the activating NKG2D receptor compared to NK-92 (33). KHYG-1 maintain their cytotoxicity after administration of 10 Gray of radiation, so that they could be adoptively transferred without the risk of engraftment in patients (39). PC-3M, which were used as the target cell line in this work, are a metastatic variant of the PC-3 cell line, which expresses altered major histocompatibility complex class I chain related molecules (MIC A/B), and allows for recognition by the NKG2D cytotoxicity receptor on KHYG-1 (40). This work may thus be generalizable to other tumours that express altered MIC A/B.

We compared 3 routes of administration of KHYG-1: IV, IP and SC. The dose of KHYG-1 administered for IV and IP was 20 million cells. This is of the same order of magnitude as the dose given in similar studies: 5-10 million cells in mice (16,21) and 15 million in rats (23,25). A larger dose of 45 million lymphokine-activated killer cells was

administered in various metastatic mouse models (41). Human doses vary but have been provided variously as $1-3.25 \times 10^{10}$ cells over 1-4 intravenous doses; $1 \times 10^8-3 \times 10^9/m^2$; 5×10^8 , 2×10^7 and up to 29×10^6 cells/kg (3-5,18). In our study, there was a high mortality (25%) associated with IV injections of the KHYG-1 cells, which might be lowered in future experiments by filtering the cells prior to injection to remove any clusters, as well as distributing the large dose over multiple injections. KHYG-1 accumulated in the tumour after SC injection of NK cells near the tumour; however, this route of administration will not be possible in future experiments using orthotopic prostate tumours and was tested as a proof-of-concept only.

Human and animal biodistribution studies show (1,18,22) that there is cell trapping, or the transient presence of NK in the lungs after IV injection, so to potentially increase the number of cells that reach the tumour, NK were also administered IP. There was no detectable signal change in the tumours after IP administration of labeled KHYG-1, although some KHYG-1 were detected by histology. This was likely because the KHYG-1 cells were sparsely distributed throughout the tumor and because the loading with iron was relatively low; combined, these two factors would limit the detection sensitivity by MRI. IP administration may be more relevant when the tumour is located in the abdomen; in ovarian cancer, IP administration of cisplatin and paclitaxel improved survival over IV drug administration (42). In mice, homing times of T-cells after IV and IP routes of administration have been compared in a study of ovalbumin-targeted T-cell homing to ovalbumin-expressing subcutaneous tumours. There was no difference in tumour T-cell accumulation, kinetics or therapeutic effect after IV and IP injection of 20 million cells, although there was a larger accumulation of T-cells in the spleen after IP administration (43). Peak accumulation was seen 5 days after injection for both routes of administration (43), which closely matches the imaging and histology timelines in our study.

There are two other published reports on the use of MRI cell tracking to image NK cells in cancer models, both involving the transfection of NK-92 to specifically target cancers (21,25). In the first of these papers, NK-92 were transfected to express a receptor for the Her2/neu antigen found on many breast cancers, then were labeled with a ferrocenyl

contrast agent and injected IV into nude mice bearing Her2/neu expressing tumours in the mammary fat pad. In the second study, NK-92 were transfected to target the epithelial cell adhesion molecule (EpCAM) and labeled with ferumoxides. Athymic rats bearing subcutaneous tumours from a human prostate cancer cell line expressing EpCAM were injected IV with the targeted and untargeted NK-92. In both experiments, migration of the targeted NK-92 was easily detected within 24 hours of injection by MRI and by histology. The non-targeted NK-92 did not migrate to the tumours in 24 hours (21,25). No later imaging and histology time points were reported in either study. Similar studies using have used PET and optical imaging to track targeted, but not untargeted, NK-92 to subcutaneous tumours (22,23).

In contrast, in our experiment we were able to histologically demonstrate accumulation of non-targeted KHYG-1 after 4 days. It is possible that there was some accumulation of KHYG-1 one day after administration; however, no mice were sacrificed at that time point so this cannot be confirmed. There was not sufficient change in the MRI images at day 1 post-injection to monitor migration of the labeled KHYG-1 cells that were injected IV and IP. In one mouse that received KHYG-1 SC near the tumour, there was both signal loss in the MRI image and histological findings of KHYG-1 in the margins of the tumour 1-4 days (MRI) and 5 days (histology) after. After IV and IP administration of KHYG-1, we were not able to detect a signal loss in the tumours despite histological evidence of KHYG-1 migration and persistence 4-12 days after administration.

The ability to detect iron-labeled cells with MRI is related to several factors, including: the total amount of iron per cell (which is influenced by the cell type, cell size, and type of iron particle), the pulse sequence used to collect MR images and the parameters of the pulse sequence (especially resolution and timing), the signal to noise ratio (tissue proton density and motion become important) and the distribution of iron labeled cells (signal loss is proportional to concentration of iron per image voxel) (44). We have previously shown that single, iron-labeled cells can be detected by MRI *in vivo* in the mouse brain with the bSSFP imaging sequence (26,27). However, those studies used macrophages and cancer cells, which incorporated much more iron per cell, the cells were labeled with agents which contain more iron per particle, and the cells were detected against an ideal

background (the brain) which further improved detection sensitivity. Shapiro et al. also demonstrated single cell detection *in vivo* with MRI using MPIO (45).

We chose to use MoldayION RhodamineB because it is biodegradable, non-toxic to cells at loading levels required for MRI and because the rhodamine tag provided an excellent means of validation. It has been also used to label mouse and non-human primate MSC and human breast cancer cells, without causing changes in viability, function, or the ability to differentiate (46,47). Feridex and Resovist, which are standard SPIO and have previously been used for NK cell tracking (21,25), are no longer commercially available. Although MPIO are advantageous for their very high iron content, we have found that labeling dendritic cells with MPIO caused alterations in some markers of DC activation and maturation (48). The lack of an obvious change in the MRI signal in tumours after IV and IP administration of KHYG-1, despite histological evidence of their accumulation in the tumour, is likely due to the combination of a relatively low iron content per cell and a low density of KHYG-1 in tumours. Future imaging experiments in orthotopic tumour models could focus on methods to increase iron loading into the KHYG-1 cells, by using a different SPIO contrast agent and methods such as electroporation and transfection agents, which have increased labeling of NK-92 cells (21,25).

A limitation of cellular MRI is the possibility of the iron being expelled from the labeled cells and taken up by bystander cells such as macrophages. Currently this can only be verified histologically. Another potential complication with interpreting subtle changes in MR signal, particularly decreases in signal intensity such as those that arise from iron oxide nanoparticles, is signal loss that results from endogenous sources of negative contrast in bSSFP images, such as bone, air, ferritin deposits and blood vessels. An example of this is the focal areas of signal loss that appeared in some tumors in mice that received no KHYG-1 cells and also in some IV treated mice. The similarities in the appearance of signal loss in the control and treated mice do not allow for a definitive conclusion that iron-labeled KHYG-1 were detected after IV administration.

We did not observe any difference in tumour volume in the treated and untreated mice in the cell tracking experiment. These experiments were not designed with conditions that

would optimally affect the tumours since our focus was on demonstrating that KHYG-1 cells could be labeled and detected in PC-3M tumours and comparing the 3 routes of administration. The lack of an observable change in the tumours after systemic KHYG-1 administration may be due to the relatively large tumour size at the beginning of treatment, or because the KHYG-1 were not provided with IL-2 to maintain their activation. The preclinical model of subcutaneous tumours used here is not representative of the therapeutic situation, where the targets would more likely be sites of metastasis. Still, this proof-of-principle study in a simple mouse model provides a first step toward realistic treatment goals and will be followed by studies in orthotopic and metastatic mouse models. MRI is an ideal technique to monitor response to treatment in these future studies.

As a pilot study for the effectiveness of NK cells on tumour growth under more optimal conditions and without the need for the NK cells to migrate to the tumours, KHYG-1 were injected directly into PC-3M tumours and IL-2 was administered to attempt to keep the NK cells viable for longer. There was a difference in tumour volume between treated and untreated tumours. This is consistent with a previous report in which NK-92 transfected to be IL-2 independent were injected into SC melanoma tumours and a treatment effect was seen (24).

2.5 References

1. Brand JM, Meller B, Von Hof K, Luhm J, Bähre M, Kirchner H, Frohn C. Kinetics and organ distribution of allogeneic natural killer lymphocytes transfused into patients suffering from renal cell carcinoma. *Stem Cells Dev* 2004, Jun;13(3):307-14.
2. Koehl U, Sörensen J, Esser R, Zimmermann S, Grüttner HP, Tonn T, et al. IL-2 activated NK cell immunotherapy of three children after haploidentical stem cell transplantation. *Blood Cells Mol Dis* 2004;33(3):261-6.

3. Miller JS, Soignier Y, Panoskaltsis-Mortari A, McNearney SA, Yun GH, Fautsch SK, et al. Successful adoptive transfer and in vivo expansion of human haploidentical NK cells in patients with cancer. *Blood* 2005, Apr 15;105(8):3051-7.
4. Arai S, Meagher R, Swearingen M, Myint H, Rich E, Martinson J, Klingemann H. Infusion of the allogeneic cell line NK-92 in patients with advanced renal cell cancer or melanoma: A phase I trial. *Cytotherapy* 2008;10(6):625-32.
5. Iliopoulou EG, Kountourakis P, Karamouzis MV, Doufexis D, Ardavanis A, Baxevanis CN, et al. A phase I trial of adoptive transfer of allogeneic natural killer cells in patients with advanced non-small cell lung cancer. *Cancer Immunol Immunother* 2010, Dec;59(12):1781-9.
6. Geller MA, Cooley S, Judson PL, Ghebre R, Carson LF, Argenta PA, et al. A phase II study of allogeneic natural killer cell therapy to treat patients with recurrent ovarian and breast cancer. *Cytotherapy* 2011, Jan;13(1):98-107.
7. Farag SS, Caligiuri MA. Human natural killer cell development and biology. *Blood Rev* 2006, May;20(3):123-37.
8. Albertsson PA, Basse PH, Hokland M, Goldfarb RH, Nagelkerke JF, Nannmark U, Kuppen PJK. NK cells and the tumour microenvironment: Implications for nk-cell function and anti-tumour activity. *Trends in Immunology* 2003;24(11):603-9.
9. Canadian Cancer Society Steering Committee. Canadian cancer statistics 2010.
10. Bachanova V, Burns LJ, McKenna DH, Curtsinger J, Panoskaltsis-Mortari A, Lindgren BR, et al. Allogeneic natural killer cells for refractory lymphoma. *Cancer Immunol Immunother* 2010, Nov;59(11):1739-44.
11. Yodoi J, Teshigawara K, Nikaido T, Fukui K, Noma T, Honjo T, et al. TCGF (IL 2)-receptor inducing factor (s). I. Regulation of IL 2 receptor on a natural killer-like cell line (YT cells). *The Journal of Immunology* 1985;134(3):1623.

12. Gong JH, Maki G, Klingemann HG. Characterization of a human cell line (NK-92) with phenotypical and functional characteristics of activated natural killer cells. *Leukemia* 1994, Apr;8(4):652-8.
13. Robertson MJ, Cochran KJ, Cameron C, Le JM, Tantravahi R, Ritz J. Characterization of a cell line, NKL, derived from an aggressive human natural killer cell leukemia. *Exp Hematol* 1996, Feb;24(3):406-15.
14. Yagita M, Huang C, Umehara H, Matsuo Y, Tabata R, Miyake M, et al. A novel natural killer cell line (KHYG-1) from a patient with aggressive natural killer cell leukemia carrying a p53 point mutation. *Leukemia* 2000;14(5):922-30.
15. Cheng M, Ma J, Chen Y, Zhang J, Zhao W, Wei H, et al. Establishment, characterization and successful adaptive therapy against human tumors of NKG cell, a new human NK cell line. *Cell Transplantation* 2011.
16. Tam YK, Martinson JA, Doligosa K, Klingemann HG. Ex vivo expansion of the highly cytotoxic human natural killer-92 cell-line under current good manufacturing practice conditions for clinical adoptive cellular immunotherapy. *Cytotherapy* 2003;5(3):259-72.
17. Jha P, Golovko D, Bains S, Hostetter D, Meier R, Wendland MF, Daldrup-Link HE. Monitoring of natural killer cell immunotherapy using noninvasive imaging modalities. *Cancer Res* 2010, Aug 1;70(15):6109-13.
18. Matera L, Galetto A, Bello M, Baiocco C, Chiappino I, Castellano G, et al. In vivo migration of labeled autologous natural killer cells to liver metastases in patients with colon carcinoma. *J Transl Med* 2006;4:49.
19. Melder RJ, Brownell AL, Shoup TM, Brownell GL, Jain RK. Imaging of activated natural killer cells in mice by positron emission tomography: Preferential uptake in tumors. *Cancer Res* 1993, Dec 15;53(24):5867-71.

20. Tonn T, Becker S, Esser R, Schwabe D, Seifried E. Cellular immunotherapy of malignancies using the clonal natural killer cell line NK-92. *J Hematother Stem Cell Res* 2001, Aug;10(4):535-44.
21. Daldrup-Link HE, Meier R, Rudelius M, Piontek G, Piert M, Metz S, et al. In vivo tracking of genetically engineered, anti-her2/neu directed natural killer cells to HER2/neu positive mammary tumors with magnetic resonance imaging. *Eur Radiol* 2005, Jan;15(1):4-13.
22. Meier R, Piert M, Piontek G, Rudelius M, Oostendorp RA, Senekowitsch-Schmidtke R, et al. Tracking of [18F]fdg-labeled natural killer cells to HER2/neu-positive tumors. *Nucl Med Biol* 2008, Jul;35(5):579-88.
23. Tavri S, Jha P, Meier R, Henning TD, Müller T, Hostetter D, et al. Optical imaging of cellular immunotherapy against prostate cancer. *Mol Imaging* 2009;8(1):15-26.
24. Lim YT, Cho MY, Noh YW, Chung JW, Chung BH. Near-infrared emitting fluorescent nanocrystals-labeled natural killer cells as a platform technology for the optical imaging of immunotherapeutic cells-based cancer therapy. *Nanotechnology* 2009, Nov 25;20(47):475102.
25. Meier R, Golovko D, Tavri S, Henning TD, Knopp C, Piontek G, et al. Depicting adoptive immunotherapy for prostate cancer in an animal model with magnetic resonance imaging. *Magn Reson Med* 2011, Mar;65(3):756-63.
26. Foster-Gareau P, Heyn C, Alejski A, Rutt BK. Imaging single mammalian cells with a 1.5 T clinical MRI scanner. *Magnetic Resonance in Medicine* 2003;49(5):968-71.
27. Heyn C, Ronald JA, Mackenzie LT, MacDonald IC, Chambers AF, Rutt BK, Foster PJ. In vivo magnetic resonance imaging of single cells in mouse brain with optical validation. *Magnetic Resonance in Medicine* 2006;55(1):23-9.
28. Shapiro EM, Sharer K, Skrtic S, Koretsky AP. In vivo detection of single cells by MRI. *Magn Reson Med* 2006, Feb;55(2):242-9.

29. Frank JA, Miller BR, Arbab AS, Zywicke HA, Jordan EK, Lewis BK, et al. Clinically applicable labeling of mammalian and stem cells by combining superparamagnetic iron oxides and transfection agents. *Radiology* 2003, Aug;228(2):480-7.
30. Bernas LM, Foster PJ, Rutt BK. Imaging iron-loaded mouse glioma tumors with bssfp at 3 T. *Magn Reson Med* 2010, Jul;64(1):23-31.
31. Ramadan SS, Heyn C, MacKenzie LT, Chambers AF, Rutt BK, Foster PJ. Ex-vivo cellular MRI with b-ssfp: Quantitative benefits of 3 T over 1.5 T. *Magnetic Resonance Materials in Physics, Biology and Medicine* 2008;21(4):251-9.
32. Gonzalez-Lara LE, Xu X, Hofstetrova K, Pniak A, Brown A, Foster PJ. In vivo magnetic resonance imaging of spinal cord injury in the mouse. *Journal of Neurotrauma* 2009;26(5):753-62.
33. Suck G, Branch DR, Smyth MJ, Miller RG, Vergidis J, Fahim S, Keating A. KHYG-1, a model for the study of enhanced natural killer cell cytotoxicity. *Exp Hematol* 2005, Oct;33(10):1160-71.
34. Kozlowski JM, Fidler IJ, Campbell D, Xu Z, Kaighn ME, Hart IR. Metastatic behavior of human tumor cell lines grown in the nude mouse. *Cancer Res* 1984, Aug;44(8):3522-9.
35. BioPAL. Relaxation values for biopal products. [Www.biopal.com/images/relaxxation Values for Biopal Products.pdf](http://www.biopal.com/images/relaxxation%20Values%20for%20Biopal%20Products.pdf) 2013, Mar 19.
36. Rosset A, Spadola L, Ratib O. OsiriX: An open-source software for navigating in multidimensional DICOM images. *J Digit Imaging* 2004, Sep;17(3):205-16.
37. Tomayko MM, Reynolds CP. Determination of subcutaneous tumor size in athymic (nude) mice. *Cancer Chemother Pharmacol* 1989;24(3):148-54.
38. Müller T, Uherek C, Maki G, Chow KU, Schimpf A, Klingemann HG, et al. Expression of a cd20-specific chimeric antigen receptor enhances cytotoxic activity of

NK cells and overcomes nk-resistance of lymphoma and leukemia cells. *Cancer Immunol Immunother* 2008, Mar;57(3):411-23.

39. Suck G, Branch DR, Keating A. Irradiated KHYG-1 retains cytotoxicity: Potential for adoptive immunotherapy with a natural killer cell line. *Int J Radiat Biol* 2006, May;82(5):355-61.

40. Wu JD, Higgins LM, Steinle A, Cosman D, Haugk K, Plymate SR. Prevalent expression of the immunostimulatory MHC class I chain # x02013; related molecule is counteracted by shedding in prostate cancer. *Journal of Clinical Investigation* 2004;114(4):560.

41. Basse P, Herberman RB, Nannmark U, Johansson BR, Hokland M, Wasserman K, Goldfarb RH. Accumulation of adoptively transferred adherent, lymphokine-activated killer cells in murine metastases. *J Exp Med* 1991, Aug 1;174(2):479-88.

42. Armstrong DK, Bundy B, Wenzel L, Huang HQ, Baergen R, Lele S, et al. Intraperitoneal cisplatin and paclitaxel in ovarian cancer. *N Engl J Med* 2006, Jan 5;354(1):34-43.

43. Petersen CC, Petersen MS, Agger R, Hokland ME. Accumulation in tumor tissue of adoptively transferred T cells: A comparison between intravenous and intraperitoneal injection. *J Immunother* 2006;29(3):241-9.

44. Heyn C, Bowen CV, Rutt BK, Foster PJ. Detection threshold of single spio-labeled cells with FIESTA. *Magnetic Resonance in Medicine* 2005;53(2):312-20.

45. Shapiro EM, Sharer K, Skrtic S, Koretsky AP. In vivo detection of single cells by MRI. *Magn Reson Med* 2006, Feb;55(2):242-9.

46. McFadden C, Mallett CL, Foster PJ. Labeling of multiple cell lines using a new iron oxide agent for cell tracking by MRI. *Contrast Media and Molecular Imaging* 2011, Nov;6(6):514-22.

47. Addicott B, Willman M, Rodriguez J, Padgett K, Han D, Berman D, et al. Mesenchymal stem cell labeling and in vitro MR characterization at 1.5 T of new SPIO contrast agent: Molday ION rhodamine-b™. *Contrast Media Mol Imaging* 2011;6(1):7-18.
48. Rohani R, de Chickera SN, Willert C, Chen Y, Dekaban GA, Foster PJ. In vivo cellular MRI of dendritic cell migration using micrometer-sized iron oxide (MPIO) particles. *Mol Imaging Biol* 2011, Aug;13(4):679-94.

Chapter 3

3 Optimization of the Balanced Steady State Free Precession (bSSFP) Pulse Sequence for Magnetic Resonance Imaging of the Mouse Prostate at 3T*

3.1 Introduction

Prostate cancer is the most-diagnosed non-melanoma cancer in Canadian men and the third-leading cause of cancer death (1). Mouse models of prostate cancer are valuable for pre-clinical studies of prostate cancer and include transgenic models such as the Transgenic Adenocarcinoma of Mouse Prostate (TRAMP) model (2), and xenograft models (3–5) that typically involve subcutaneous or orthotopic (intra-prostatic) injection of cancer cells. Subcutaneous tumours are easy to implant and measurable with calipers, but orthotopic tumours are superior for studies in which metastasis is desired (6–9). In the case of intra-prostatic tumours, without imaging, tumour volume can only be estimated by palpation and then measured after sacrifice, which requires a single measurement for each animal and potentially a large number of animals with separate groups of mice sacrificed at multiple time points.

The use of magnetic resonance imaging (MRI) allows for the non-invasive quantification of tumor size, so that multiple time points are measured in each animal, allowing for smaller sample sizes and more complete data. There is also the opportunity to manipulate the tissue contrast to better visualize the tissue of interest and to gain different information about pathology. The prostate is adjacent to the bladder and surrounded by fatty tissue, which must be taken into account when determining which imaging pulse sequence and parameters to use. MRI has been used to monitor prostate tumour growth in mice, primarily at high field strengths (>4T), but also at clinical field strengths (1.5T and

* This chapter was previously published as: Mallett CL and Foster PJ (2011) *Optimization of the Balanced Steady State Free Precession (bSSFP) Pulse Sequence for Magnetic Resonance Imaging of the Mouse Prostate at 3T* PLoSONE 6(4):e18361.

3T). Most investigations have used 2D T_1 - or T_2 -weighted spin echo sequences (T_1 wSE and T_2 wSE), but 3D imaging sequences have also been used (9–23).

The purpose of this study was to optimize 3D imaging of the mouse prostate to achieve high SNR, high contrast-to-noise (CNR) and high resolution between the prostate and surrounding tissues, using the balanced steady state free precession (bSSFP) pulse sequence. This SNR-efficient sequence has not previously been used for mouse prostate imaging, and has the advantage of sensitivity to iron, which will be useful in future studies of iron-labeled cell tracking in a mouse model of prostate cancer.

3.2 Methods

3.2.1 Animals

Healthy male nude mice (5–12 weeks of age) were studied. Mice were housed in a specific pathogen-free barrier facility in between scanning sessions. All animal experiments were approved by the Animal Use Subcommittee of the University Council on Animal Care at The University of Western Ontario following the guidelines of the Canadian Council on Animal Care (protocol # 2006-03).

3.2.2 MRI

Scans were performed on a 3T GE Excite MR750 system using a custom-built high-performance gradient insert with an inner diameter of 17.5 cm, maximum gradient strength of 500 mT/m and peak slew rate of 3,000 T/m/s, and a custom solenoidal whole-mouse body RF coil 4 cm in length and 3 cm in diameter. For live mouse imaging, mice were anaesthetized with isoflurane (2% in oxygen) and placed supine in the coil, warm saline bags were taped near the RF coil to maintain body temperature, and the mice were wrapped with gauze and tape for consistent positioning and to minimize motion artifact due to respiration. For *ex vivo* imaging, a mouse was euthanized by euthanyl then immediately imaged in the same manner.

Images acquired using the bSSFP pulse sequence had the following parameters at 200 μm isotropic spatial resolution. For axial scans, the field of view (FOV) was 3x3 cm (14 minutes) or 4x4 cm (20 minutes), and for coronal scans it was 6x3.3 cm (26 minutes).

The flip angle (FA) was varied between 30°, 40° and 50°. The receiver bandwidth (BW) was varied from ± 31.25 , ± 41.67 , ± 62.5 and ± 83.3 kHz. Repetition time (TR) was automatically set by the scanner software in accordance with BW and FOV, and echo time (TE) was set to be half of TR. Thus, TR ranged from 3.3–4.6 ms and TE from 1.7–2.3 ms. The number of signal averages (NEX) ranged from 1–4. An RF phase cycling scheme with a sum of squared reconstruction was implemented and the number of phase cycles (PC) was varied between 2–8. Axial bSSFP images (FOV 3x3 cm, 14 minutes) were compared with the more traditionally-used spin echo (SE) images acquired with the following parameters: axial orientation, FOV 3x3 cm, TR/TE = 600/25 ms (T_{1w}), 2000/70 ms (T_{2w}), 1 mm slice thickness, 128x128 matrix, 234 mm in-plane resolution, and acquisition time of 20 (T_{1w}) or 17 (T_{2w}) minutes.

3.2.3 Image Analysis

Images were compared based on SNR, contrast to noise ratio CNR, and presence of artifacts such as chemical shift. SNR was calculated as the mean signal from the hindlimb muscle divided by the standard deviation of the background signal. CNR was calculated as the difference in SNR between the prostate and the surrounding fatty tissue. In order to compare sequences with different scan times and slice thicknesses, SNR efficiency was calculated as the SNR divided by the square root of the scan time (in minutes) and was normalized by slice thickness (in mm).

3.3 Results

3.3.1 Effect of phase cycles and averaging

Phase cycling is used with the bSSFP sequence to avoid the appearance of characteristic dark banding artifacts that are caused by sensitivity to local field inhomogeneities and which degrade image quality considerably. Figure 3.1 shows the effect of phase cycling (2, 4 and 8 PC) and averaging (4, 2 and 1 NEX) on prostate image quality in a sacrificed mouse. All scans took 20 minutes. SNR values did not vary significantly with different amounts of phase cycling, and CNR was highest for 4 PC, 2 NEX and 8PC, 1 NEX.

There was no banding artifact in any of the images. The shape of the prostate in these *ex vivo* images is different from the prostate *in vivo* due to deflation of the bladder in the sacrificed mouse. For all future bSSFP acquisitions, 4 PC and 2 NEX were used.

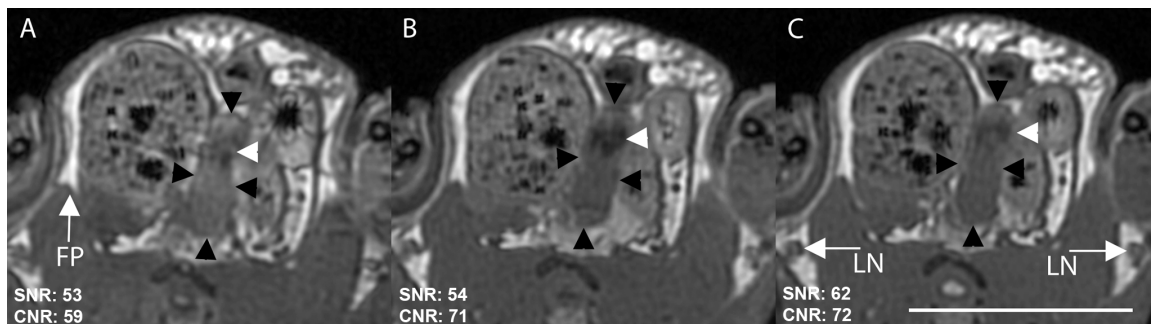


Figure 3.1: Effect of phase cycling and averaging on *ex vivo* prostate image quality. Cropped and enlarged sections of axial scans: A: 2 PC, 4 NEX, B: 4 PC, 2 NEX, C: 8 PC, 1 NEX. Black arrowheads indicate prostate, white arrowheads urethra, FP is the fat pad used for CNR measurements and LN are the inguinal lymph nodes. Scale bar is 1 cm. Axial scan, FOV 4x4 cm, 200 μ m isotropic resolution, TR/TE = 3.9/2.0 ms, FA 30°, BW \pm 62.5 kHz, 20 minutes.

3.3.2 Effect of bandwidth and flip angle

When flip angles were compared, image SNR (based on muscle signal) was approximately equal between flip angles, ranging from 20 to 23 (Figure 3.2). CNR increased with flip angle, with values of 40, 54 and 77 for 30°, 40° and 50°, respectively. With a flip angle of 50°, the best SNR and CNR was obtained with a bandwidth of \pm 31.25 kHz (SNR = 25, CNR = 116); however, there were artifacts such as a slight chemical shift between the urethra and prostate tissue, as well as a blurring of the edges of the prostate, at the lowest bandwidth (D) compared to the highest bandwidth (F). When the bandwidth was set to \pm 62.5 kHz, the artifacts were reduced with a higher CNR than was seen at a bandwidth of \pm 83.5 kHz.

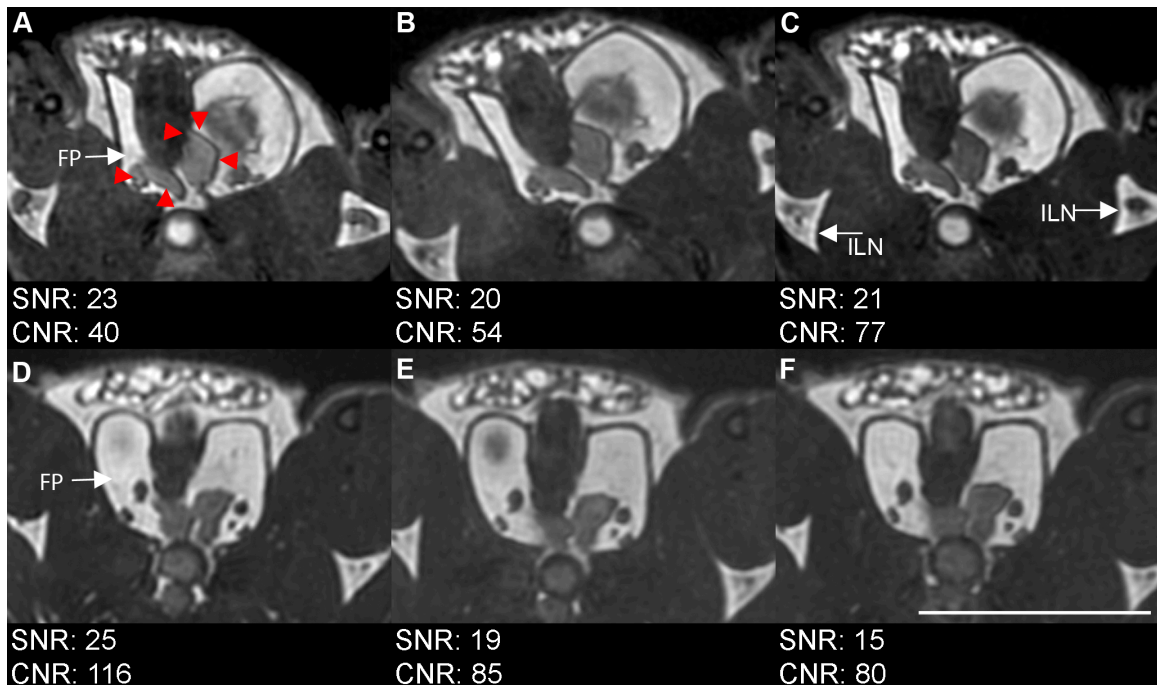


Figure 3.2: Effect of flip angle and bandwidth on prostate visibility and artifacts.

Flip angle of A: 30° vs B: 40° vs C: 50° at BW of ± 62.5 kHz. Bandwidth of D: ± 31.25 kHz vs E: ± 62.5 kHz vs F: ± 83.3 kHz. Red arrowheads indicate prostate boundaries. White arrows point to fat pad used for CNR calculations (FP) and to inguinal lymph nodes (ILN). Scale bar is 1 cm. Scan parameters: Axial scan, FOV 3x3 cm, 200 μ m isotropic resolution, TR/ TE = 3.3–4.6 ms/1.1–2.3 ms, 4 PC, 2 NEX, 14 minutes.

3.3.3 Comparison of bSSFP with T_1 w and T_2 w SE

Axial scans of a mouse were acquired with bSSFP with 4 PC, 2 NEX, FA 50° and BW ± 62.5 kHz (14 minutes) as determined above and compared to T_1 wSE (20 min) and T_2 wSE (17 min) scans with parameters as indicated in the methods section (Figure 3.3). The T_1 wSE image had the highest CNR of the prostate relative to the surrounding fat at 114, compared to 84 for the bSSFP image and 12 for the T_2 wSE. While the overall SNR was highest for the T_1 wSE image at 41, it must be noted that the slice thickness for the bSSFP, which had an SNR of 17, was 0.2 mm, compared to 1 mm for T_1 wSE. The SNR for the T_2 wSE, also acquired with 1 mm slices, was 16. The SNR efficiency was calculated and normalized by slice thickness: the bSSFP had the largest SNR efficiency at 23, compared to 9 for the T_1 wSE and 3 for the T_2 wSE.

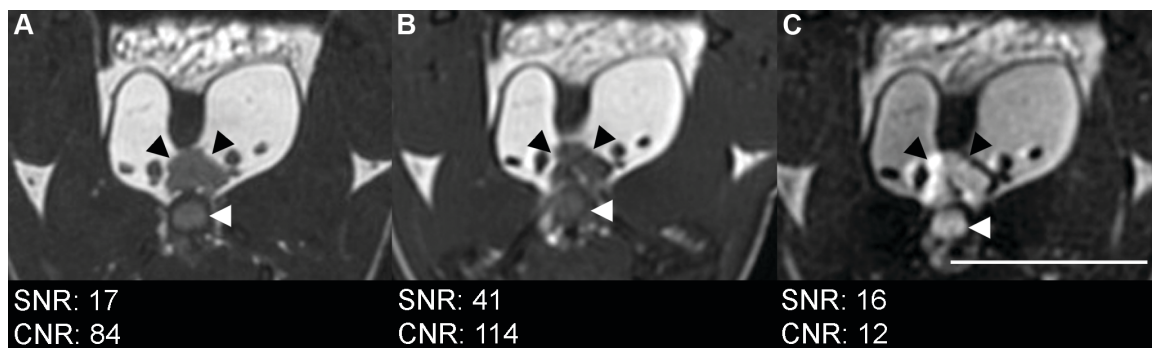


Figure 3.3: Comparison of *in vivo* axial images acquired with 3 different pulse sequences.

A: bSSFP, B: T_1 wSE and C: T_2 wSE. Black arrows indicate prostate, white arrows indicate urethra. Scale bar is 1 cm. bSSFP images acquired using optimized sequence with 3x3 cm FOV. Spin echo sequences acquired with axial orientation, FOV 3x3 cm, TR/TE = 600/25 ms (T_1 w), 2000/70 ms (T_2 w), 1 mm slice thickness, 128x128 matrix, 234 mm in-plane resolution, and 20 (T_1 w) and 17 (T_2 w) minutes acquisition time.

3.3.4 3D nature of bSSFP

Since bSSFP is a 3-dimensional sequence, the image can be re-oriented to view the prostate from any angle (Figure 3.4). This is valuable to visualize the morphology and size of the prostate. A simple re-orientation of the scan plane and enlargement of the field of view allows for acquisition of whole mouse-body images, in a short scan time, that include clear views of the prostate and other organs of interest, such as lymph nodes and lymph vessels (Figure 3.5).

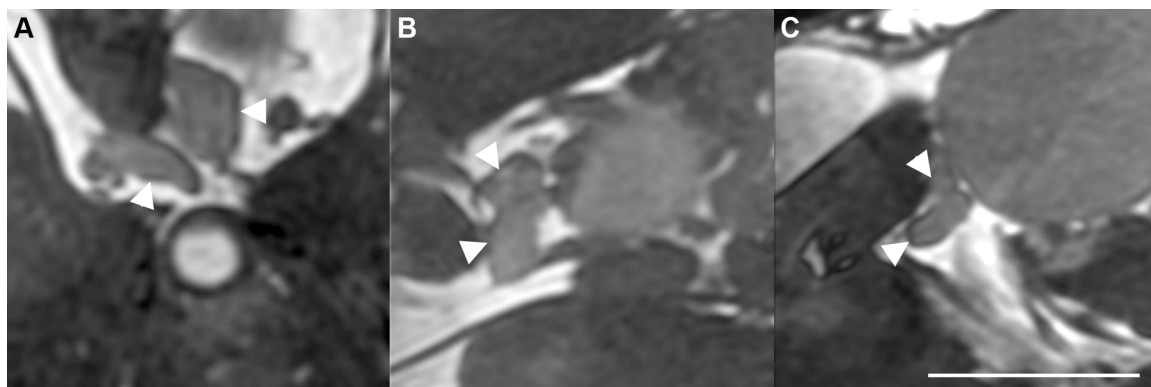


Figure 3.4: 3 views of prostate from one 3-dimensional *in vivo* scan.

A: axial, B: coronal, C: sagittal. White arrows indicate prostate. Scale bar is 0.5 cm. Axial scan, FOV 3x3 cm, 200 μ m isotropic resolution, TR/TE = 4.6 ms/2.3 ms, 4 PC, 2 NEX, FA 50°, BW \pm 62.5 kHz, 14 minutes.

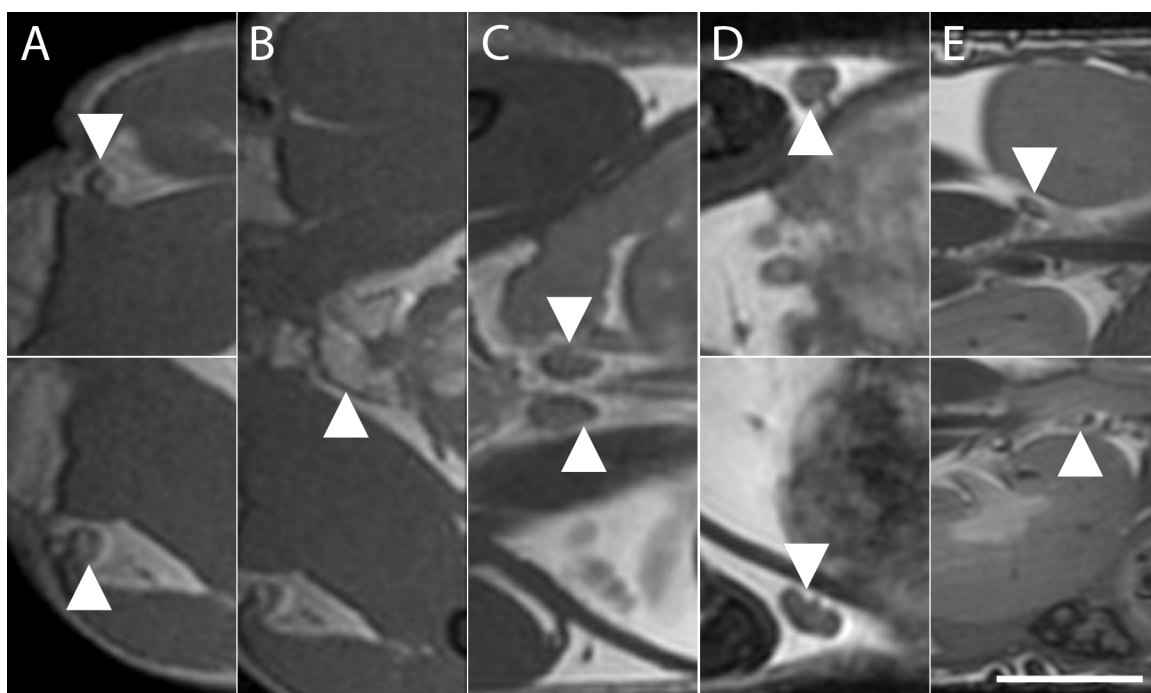


Figure 3.5: Sections of coronal view of mouse with prostate and lymph nodes identified.

Tail is at left, head at right. White arrows indicate organs of interest as follows. A: popliteal lymph nodes; B: prostate; C: iliac lymph nodes; D: inguinal lymph nodes with lymph vessels visible; E: Renal lymph nodes. Scale bar is 0.5 cm. Coronal scan, FOV 6x3.3 cm, 200 μ m isotropic resolution, TR/TE = 4.6/2.3 ms, BW \pm 62.5 kHz, FA 40°, 8 PC, 2 NEX, 26 minutes.

3.4 Discussion

MRI measurements of the mouse prostate are desirable for visualizing the prostate over time with the flexibility of being able to manipulate contrast. An advantage of MRI is sensitivity for early detection: measurements of the long and short axes of the prostate in 2D T_1 wSE images acquired at 7T were able to detect prostate cancer 4 weeks sooner than by palpation (12,16).

Previous work on imaging the mouse prostate has been primarily with 2-dimensional T_1 W (12,16,19,21) or T_2 W (9,11,18–20,22,23) spin echo pulse sequences that provide only a single orientation for viewing. With these 2D sequences it is often necessary to use thick slices in order to obtain a reasonable SNR in a reasonable scan time – these have been as high as 500–2000 μm (14,15,19,22,23) in these sequences, although in one case it was reduced to 50 μm when field strength was increased to 4.7T from 1.5T (10). In plane resolution is higher, typically ~ 100 μm . Three-dimensional sequences such as T_1 W and T_2 W fast spin echo and fast low angle shot also yield a variety of slice thicknesses from 300–2000 μm and in-plane resolutions of 80–400 μm at clinical and high field strengths (11,13–15,17).

Even at high field strength, scan time can be quite long, for example 2.5 hours with an additional hour for setup (18). While this protocol at 7T allowed for impressive discrimination of the ventral from the dorsolateral lobes of the prostate using a 2D T_2 WSE sequence with CHESS (chemical shift selective sequence), this scan time is impractical for studies involving more than a few mice. More reasonable scan times of 10–15 minutes at 7T were achieved through the use of techniques such as RARE and multi-echo sequences (9,11).

Techniques for enhancing prostate contrast include using a long TE and fat saturation in a 5–15 minute 2D fast spin-echo (FSE) scans at 3T (19). Also at 3T, a 3D fast low-angle shot sequence with fat suppression was used to obtain scans with 400 μm isotropic voxel size in 10 minutes (17). Additionally, fat suppression by saturation pre-pulses has been used at 7T (9,17–19). Gadolinium has also been used to enhance contrast (21,24). Other methods of visualizing prostate tumours include using diffusion weighted imaging, which

improved detection of small tumours (<1mm in diameter) compared to T_2W imaging in a transgenic mouse model of prostate cancer (20).

In this study, we did not use any additional contrast enhancement techniques such as fat suppression; consequently, the seminal vesicles were not detectable from the surrounding fat in healthy mice. It is common for prostate tumours to spread to the seminal vesicles; however, the seminal vesicles can be completely destroyed by large prostate tumours (16), and the tumour-fat contrast may be different from healthy seminal vesicle-fat contrast. Nevertheless, it might be helpful in the future to exploit the chemical shift artifact of the second kind to suppress mixed water-fat pixels using a TE and TR such that the water and fat frequencies are out of phase; fat-tissue interfaces would be black. However, the TR would have to be increased, leading to a longer scan time (25).

The bSSFP pulse sequence is very SNR efficient and produces unique T_2/T_1 contrast (26). This sequence has been recently applied to investigations of glioma in the mouse brain (27,28). A challenge presented by bSSFP, however, is its high sensitivity to local field inhomogeneities. The result is a characteristic “banding artifact” that worsens at higher field strengths and with longer TR (26). Multiple acquisition RF phase cycling techniques ameliorate this problem and have allowed for bSSFP imaging at higher field strengths and with longer TR (28,29). Although the sensitivity of bSSFP to local field inhomogeneities can be problematic, it has also been what has enabled this sequence to be used for highly sensitive cellular imaging, which has allowed the detection of iron-labeled single cells and cell clusters at 1.5 T and 3 T (30–35). This feature of bSSFP may be useful in mouse models of prostate cancer for detecting and monitoring metastases.

We have obtained excellent high resolution, high SNR images of the healthy mouse prostate in a relatively short scan time using the bSSFP pulse sequence. For our mouse studies, this was achieved using a custom-built high-performance gradient insert on a clinical 3T system. While the maximum strength of the insertable gradient coil used in this study is 500 mT/m, we operated below this. For example, with receiver BW of ± 62 kHz, and FOV of 3 cm, (γ is 42.57 Hz/T), the strength of the readout gradient is approximately 100mT/m (using the equation $G(\text{read-out}) = 2 \cdot \text{BW} / (\gamma \cdot \text{FOV})$). The

gradient strength used to excite the slab is also far below this maximum strength since a thick slab is used that encompasses the whole mouse body. Clinical gradients of 50 mT/m and higher are now available on whole body scanners; therefore, bSSFP protocols similar to that used in this study are not out of the question for modern-day clinical gradients.

In conclusion, this study shows that with optimized imaging parameters, 3D mouse body images acquired with bSSFP allow for the simultaneous visualization of the prostate and its draining lymph nodes, the iliac and renal lymph nodes, as well as the nearby inguinal and popliteal lymph nodes. The ability to detect both the prostate and the lymph nodes in a single fast, high-resolution scan will be useful for studies that aim to investigate prostate cancer metastasis.

3.5 References

1. Canadian Cancer Society (2010) Canadian Cancer Statistics 2010.
2. Greenberg NM, DeMayo F, Finegold MJ, Medina D, Tilley WD, et al. (1995) Prostate cancer in a transgenic mouse. *Proc Nat Acad Sci USA* 92: 3439–3443.
3. Thalmann GN, Sikes RA, Wu TT, Degeorges A, Chang SM, et al. (2000) LNCaP progression model of human prostate cancer: androgen-independence and osseous metastasis. *Prostate* 44: 91–103.
4. Deeb D, Gao X, Jiang H, Dulchavsky SA, Gautam SC (2009) Oleanane triterpenoid CDDO-Me inhibits growth and induces apoptosis in prostate cancer cells by independently targeting pro-survival Akt and mTOR. *Prostate* 69: 851–860.
5. Wolf P, Alt K, Bühler P, Katzenwadel A, Wetterauer U, et al. (2008) Anti-PSMA immunotoxin as novel treatment for prostate cancer? High and specific antitumor activity on human prostate xenograft tumors in SCID mice. *Prostate* 68: 129–138.
6. Bastide C, Bagnis C, Mannoni P, Hassoun J, Bladou F (2002) A Nod Scid mouse model to study human prostate cancer. *Prostate Cancer Prostatic Dis* 5: 311–315.

7. Kozlowski JM, Fidler IJ, Campbell D, Xu Z, Kaighn ME, Hart IR (1984) Metastatic behavior of human tumor cell lines grown in the nude mouse. *Cancer Res* 44: 3522–3529.
8. Stephenson RA, Dinney CPN, Gohji K, Ordonez NG, Killion JJ, Fidler IJ (1992) Metastatic model for human prostate cancer using orthotopic implantation in nude mice. *JNCI Journal of the National Cancer Institute* 84: 951.
9. Jennbacken K, Gustavsson H, Tesan T, Horn M, Vallbo C, et al. (2009) The prostatic environment suppresses growth of androgen-independent prostate cancer xenografts: an effect influenced by testosterone. *Prostate* 69: 1164–1175.
10. Adhami VM, Siddiqui IA, Sarfaraz S, Khwaja SI, Hafeez BB, et al. (2009) Effective prostate cancer chemopreventive intervention with green tea polyphenols in the TRAMP model depends on the stage of the disease. *Clin Cancer Res* 15: 1947–1953.
11. Degrassi A, Russo M, Scanziani E, Giusti A, Ceruti R, et al. (2007) Magnetic resonance imaging and histopathological characterization of prostate tumors in TRAMP mice as model for pre-clinical trials. *Prostate* 67: 396–404.
12. Eng MH, Charles LG, Ross BD, Chrisp CE, Pienta KJ, et al. (1999) Early castration reduces prostatic carcinogenesis in transgenic mice. *Urology* 54: 1112–1119.
13. Fricke ST, Rodriguez O, Vanmeter J, Dettin LE, Casimiro M, et al. (2006) *In vivo* magnetic resonance volumetric and spectroscopic analysis of mouse prostate cancer models. *Prostate* 66: 708–717.
14. Gupta S, Hastak K, Ahmad N, Lewin JS, Mukhtar H (2001) Inhibition of prostate carcinogenesis in TRAMP mice by oral infusion of green tea polyphenols. *Proc Natl Acad Sci U S A* 98: 10350–10355.
15. Gupta S, Adhami VM, Subbarayan M, MacLennan GT, Lewin JS, et al. (2004) Suppression of prostate carcinogenesis by dietary supplementation of celecoxib in transgenic adenocarcinoma of the mouse prostate model. *Cancer Res* 64: 3334–3343.

16. Hsu CX, Ross BD, Chrisp CE, Derrow SZ, Charles LG, et al. (1998) Longitudinal cohort analysis of lethal prostate cancer progression in transgenic mice. *J Urol* 160: 1500–1505.
17. Kumar AP, Bhaskaran S, Ganapathy M, Crosby K, Davis MD, et al. (2007) Akt/cAMP-responsive element binding protein/cyclin D1 network: a novel target for prostate cancer inhibition in transgenic adenocarcinoma of mouse prostate model mediated by Nexrutine, a Phellodendron amurense bark extract. *Clin Cancer Res* 13: 2784–2794.
18. Nastiuk KL, Liu H, Hamamura M, Muftuler LT, Nalcioglu O, Krolewski JJ (2007) *In vivo* MRI volumetric measurement of prostate regression and growth in mice. *BMC Urol* 7: 12.
19. Rad AM, Gao X, Deeb D, Gautam SC, Arbab AS (2008) Imaging Mouse Prostate Gland by 3 Tesla Clinical MRI System. *Open Magn Reson Rev* 1: 60–63.
20. Song SK, Qu Z, Garabedian EM, Gordon JI, Milbrandt J, Ackerman JJ (2002) Improved magnetic resonance imaging detection of prostate cancer in a transgenic mouse model. *Cancer Res* 62: 1555–1558.
21. Stoyanova R, Hachem P, Hensley H, Khor LY, Mu Z, et al. (2007) Antisense-MDM2 sensitizes LNCaP prostate cancer cells to androgen deprivation, radiation, and the combination *in vivo*. *Int J Radiat Oncol Biol Phys* 68: 1151–1160.
22. Chen Z, Trotman LC, Shaffer D, Lin HK, Dotan ZA, et al. (2005) Crucial role of p53-dependent cellular senescence in suppression of Pten-deficient tumorigenesis. *Nature* 436: 725–730.
23. Trotman LC, Niki M, Dotan ZA, Koutcher JA, Di Cristofano A, et al. (2003) Pten dose dictates cancer progression in the prostate. *PLoS Biol* 1: E59.
24. Kiss P, Eltoum IE, Suranyi P, Zeng H, Simor T, et al. (2009) Virtual *in vivo* biopsy map of early prostate neoplasm in TRAMP mice by MRI. *Prostate* 69: 449–458.

25. Stadler A, Schima W, Ba-Ssalamah A, Kettenbach J, Eisenhuber (2007) Artifacts in body MR imaging: their appearance and how to eliminate them. *Eur Radiol* 17: 1242–1255.
26. Scheffler K, Lehnhardt S (2003) Principles and applications of balanced SSFP techniques. *Eur Radiol* 13: 2409–2418.
27. Bernas LM, Foster PJ, Rutt BK (2010) Imaging iron-loaded mouse glioma tumors with bSSFP at 3 T. *Magnetic Resonance in Medicine* 64: 23–31. 28.
28. Miraux S, Massot P, Ribot EJ, Franconi JM, Thiaudiere E (2008) 3D TrueFISP imaging of mouse brain at 4.7 T and 9.4 T. *Journal of Magnetic Resonance Imaging* 28: 497–503.
29. Bangerter NK, Hargreaves BA, Vasanawala SS, Pauly JM, Gold GE, Nishimura DG (2004) Analysis of multiple-acquisition SSFP. *Magn Reson Med* 51: 1038–1047.
30. Foster-Gareau P, Heyn C, Alejski A, Rutt BK (2003) Imaging single mammalian cells with a 1.5 T clinical MRI scanner. *Magnetic Resonance in Medicine* 49: 968–971.
31. Gonzalez-Lara LE, Xu X, Hofstetrova K, Pniak A, Brown A, Foster PJ (2009) *In vivo* Magnetic Resonance Imaging of Spinal Cord Injury in the Mouse. *Journal of Neurotrauma* 26: 753–762.
32. Heyn C, Bowen CV, Rutt BK, Foster PJ (2005) Detection threshold of single SPIO-labeled cells with FIESTA. *Magnetic Resonance in Medicine* 53: 312–320.
33. Heyn C, Ronald JA, Mackenzie LT, MacDonald IC, Chambers AF, et al. (2006) *In vivo* magnetic resonance imaging of single cells in mouse brain with optical validation. *Magnetic Resonance in Medicine* 55: 23–29.
34. Jirak D, Kriz J, Strzelecki M, Yang J, Hasilo C, et al. (2009) Monitoring the survival of islet transplants by MRI using a novel technique for their automated detection and quantification. *Magnetic Resonance Materials in Physics, Biology and Medicine* 22: 257–265.

35. Ramadan SS, Heyn C, MacKenzie LT, Chambers AF, Rutt BK, Foster PJ (2008) Ex-vivo cellular MRI with b-SSFP: quantitative benefits of 3 T over 1.5 T. *Magnetic Resonance Materials in Physics, Biology and Medicine* 21: 251–259.

Chapter 4

4 Anatomical and Metabolic Magnetic Resonance Imaging Characterization of an Orthotopic Mouse Model of Prostate Cancer Using the PC-3M Cell Line in Nude Mice

4.1 Introduction

Prostate cancer (PCa) is the second most commonly diagnosed non-skin cancer in North American men and the 2nd and 3rd most deadly in the United States and Canada, respectively (1,2). Mouse models of prostate cancer include transgenic and knockout models such as TRAMP and Pten (3,4), as well as subcutaneous or orthotopic injection of human cancer cells into immune-compromised mice. With orthotopically-implanted cells, prostate tumours can be difficult to palpate, particularly when the tumours are small (< 0.5 cm), and precise volume measurement is possible only at necropsy. Magnetic resonance imaging (MRI) can be a valuable tool to track tumour growth longitudinally *in vivo* as well as response to therapy (3,5-8). We have previously shown that the bSSFP MRI sequence can be used to image the mouse prostate and we have determined the optimal sequence parameters in healthy male mice. These whole body images also allow visualization of prostate-draining lymph nodes that could be sites of metastasis (9).

The unique flexibility of MRI also allows for the measurement of factors other than volume. For example, spectroscopy after the injection of hyperpolarized ¹³C-labeled compounds into the mice can be used to measure metabolism. With hyperpolarized ¹³C-labeled pyruvate, the difference in pyruvate metabolism between normal tissue (through the citric acid cycle) and tumour (aerobic glycolysis and conversion of pyruvate to lactate) can be detected by measuring the ratio of lactate to pyruvate in a spectrum (10). Lactate/pyruvate ratio has been found to correlate with the grade of PCa in TRAMP mice (11) and is an early indicator of response to chemotherapy and radiation therapy in other cancer models (12-14).

This study was conducted to use MRI to characterize the growth, metastasis and metabolism of developing orthotopic human-derived prostate tumours in an immune-compromised mouse model, in the context of establishing a timeline for therapy with natural killer (NK) cells. The criteria we determined for an optimal therapeutic time is one where a tumour is reliably present as detected by MRI, but where the tumour is still small enough to allow for long-term comparisons of treated and untreated tumours; for example, a time point for treatment should be before a tumour becomes necrotic, and well before the onset of morbidity such as bladder stenosis and impaired mobility. Knowing the time required for lymph node metastases to develop would offer the ability to determine the effectiveness of the treatment in preventing metastasis and monitor the ability of NK to track to lymph nodes. In order to characterize this model for tumour size, appearance and cancer cell distribution, mice were followed with anatomical MRI long-term for 30 days, and shorter term for 9 or 13 days. Additionally, [1-¹³C]pyruvate spectroscopy was used to measure pyruvate metabolism in the later stages of tumour growth. At the endpoints, the spleen and draining lymph nodes (iliac, renal, sciatic, popliteal as well as the inguinal) of the prostate were examined *ex vivo* for the presence of cancer cells and histological characteristics. To the best of our knowledge, this is the first study to use MRI to monitor volume of orthotopic PC-3M tumours over time and the first to use ¹³C spectroscopy on a xenograft model of prostate cancer.

4.2 Methods

4.2.1 Cells

We used the PC-3M cell line, which is a metastatic variant of the PC-3 cell line (15,16). PC-3M cells were cultured in RPMI-1640 with 10% fetal bovine serum (FBS). Cells in log phase were harvested by trypsinization, washed once with HBSS, and suspended in HBSS at a density of 0.5 million cells per 30-40 μ L for injection into the mice.

4.2.2 Tumour Cell Injection

All experiments were approved by the University of Western Ontario Animal Use Committee. Male nude mice (nu/nu, aged 6-8 weeks) (Charles River Laboratories, Saint-Constant, QC) were housed in a specific pathogen-free exclusion barrier facility. For surgery, mice were anaesthetized with 2% isoflurane in oxygen, an incision was made in the lower abdomen, and the bladder was retracted to expose the prostate. Cells were injected into the left lateral or dorsal lobes of the prostate using a butterfly needle attached by a catheter to a Hamilton syringe for precise injection, following the model presented by (17-19). The inner and outer layers of the incision were sutured. Mice were treated with ketaprofen at 4 mg/kg IP 2x a day for 3 days.

4.2.3 Anatomical Imaging Study

Ten mice (Group 1) were implanted with tumours on day 0, and then followed for 30 days to determine the rate of tumour growth and the extent of metastasis. Mice were scanned at baseline and on days 6, 13, 22 and 29 after tumour induction. The volume of the prostate and tumour were measured, the number of tumours in the prostate and abdomen were counted, and the lymph nodes were examined for morphological changes that might correspond to metastasis.

In order to histologically determine sites of metastasis early after tumour induction, six mice were included in a cross-sectional experiment. The mice were injected intraprostatically with PC-3M as above, then 3 mice were scanned on day 9 (Group 2a) and 3 mice were scanned day 13 (Group 2b). As before, mice were sacrificed and perfused with saline on the day after scanning.

4.2.4 Anatomical Magnetic Resonance Imaging

Mice were scanned on a clinical 3 Tesla GE MR750 whole body system equipped with a custom-built, high-performance insert gradient. Mice were anaesthetized with isoflurane in oxygen (2% for induction, ~1% during scanning as required) and placed within a solenoidal mouse body radiofrequency (RF) coil (4 cm long, 3 cm diameter). Whole mouse body images were acquired with the following 3D bSSFP imaging parameters:

200 μm spatial resolution in all three imaging planes, achieved with a 6 cm field of view and a 300x300 image matrix and a 200 μm slice thickness, repetition time/echo time (TR/TE)=4.7/2.3 ms, flip angle 30° or 50°, receiver bandwidth \pm 62.5 kHz, 2 signal averages and 4 phase cycles for a 24 minute scan. Tumour volumes were measured using Osirix (20). The prostate and tumour were manually segmented to create regions of interest (ROI); smaller tumours were segmented every 100 μm while larger tumours were segmented every \sim 300 μm , using the 'generate missing ROI' tool to automatically segment the intermediate slices. The auto-generated segmentations were verified and adjusted as required.

4.2.5 Spectroscopic Imaging

Six mice (Group 3) were scanned on day 22 after orthotopic PC-3M injection. Mice were scanned at 3T using a custom-built switch-tuned $^1\text{H}/^{13}\text{C}$ coil with a birdcage transmit and surface receive coils. Mice were anaesthetized with isoflurane as described above. A catheter (approximately 60 cm long) made from PE-20 tubing and tipped with a 30 gauge needle was placed in the tail vein and filled with heparinized saline. Temperature was maintained by circulating 42 °C water through the animal bed. Breathing was monitored (Small Animal Instruments Inc., Stony Brook, NY) and maintained between 30 and 80 breaths per minute. T_2 -weighted spin-echo (T_2 WSE) ^1H scans were performed in the axial and sagittal planes to localize the tumour with the parameters: \sim 400 μm in-plane resolution, 5 cm field of view, 128x128 image matrix, 3 mm slice thickness, TR/TE=4000/85 ms, echo train length 24, bandwidth \pm 10.42 kHz, 25 signal averages, 10 minute scan. For the spectroscopy acquisition, a 6-8 mm thick axial slab, depending on the tumour size, was placed based on the SE images. $[1-^{13}\text{C}]$ Pyruvate was polarized for 45 minutes using a HyperSense polarizer (Oxford Instruments, UK) then dissolved to a final concentration of 79 mM at a pH of 7.6. 300 μL of $[1-^{13}\text{C}]$ pyruvate was injected in a single bolus injection through the catheter over 12 seconds. 25 s after the start of the injection, a chemical shift image was acquired (6x6 cm field of view, 12x12 matrix, TR 80 ms, scan time 12 s) using the 2D FID-CSI sequence on the scanner. Spectra were analyzed using SAGE software provided by GE on the scanner. The spectra were apodized, zero-filled, and then Fourier transformed. The area of the lactate and pyruvate

peaks in the magnitude spectra was used to calculate the ratio of lactate to pyruvate (lac/pyr) in the tumour-containing voxels. Anatomical images of these mice were obtained on day 23 using the bSSFP sequence as described above.

4.2.6 Histology

Mice were sacrificed the day after their final imaging time point, on day 10, 14 or 30-31. About 30 minutes before sacrifice, ~5 μ L of Evans blue dye was injected SC into the hind footpads of the mice for visualization of the lymph nodes (Groups 1 and 2). Mice were sacrificed by intraperitoneal euthanyl injection and perfused with saline. Lymph nodes (popliteal, sciatic, iliac, renal, inguinal – for Group 2 only) as well as the spleen were removed and processed through a sucrose gradient (24 hours in formalin, 10%, 20% and 30% sucrose) for frozen sectioning at a thickness of 14 μ m. Sections from lymph nodes of one mouse from Group 1 (d30), Group 2a (d9) and Group 2b (d13) were randomly selected for detection of human cells using mouse anti-HuNu staining, which stains human nuclear membranes. Sections were blocked with goat serum, stained with mouse anti-HuNu primary antibody (Millipore) overnight, then the secondary antibody, goat anti-mouse IgG labeled with green fluorescent Alexa Fluor 488 (Invitrogen) was applied. Sections were cover slipped using mounting media containing DAPI (Vectashield, Vector Laboratories, Burlington, ON). A Zeiss Axio Imager microscope (Canada) with a Retiga EXi Digital CCD camera (Q Imaging, Vancouver, BC, Canada) was used to photograph the sections for a determination of the presence of human prostate cancer cells in the lymph nodes and spleens. Two to three slides containing four sections each were stained and examined for each node. Prostate tumours from Group 1 and 3 were similarly processed for frozen sectioning at 14 μ m and stained with hematoxylin and eosin (H&E) according to standard methods. Whole tumour sections were scanned using a TISSUEScope 4000 slide scanner (Huron Technologies, Waterloo, Canada).

4.2.7 Statistical Analysis

A one-way repeated measures analysis of variance with Tukey post-hoc tests was used to analyze the rate of tumour growth and the change in lymph node volume over time (GraphPad Prism 5.0, GraphPad, San Diego, CA). Because this analysis requires data from all time points, tumours and lymph nodes that were not clearly visible at one time point required the exclusion of all measurements of that tissue from the analysis. This restriction excluded 1/10 tumours, 3/20 iliac lymph nodes and 6/20 inguinal lymph nodes from the statistical analysis; however, volumes at the measurable time points are included in graphical representations of the data. To compare tumour volumes in the longitudinal and cross-sectional experiment, an unpaired 2-tailed student t-test with equal variances not assumed was performed (Microsoft Excel 2008). To compare lactate/pyruvate ratios between high and low uptake voxels, an unpaired 2-tailed t-test was used (GraphPad Prism).

4.3 Results

4.3.1 Tumour Appearance in MRI Images

The prostate and tumours were easily visualized and segmented in the bSSFP images (Figure 4.1). The prostate was discernible at baseline and day 6 by its position under the bladder and its shape but was engulfed by the tumour at later time points. In some images from early time points the healthy prostate is visible surrounding the tumour as a brighter tissue surrounding the darker tumour, as seen in Figure 4.1B. There were regions of signal hypo- and hyper-intensities in the tumours, likely caused by blood vessels and fluidic regions in the tumour, respectively. Hypointensities appear as discrete black dots in the image and appeared as early as day 6 after tumour injection and at all other imaging time points. Hyperintensities were visible as large patches of white in the centre of the tumour; they were present starting at day 22 in some tumours and appeared in most tumours on day 29.

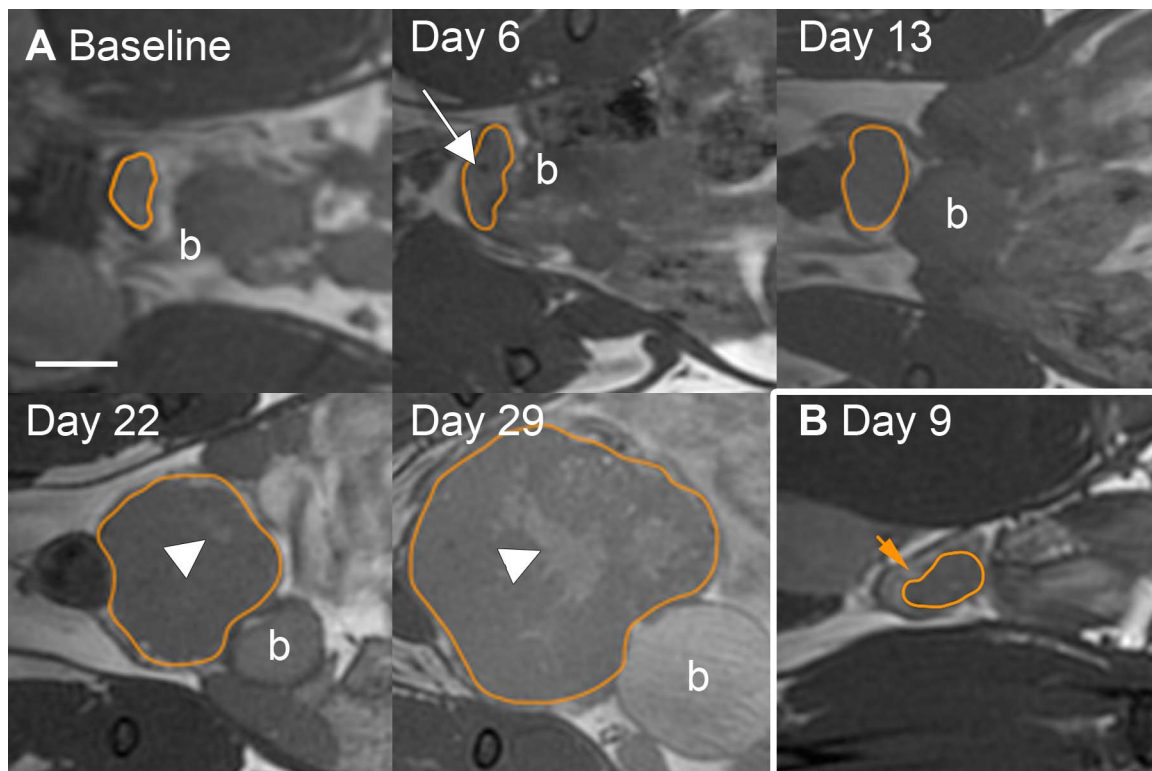


Figure 4.1: MR appearance and sample segmentation of the prostate and tumour over time.

A: Progression of tumour in one mouse over time (Group 1). B: Sample image of tumour on day 9 (Group 2a) with normal prostate tissue still visible (orange arrow). The tumour is outlined in orange; b indicates the bladder, white arrow indicates regions of hypointensity, white arrowhead regions of signal hyperintensity. Scale bar is 2.5 mm.

4.3.2 Tumour Volume

The volume of the ventral and lateral prostate plus tumour increased with time. At baseline, the mean volume was $7 \pm 2 \text{ mm}^3$, on day 6 it was $11 \pm 5 \text{ mm}^3$, on day 13 it was $51 \pm 30 \text{ mm}^3$, on day 22 it was $226 \pm 74 \text{ mm}^3$, and the mean final volume on day 29 was $720 \pm 190 \text{ mm}^3$ (Figure 4.2). The difference in volume from baseline was statistically significant on day 22 and day 29, although prostate tumours were clearly visible in the images by day 13. At day 6 and day 13, all mice had only one tumour in the prostate. By day 22, 4 mice had one tumour and 6 had multiple tumour lobes. On day 29, 3 mice had one tumour and 7 had multiple tumours. The additional tumour lobes tended to be located in the abdomen, superior and anterior to the prostate and bladder (Figure 4.3).

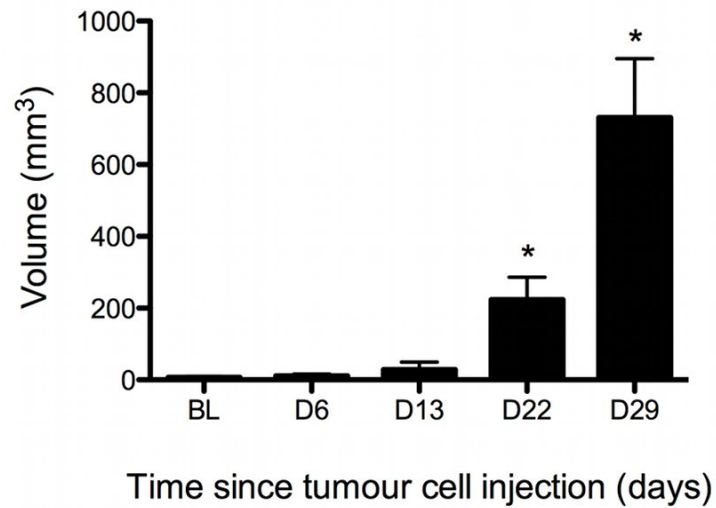


Figure 4.2: Tumour volume over time.

Volume of ventral/lateral lobes of prostate plus tumour was measured at each time point. BL = baseline measurement of prostate volume; *indicates significant difference from baseline prostate volume in a repeated measures analysis of variance ($p < 0.05$).

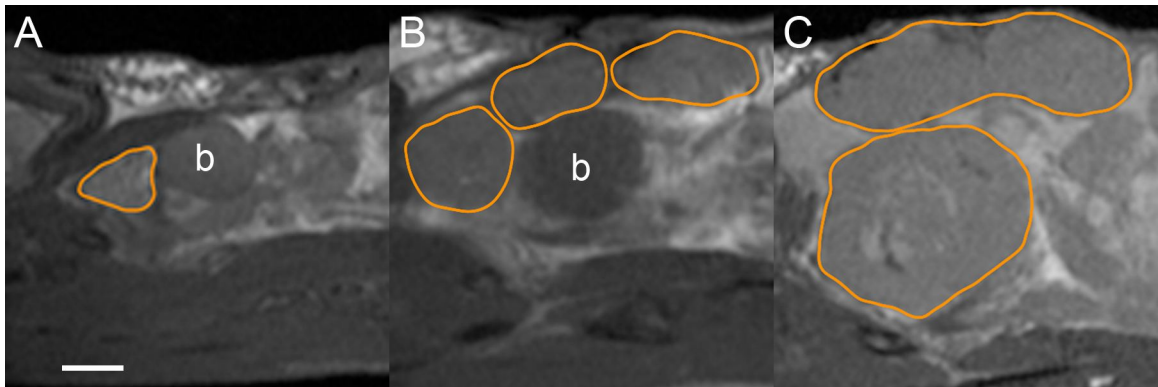


Figure 4.3: Distribution of multiple tumour lobes.

bSSFP images of a mouse in which the tumour had one lobe on day 13 (A), then 3 lobes by day 22 (B). On day 29 (C) all 3 lobes were larger. Sagittal view of mouse. b indicates the bladder. The prostate has been enveloped by the tumour. Scale bar is 2.5 mm.

Based on the consistent presence of tumours in the prostate by day 13 after PC-3M injection, a cross-sectional study was conducted to determine the tumour size and presence of tumour cells in the lymph nodes on day 9 and day 13. Our previous experiments with histology of subcutaneous tumours (9) have shown that NK are expected to be present in the tumour 3-5 days after intravenous and intraperitoneal administration, so a time-point 4 days before day 13 was selected as it would be a potential window for IV therapy administration.

On day 9 of the cross-sectional study, 3/3 mice had prostate tumours, with a mean volume of $20 \pm 14 \text{ mm}^3$. On day 13, 2/3 mice had measurable tumours, with a mean volume of $39 \pm 16 \text{ mm}^3$ (mean of 2 tumours). These values are not significantly different from the mean tumour volume in the longitudinal experiment on day 13 ($p=0.5$).

4.3.3 Lymph Node Histology

One mouse from day 30 (Group 1), day 9 and day 13 (Group 2) was selected for histological examination for the presence of human cells in lymph nodes (Figure 4.4). The results are summarized in Table 4.1). The iliac lymph node was the only node with PC-3M cells present on day 9 and was the only node where the cells were present at all time points. On day 13, the iliac and renal nodes had human cells. All lymph nodes from the mouse sacrificed on day 30 had PC-3M cells in them. The PC-3M cells were distributed in the center of the nodes, in what would be the T-cell region in mice with intact immune systems.

Table 4.1: Summary of locations where prostate cancer cells were detected.

Selected sections from one mouse at each time point were stained for Hu/Nu. + indicates that PC-3M cells were detected in the node/spleen by fluorescence microscopy, - indicates no cells were detected. Nd indicates not done, because the nodes were not collected.

Time	Spleen	Iliac	Popliteal	Sciatic	Renal	Inguinal
Day 9	+	+	-	-	nd	-
Day 13	+	+	+	-	+	-
Day 30	+	+	+	+	+	nd

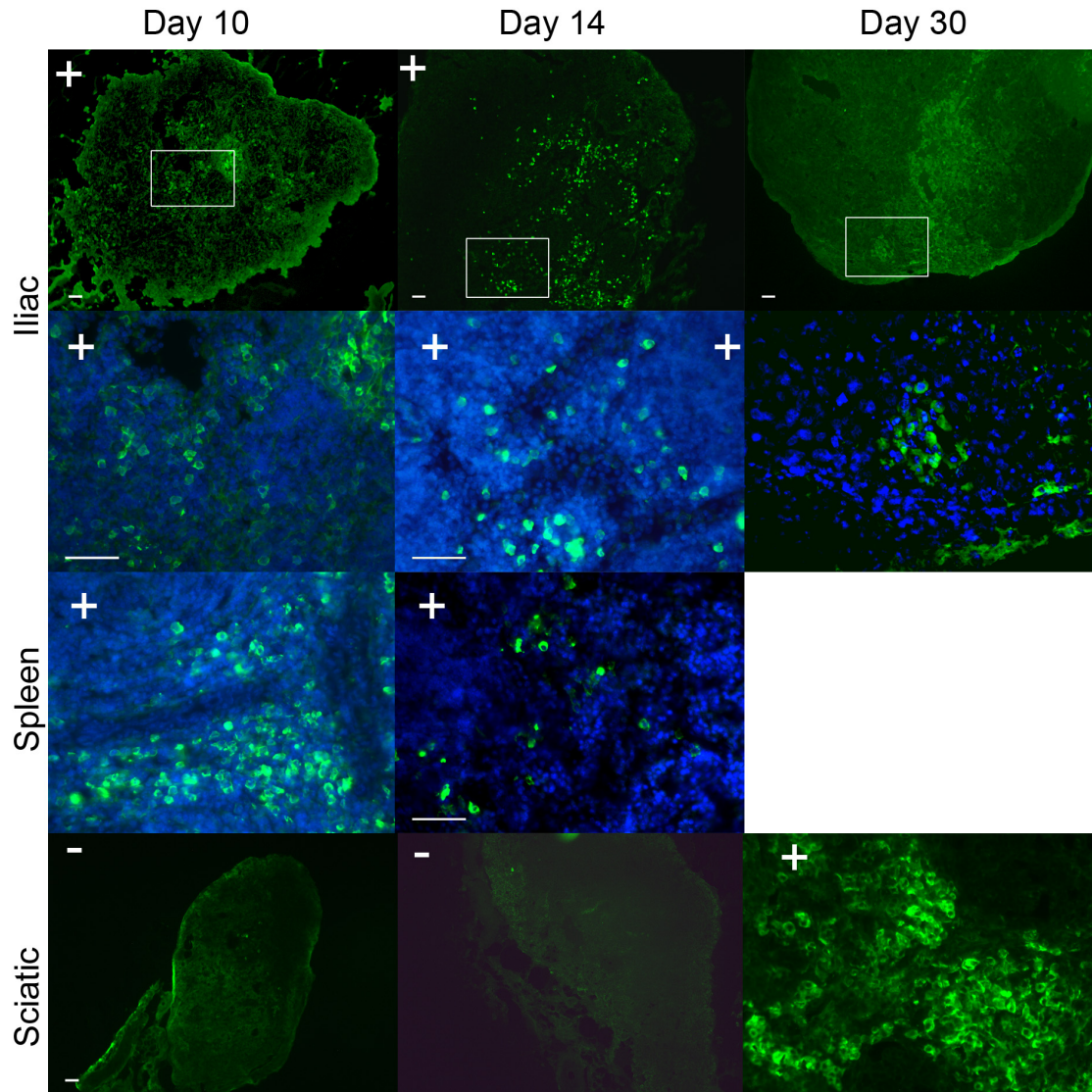


Figure 4.4: Presence of PC-3M in lymph nodes and spleens.

Lymph nodes and spleen sections were stained with HuNu (human cells, green) and DAPI (all nuclei, blue). This is a selection of lymph nodes and spleen sections from all time points in which PC-3M were detected (+) and not detected (-). For the iliac lymph nodes, 2 magnifications are presented to show distribution of the cells; the white box indicates the section that is magnified in the row below. Scale bars are 50 μm .

4.3.4 MR appearance of metastatic lymph nodes

Other than size, there were no gross differences in MR appearance or at necropsy between metastatic and non-metastatic lymph nodes. Figure 4.5 shows the appearance of the iliac lymph node over time in a representative mouse. The volume of this node, which contained PC-3M cells upon histological examination on day 30, increased with time.

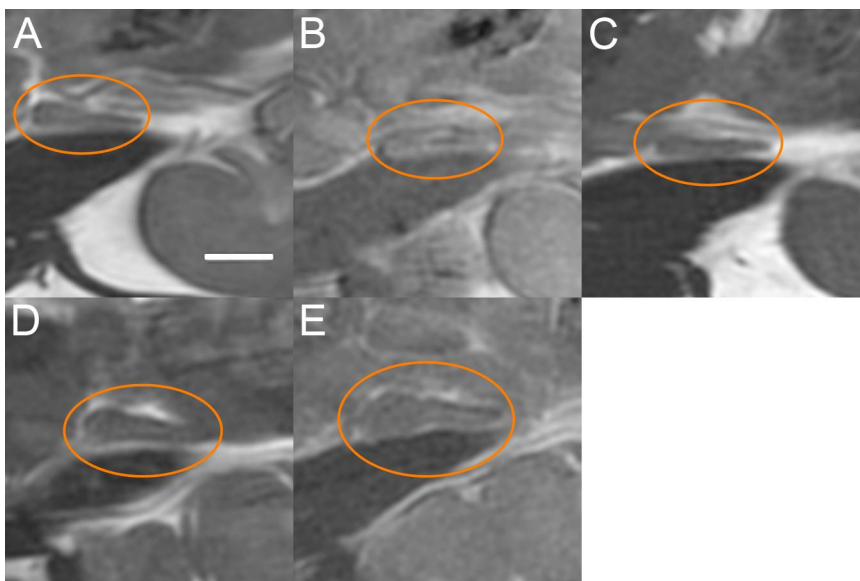


Figure 4.5: MR appearance of the iliac lymph node over time.

Magnified views of the iliac lymph node in coronal images from one mouse (Group 1) at baseline (A), day 6 (B), day 13 (C), day 22 (D) and day 29 (E). The node (circled in orange) increases in size, particularly in the last 2 imaging time points, but there are no changes in the contrast of the node itself. Scale bar is 2.5 mm.

When the volume of all iliac lymph nodes for all mice in the longitudinal experiment was measured, there was a significant increase in lymph node size on day 29 compared to all other time points (Figure 4.6a). For the inguinal lymph nodes, where metastasis is not expected, there was no trend to increasing size over time (Figure 4.6b).

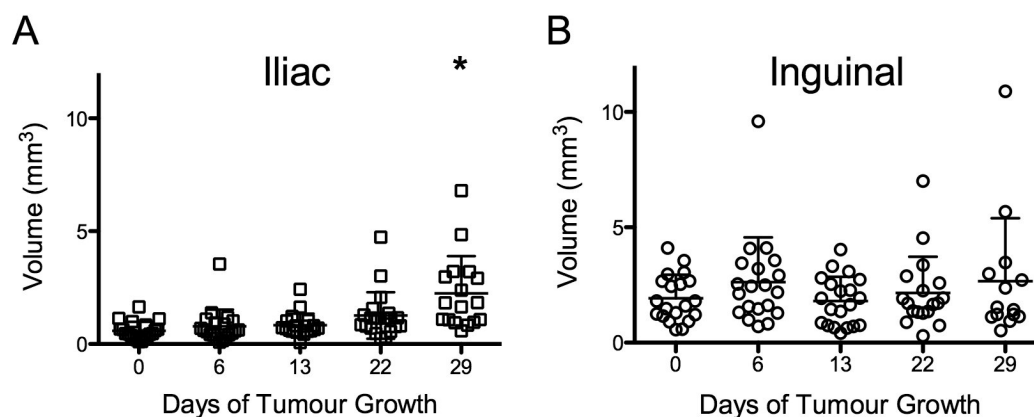


Figure 4.6: Volumes of iliac and inguinal lymph nodes over time.

Volumes of the iliac (A) and inguinal (B) lymph nodes for each time point in mice from Group 1. The volume of the iliac lymph nodes increased over time and was significantly different on day 29 than all other time points. There was no significant difference in inguinal lymph node volume over time. Volumes of all measurable nodes are presented (including nodes that were excluded from the analysis because of incomplete data at some time points). Horizontal lines indicate mean node volume, error bars are standard deviation (upper bound only), *= significant difference, $p < 0.05$, relative to baseline.

4.3.5 Pyruvate Metabolism

On day 22, the mean volume of the tumours was $290 \pm 110 \text{ mm}^3$. The mean lac/pyr ratio of the 6 tumours was 1.2 ± 0.5 . Values of lac/pyr were heterogeneous in the tumours, with coefficients of variation ranging from 20% to 80%. The amount of signal varied between tumour voxels. Voxels were visually categorized as high or low uptake based on the relative total height of the pyruvate and lactate peaks across all tumour voxels; the low-uptake voxels tended to be in the middle of the tumours, with the high-uptake voxels around the edge (Figure 4.7). When all high-uptake voxels were compared to the low-uptake voxels, there was a trend to the low-uptake voxels having a higher lac/pyr ratio than the high-uptake voxels (unpaired t-test, $p = 0.07$) (Figure 4.8). Low uptake voxels corresponded to regions with bright signal on the bSSFP images, which indicates the presence of fluid. These also corresponded to regions in the histology that showed necrosis, as indicated by regions of low cell density in the middle of the tumour (Figure 4.9).

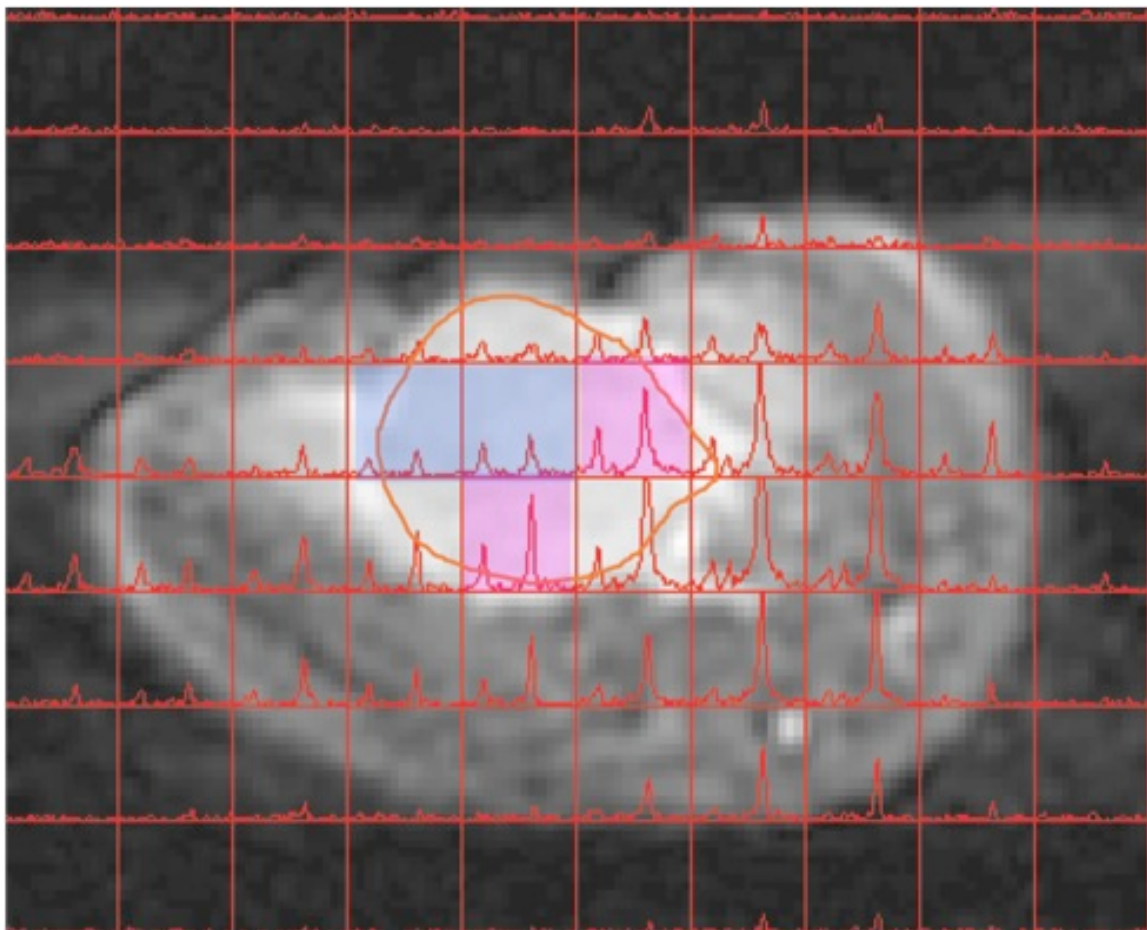


Figure 4.7: Sample image of lactate/pyruvate spectrum in a tumour with variable uptake.

The spectra are shown in red overlaid on the axial T_2 weighted anatomical image of the mouse at the level of the prostate. In each spectrum, the left peak is the lactate peak and the right peak is the pyruvate peak. Tumour is outlined in orange. Voxels shaded in pink were categorized as high uptake while those shaded in blue are low uptake. Only voxels comprised entirely of tumour were included in the analysis. Voxels are 3.3 x 3.3 x 8 mm.

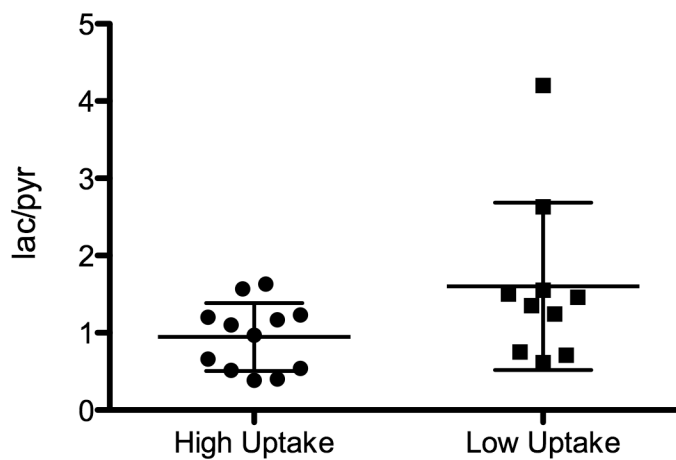


Figure 4.8: Comparison of lactate/pyruvate ratio in voxels with high and low pyruvate and lactate signal.

All tumour voxels were included in the analysis and categorized as having a high or low total uptake of pyruvate and lactate. There was a trend to a significant difference between low and high uptake voxels ($p=0.07$).

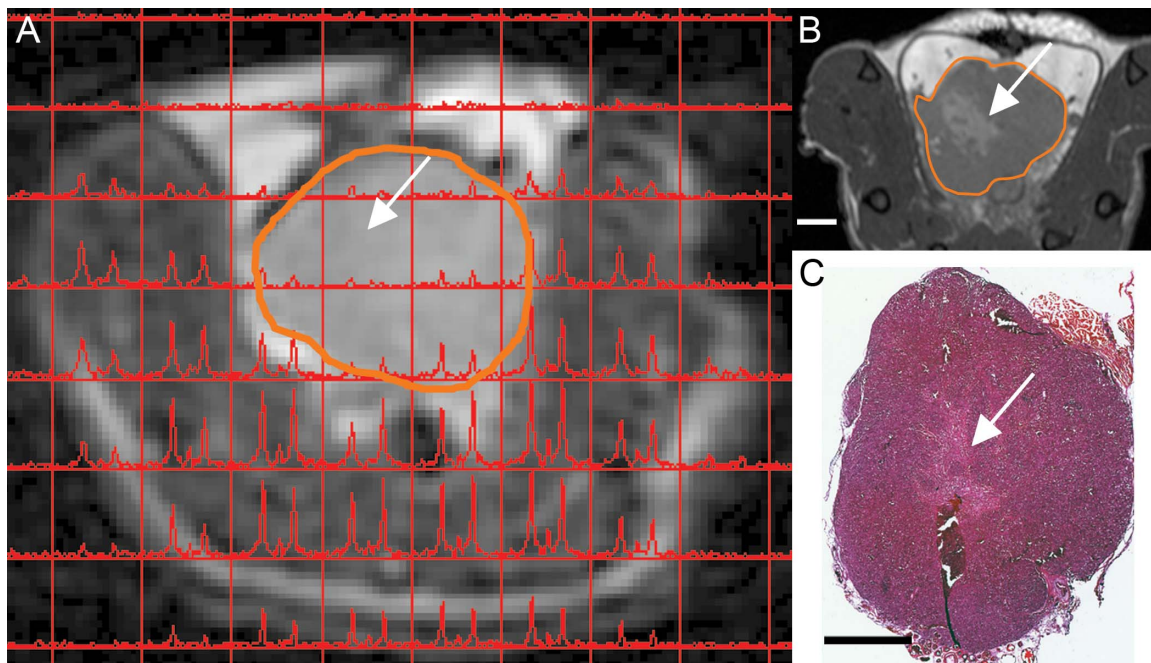


Figure 4.9: Comparison of spectroscopy, bSSFP and histology.

(A) Spectrum (red) overlaid on axial T_2 WSE image (day 22). B: bSSFP image of same mouse (day 23). C: Tumour section (day 25) stained with H&E. The upper left part of the tumour has a low total signal image in the spectrum from day 22, a white, fluidic region in the day 23 anatomical image and necrosis in the day 25 histological section (white arrows). Tumour is outlined in orange. Voxels are $3.3 \times 3.3 \times 8$ mm and scale bars are 2.5 mm.

4.3.6 Sample Size Calculation

A standard sample size calculation was performed to calculate the number of mice required to see a therapeutic effect with pyruvate metabolism data using a t-test:

$$n = \frac{4\sigma^2(Z_\alpha + Z_\beta)}{\Delta^2} \quad (4)$$

where n is the total number of animals, σ is the standard deviation of the measurements, Z_α is the significance criterion, Z_β is the power value and Δ is the desired difference between groups to be measured. In this case, σ was 0.5, $Z_\alpha = 1.960$ for a p value of 0.05, Z_β is 0.842 for a power of 80% (21), and Δ is 0.6, taken from a paper in which the difference in lac/pyr between treated and untreated tumours one day after temozolamide

treatment was 50% (13). With these values, the number of mice required is 22, or 11 per group (treated and untreated).

4.4 Discussion

We have described the growth and metabolism of orthotopic PC-3M tumours in nude mice. Tumour take rate was 21/22 mice (including the longitudinal, cross sectional and spectroscopy experiments). The MR appearance of orthotopic PC-3M tumours included both hyper- and hypo-intense regions, which correspond to regions with necrosis and hemorrhage, respectively. Tumour volume increased with time to an average of $720 \pm 190 \text{ mm}^3$ on day 29. A full summary of previous orthotopic PC-3 and PC-3M studies is presented in Table 4.2. In previously reported experiments with intraprostatic PC-3 tumours, tumour volumes of approximately $400\text{-}500 \text{ mm}^3$ were observed after 4 weeks of tumour growth; however, volumes as low as $50\text{-}70 \text{ mm}^3$ were also reported. PC-3M and PC-3 cells have been injected into the prostate in studies where palpitation is used primarily to monitor tumour progression and *ex vivo* measurement of tumour volume is performed at necropsy. Cells can be transfected with luciferin and bioluminescence measured as a surrogate for tumour volume eg (22,23). There have been no studies to date that have directly measured the volume of intraprostatic PC-3M tumours; volume of PC-3M tumours has only been provided from an extrapolation based on bioluminescence intensity as 1100 mm^3 (24).

Metastasis was seen in the iliac lymph node on days 9, 13 and 30 using histology in this study. Metastasis in more distant lymph nodes was seen at later time points. This agrees with previous experiments where metastases from orthotopically implanted PC-3 and PC-3M cells have been observed in the draining nodes of the prostate, in the lungs and, more rarely, in bone after tumour growth times of 4-8 weeks (Table 4.2). One study using bioluminescence imaging (BLI) appeared to show metastatic spread to the inguinal lymph node on day 21 after implantation (23). We did not observe PC-3M cells in the inguinal node in this experiment on day 9 or day 13, but those nodes were not collected on day 29 so it is not known whether in our model there is the potential for PC-3M to

spread to inguinal lymph nodes. The lungs and bone were not examined histologically in this study but there were no abnormal MRI findings in the bone or lungs of the mice. The determination of metastasis was limited by the fact that only a small subset of all lymph nodes was examined histologically for PC-3M cells.

Because the iliac lymph node was positive for PC-3M cells in all 3 mice that were examined histologically, the volume of this node was evaluated over time in mice from Group 1. The mean volume was larger on day 29 than it was at baseline. To attempt to rule out the possibility that this was due to growth of the mice, the volume of the inguinal lymph node was also measured and did not vary with time. It is tempting to attribute the increase in iliac lymph node volume to the presence of metastases; however, other factors such as node reactivity, i.e. proliferation of immune cells due to a pathogen in the mouse body can change the volume of lymph nodes. As well, previous studies have demonstrated that nodes may be metastatic without increasing in size and may increase in size without being metastatic, so a change in lymph node volume cannot be over-interpreted as due to metastasis (25). The nu/nu strain used in this study is maintained as an outbred strain which may contribute to size variability. There is the potential to detect metastatic lymph nodes using pyruvate spectroscopy in future work; lymph node metastases of 100 mm³ have been detected in TRAMP mice (11).

We obtained lactate/pyruvate spectra for tumours on day 22 using hyperpolarized ¹³C-labeled pyruvate. This is the first report of this technique being used in a xenograft model of prostate cancer. The mean lac/pyr ratio was 1.2 ± 0.5 on day 29. A sample size calculation indicated that in order to be sensitive to 50% changes in lac/pyr ratio with treatment, 11 mice per group would be required. In TRAMP mice, lac/pyr values of 1.1 – 3.1 have been reported in low- and high-grade tumours, respectively (11). These values are not precisely equivalent to the results reported here, because in the TRAMP study the spectra were acquired 35 seconds after the start of the pyruvate injection as compared to 24 seconds in our study, resulting in more lactate conversion due to the longer delay time. We observed heterogeneous uptake of pyruvate in the tumours, with low uptake voxels corresponding to necrotic regions as determined by bSSFP imaging and histology. There was still some signal in these large spectroscopic voxels, likely because there was still

some viable tissue present; however, the lac/pyr ratio was higher, indicating a more advanced tumour. In TRAMP tumours, a higher grade of tumour corresponds to a higher lactate/pyruvate ratio (11).

In our experiment, tumours were visible using MRI by day 9 and on day 13, and there was no necrosis, as indicated by the lack of hyperintensities in the MRI images. This indicates that day 9-13 could be a suitable time point for therapeutic injection of NK cells, either intravenously or intraperitoneally. This is consistent with the timeline used in a similar model for gemcitabine treatment (26). In our study, the MRI appearance of the tumours throughout their development included spots of hypointensity. Because of these hypointensities, a subtle change in MR signal due to iron-oxide labeled NK cells could be confused with a naturally-occurring signal void so caution must be used in interpreting results. However, it is usually possible to trace the path of blood vessels through the images so this not a major concern. Metastasis was seen in all draining lymph nodes of the prostate at later time points by histology, but only in proximal lymph nodes at early time points.

In summary, in this prostate cancer model, tumours were visible by MRI 9 days after tumour cell implantation, and we observed the presence of PC-3M in the iliac lymph nodes as early as day 9 after tumour cell injection, with more lymph nodes involved in later time points. Necrosis was present at day 22, and large tumours required sacrifice of the mouse by about day 30. Based on these results, this model could be used for studying NK therapy as early as day 9 after cells are injected and would allow for the determination of the effect of NK treatment on primary tumour development and metastasis.

Table 4.2: Summary of previous PC-3 and PC-3M tumour growth and metastasis

Mouse type	Cells	Injection site	No. of cells	Time to tumour measurement	% Engraftment	Volume/Mass	Time to met. measurement	% with met.	Site of met.	Method of met. detection	Source
Nude 8 weeks	PC-3M	D	2×10^6	60 days	1 of 2		60 days	1 of 2	Pre-aortic/iliac lymph node		(27)
Nude 8-10 weeks	PC-3M	DL	5×10^5	60 days			60 days		Para-lumbar/para-aortic lymph nodes	H&E	(28)
Nude 8 weeks	PC-3M	P	1×10^6		9/9		32 days	6/9	Lymph node	H&E	(19)
Nude	PC-3M	V	1×10^6	40 days	100		40 days	100	mesenteric lymph node	Mass of nodes	(29)
Nude 5-6 weeks	PC-3M-luc-C6	DL	5×10^5	4 weeks		$\sim 1100 \text{ mm}^3$ †					(24)
Nude 8-10 weeks	PC-3M-luc-C6	DL	5×10^5	5 weeks	11/13	350 mg	3 – 5 weeks	6/11	Regional lymph nodes	BLI <i>in vivo</i>	(23)
Nude 6 weeks	Pc-3MsLUC	P	5×10^5	18 days	100%	1205.3 g	18 days	100%	Lymph nodes, lungs, bones, sexual organs	BLI of organ homogenates	(22)
NOD/SCID	PC-3	O	1×10^6		83%		8-9 weeks	70%		Visual inspection	(18)
Nude	PC-3	O	5×10^5		100%		60 days	100%	lymph node, kidney, lung	H&E	(30)
Nude 6 weeks	PC-3	O	2×10^6	7 weeks	100%						(31)

Mouse type	Cells	Injection site	No. of cells	Time to tumour measurement	% Engraftment	Volume/Mass	Time to met. measurement	% with met.	Site of met.	Method of met. detection	Source
Nude 12 weeks	PC-3	O	5×10^5		6/14 after 4 weeks 9/14 after 8 weeks	4 weeks ~400mm ³ 8 weeks ~1500mm ³	8 weeks	7/9 mice	regional lymph nodes	H&E	(32)
Nude 8 weeks	PC-3	D	5×10^5	4 weeks	13/16 mice	500 mm ³	4 weeks	7/13 mice	iliac and sacral lymph nodes	H&E	(33)
Nude 8 weeks	PC-3	O	5×10^5	4 weeks		47 mm ³	4 weeks	58% 8%	iliac and sacral lymph nodes Lungs	H&E	(34)
Nude 4-6 weeks	PC-3	D	1×10^6	4 weeks		~1.5 g					(35)
Nude	PC-3	A	1×10^6	30-35 days	~ 95-100%	375±330 mm ³	30-35 days	100%	spleen, lung, liver, lymph nodes, femur, spine	<i>In vitro</i> BLI	(26)
Nude	PC-3	O	1×10^5	42 days	100%	21 d 70 mm ³ 42d 120 mg	42 days		44.2% invasion of lymph nodes	H&E and immunohistochemistry	(36)
Nude 8-12 weeks	PC-3	D	1×10^6	45 days	100%	1.1 g	45	3/5 1/5	lymph nodes lungs	H&E	(17)

D: dorsal lobe, DL: dorsolateral lobe, P: posterior lobe, A: anterior lobe, V: ventral lobe, O no lobe specified (orthotopic). A blank cell indicates that the data was not provided. † - interpolated from data of bioluminescence measurement and provided calibration curve. Often the specific lymph nodes examined were not specified.

4.5 References

1. Canadian Cancer Society Steering Committee. Canadian cancer statistics 2010.
2. Siegel R, Naishadham D, Jemal A. Cancer statistics, 2012. *CA Cancer J Clin* 2012;62(1):10-29.
3. Greenberg NM, DeMayo F, Finegold MJ, Medina D, Tilley WD, Aspinall JO, et al. Prostate cancer in a transgenic mouse. *Proceedings of the National Academy of Science USA* 1995, Apr;92(8):3439-43.
4. Kwabi-Addo B, Giri D, Schmidt K, Podsypanina K, Parsons R, Greenberg N, Ittmann M. Haploinsufficiency of the pten tumor suppressor gene promotes prostate cancer progression. *Proc Natl Acad Sci U S A* 2001, Sep 25;98(20):11563-8.
5. Eng MH, Charles LG, Ross BD, Chrisp CE, Pienta KJ, Greenberg NM, et al. Early castration reduces prostatic carcinogenesis in transgenic mice. *Urology* 1999, Dec;54(6):1112-9.
6. Hsu CX, Ross BD, Chrisp CE, Derrow SZ, Charles LG, Pienta KJ, et al. Longitudinal cohort analysis of lethal prostate cancer progression in transgenic mice. *J Urol* 1998, Oct;160(4):1500-5.
7. Kumar AP, Bhaskaran S, Ganapathy M, Crosby K, Davis MD, Kochunov P, et al. Akt/camp-responsive element binding protein/cyclin D1 network: A novel target for prostate cancer inhibition in transgenic adenocarcinoma of mouse prostate model mediated by nexrutine, a phellodendron amurense bark extract. *Clin Cancer Res* 2007, May 1;13(9):2784-94.
8. Stoyanova R, Hachem P, Hensley H, Khor LY, Mu Z, Hammond ME, et al. Antisense-MDM2 sensitizes Incap prostate cancer cells to androgen deprivation, radiation, and the combination in vivo. *Int J Radiat Oncol Biol Phys* 2007, Jul 15;68(4):1151-60.

9. Mallett CL, Foster PJ. Optimization of the balanced steady state free precession (bssfp) pulse sequence for magnetic resonance imaging of the mouse prostate at 3T. *PLoS One* 2011;6(4):e18361.
10. Kurhanewicz J, Vigneron DB, Brindle K, Chekmenev EY, Comment A, Cunningham CH, et al. Analysis of cancer metabolism by imaging hyperpolarized nuclei: Prospects for translation to clinical research. *Neoplasia* 2011, Feb;13(2):81-97.
11. Albers MJ, Bok R, Chen AP, Cunningham CH, Zierhut ML, Zhang VY, et al. Hyperpolarized ¹³C lactate, pyruvate, and alanine: Noninvasive biomarkers for prostate cancer detection and grading. *Cancer Res* 2008, Oct 15;68(20):8607-15.
12. Day SE, Kettunen MI, Gallagher FA, Hu DE, Lerche M, Wolber J, et al. Detecting tumor response to treatment using hyperpolarized ¹³C magnetic resonance imaging and spectroscopy. *Nat Med* 2007, Nov;13(11):1382-7.
13. Park I, Bok R, Ozawa T, Phillips JJ, James CD, Vigneron DB, et al. Detection of early response to temozolomide treatment in brain tumors using hyperpolarized ¹³C MR metabolic imaging. *J Magn Reson Imaging* 2011, Jun;33(6):1284-90.
14. Chen AP, Chu W, Gu YP, Cunningham CH. Probing early tumor response to radiation therapy using hyperpolarized [1-(¹³C)]pyruvate in MDA-MB-231 xenografts. *PLoS One* 2013;8(2):e56551.
15. Kaighn ME, Narayan KS, Ohnuki Y, Lechner JF, Jones LW. Establishment and characterization of a human prostatic carcinoma cell line (PC-3). *Invest Urol* 1979, Jul;17(1):16-23.
16. Kozlowski JM, Fidler IJ, Campbell D, Xu Z, Kaighn ME, Hart IR. Metastatic behavior of human tumor cell lines grown in the nude mouse. *Cancer Res* 1984, Aug;44(8):3522-9.
17. Rembrink K, Romijn JC, van der Kwast TH, Rübber H, Schröder FH. Orthotopic implantation of human prostate cancer cell lines: A clinically relevant animal model for metastatic prostate cancer. *Prostate* 1997, May 15;31(3):168-74.

18. Bastide C, Bagnis C, Mannoni P, Hassoun J, Bladou F. A nod scid mouse model to study human prostate cancer. *Prostate Cancer Prostatic Dis* 2002;5(4):311-5.
19. Stephenson RA, Dinney CPN, Gohji K, Ordonez NG, Killion JJ, Fidler IJ. Metastatic model for human prostate cancer using orthotopic implantation in nude mice. *JNCI Journal of the National Cancer Institute* 1992;84(12):951.
20. Rosset A, Spadola L, Ratib O. OsiriX: An open-source software for navigating in multidimensional DICOM images. *J Digit Imaging* 2004, Sep;17(3):205-16.
21. Eng J. Sample size estimation: How many individuals should be studied? *Radiology* 2003, May;227(2):309-13.
22. El Hilali N, Rubio N, Blanco J. Different effect of paclitaxel on primary tumor mass, tumor cell contents, and metastases for four experimental human prostate tumors expressing luciferase. *Clin Cancer Res* 2005, Feb 1;11(3):1253-8.
23. Jenkins DE, Yu SF, Hornig YS, Purchio T, Contag PR. In vivo monitoring of tumor relapse and metastasis using bioluminescent pc-3m-luc-c6 cells in murine models of human prostate cancer. *Clin Exp Metastasis* 2003;20(8):745-56.
24. Casarez EV, Dunlap-Brown ME, Conaway MR, Amorino GP. Radiosensitization and modulation of p44/42 mitogen-activated protein kinase by 2-methoxyestradiol in prostate cancer models. *Cancer Res* 2007, Sep 1;67(17):8316-24.
25. Economopoulos V, Chen, McFadden C, Foster PJ. MRI detection of nonproliferative tumor cells in lymph node metastases using iron oxide particles in a mouse model of breast cancer. *Translational Oncology* (in press).
26. Jantscheff P, Esser N, Graeser R, Ziroli V, Kluth J, Unger C, Massing U. Liposomal gemcitabine (gemlip)-efficient drug against hormone-refractory du145 and PC-3 prostate cancer xenografts. *Prostate* 2009, Aug 1;69(11):1151-63.
27. Chu JH, Sun ZY, Meng XL, Wu JH, He GL, Liu GM, Jiang XR. Differential metastasis-associated gene analysis of prostate carcinoma cells derived from primary

tumor and spontaneous lymphatic metastasis in nude mice with orthotopic implantation of PC-3M cells. *Cancer Lett* 2006, Feb 20;233(1):79-88.

28. Sehgal I, Foster TP, Francis J. Prostate cancer cells show elevated urokinase receptor in a mouse model of metastasis. *Cancer Cell Int* 2006;6:21.

29. O'Reilly T, McSheehy PM, Wenger F, Hattenberger M, Muller M, Vaxelaire J, et al. Patupilone (epothilone B, EPO906) inhibits growth and metastasis of experimental prostate tumors in vivo. *Prostate* 2005, Nov 1;65(3):231-40.

30. Waters DJ, Janovitz EB, Chan TC. Spontaneous metastasis of PC-3 cells in athymic mice after implantation in orthotopic or ectopic microenvironments. *Prostate* 1995, May;26(5):227-34.

31. Singh RP, Raina K, Deep G, Chan D, Agarwal R. Silibinin suppresses growth of human prostate carcinoma PC-3 orthotopic xenograft via activation of extracellular signal-regulated kinase 1/2 and inhibition of signal transducers and activators of transcription signaling. *Clin Cancer Res* 2009, Jan 15;15(2):613-21.

32. Valta MP, Tuomela J, Vuorikoski H, Lojonen N, Väänänen RM, Pettersson K, et al. FGF-8b induces growth and rich vascularization in an orthotopic PC-3 model of prostate cancer. *J Cell Biochem* 2009, Jul 1;107(4):769-84.

33. Tuomela JM, Valta MP, Väänänen K, Härkönen PL. Alendronate decreases orthotopic PC-3 prostate tumor growth and metastasis to prostate-draining lymph nodes in nude mice. *BMC Cancer* 2008;8:81.

34. Tuomela J, Valta M, Seppänen J, Tarkkonen K, Väänänen HK, Härkönen P. Overexpression of vascular endothelial growth factor C increases growth and alters the metastatic pattern of orthotopic PC-3 prostate tumors. *BMC Cancer* 2009;9:362.

35. Shankar S, Ganapathy S, Srivastava RK. Sulforaphane enhances the therapeutic potential of TRAIL in prostate cancer orthotopic model through regulation of apoptosis, metastasis, and angiogenesis. *Clin Cancer Res* 2008, Nov 1;14(21):6855-66.

36. Vandyke K, White MY, Nguyen-Khuong T, Ow K, Luk SC-W, Kingsley EA, et al. Plant-Derived MINA-05 inhibits human prostate cancer proliferation *in vitro* and lymph node spread *in vivo*. *Neoplasia* 9(4):322-31.

Chapter 5

5 Summary and Future Work

5.1 Conclusions

Prostate cancer is the most diagnosed and second most deadly cancer in North American men (1). Several immunotherapies are currently under investigation to treat metastatic castration-resistant prostate cancer (2). The purpose of this project was to use MRI to study NK cell therapy in a mouse model of prostate cancer. This work used a novel NK cell line (KHYG-1) in SC and orthotopic mouse models of prostate cancer. The KHYG-1 were labeled with an iron oxide contrast agent, an MR pulse sequence was optimized and the model was characterized using anatomical and metabolic MRI.

In Chapter 2, NK cells were labeled with Molday-Rhodamine, an iron oxide contrast agent, and administered in a subcutaneous (SC) model of prostate cancer. Iron oxide-labeled NK cell migration to tumours was detected by histology for IV, IP and SC injections of the cells. However, iron-labeled NK cells were only detected by MRI in regions with a large concentration of labeled cells in the periphery of tumours, after SC injection of KHYG-1, and not for more sparsely distributed cells in the centre of tumours, which occurred after IV and IP administration. In a subsequent experiment, KHYG-1 were injected directly into SC tumours; there was a significant difference in tumour growth between the treated and control tumours. This presents a proof of concept that if systemically administered cells reach the tumour in sufficient numbers, there is the potential to see a treatment effect. There are several novel aspects to this work: (i) this was the first time that the KHYG-1 cell line was labeled with an iron oxide nanoparticle (ii) there are no other published reports of the *in vivo* administration of the KHYG-1 cell line in a tumour model, (iii) this is the first study to track the KHYG-1 cell line *in vivo* in a tumour model, and the first to use MRI to visualize tumour accumulation of a non-targeted NK cell line *in vivo*.

In Chapter 3, the bSSFP sequence was optimized for imaging the normal mouse prostate. The flip angle, bandwidth, phase cycling and excitations were adjusted to obtain the

maximum SNR while also minimizing artifacts such as chemical shift and banding. When compared with 2D T_1 WSE and T_2 WSE sequences with similar scan times, the SNR for the bSSFP sequence was superior. As well, the optimized bSSFP images were acquired in under 30 minutes and allowed for visualization of the prostate as well as lymph nodes that are potential sites of metastasis.

This pulse sequence was then applied to characterize an orthotopic mouse model of prostate cancer in Chapter 4. The growth rate of the primary tumour and its appearance in MR images was described. Histology was used to determine sites of metastasis; the iliac lymph node was metastatic in all examined mice. This information was consolidated to determine that in future cell tracking experiments, treatment with iron-oxide labeled NK cells should begin around day 9-13 after the injection of tumour cells to provide the opportunity to monitor cell tracking to tumours, tumour growth, and metastasis. As well, hyperpolarized ^{13}C pyruvate MR spectroscopy was used to examine tumour metabolism. This is the first reported use of hyperpolarized ^{13}C spectroscopy in a xenograft model of prostate cancer.

In this work we have demonstrated that tracking NK cells labeled with MoldayRhodamine is feasible, and showed that they accumulate in prostate cancer tumours in mice. We can image the mouse prostate and surrounding lymph nodes with bSSFP, and have used this sequence to characterize the growth of orthotopic PC-3M tumours in nude mice, as well as using histology to detect lymph node and splenic metastases. This model can now be used in future studies to examine NK cell tracking in the orthotopic model.

5.2 Future Work

Future work may expand on the model development and initial cell tracking work presented in this thesis. The focus will be on applying cell tracking in the orthotopic model, in metastatic models, exploring the use of other imaging techniques and expanding on which hyperpolarized metabolites are used.

5.2.1 NK Cell Dose Optimization

The iron oxide labeled KHYG-1 can be administered in the orthotopic model of prostate cancer. Using labeled KHYG-1 would allow the determination of the time taken for the NK cells to migrate to the tumours. As well, because the MR images acquired with bSSFP also include most of the body (from the hind limbs to the bottom of the lungs), NK can be tracked to lymph nodes as well as other organs such as the spleen and liver to determine biodistribution *in vivo*. The first step in this experiment would be to change the imaging parameters of the bSSFP sequence to make it more sensitive to SPIO than it was in Chapter 2. This would be achieved by injecting labeled NK cells IV into mice with SC tumors, since we have established that KHYG-1 will migrate to those tumours. Then the imaging parameters would be optimized by increasing TR and decreasing the voxel size, with starting values of 10 ms and 100x100x200 μm to start.

Once the imaging parameters are optimized, the next step is to determine the optimal route of injection. We found there was NK cell migration to SC tumours after IV injection, but there was high mortality with this route of administration due to cell trapping in the lungs. This could be resolved by testing the effect of injecting cells into the left ventricle of the heart (IC), so that they are distributed to the rest of the body before reaching the lungs. Accumulation in the tumour and other sites of interest over time could be monitored using the new optimized sequence.

The next question to answer would be whether there is an optimal number of cells to be administered and if there is an increase in the accumulation of NK cells in the tumor following injection of multiple doses. In patients, NK cells have been administered in one dose (3,4) or multiple doses (5). In order to test this in a mouse model, NK cells could be injected, the mice scanned to determine if the degree of signal increases reflecting the presence of migrated NK cells, then another dose could be injected and then the mice scanned again to determine if more NK cells have tracked to the tumour. A similar procedure could be followed to determine if there is a difference in accumulation following the injection of different numbers cells, which could then be scaled up for human clinical trials of NK therapy. A disadvantage of this approach is that it is only semi-quantitative. The tumour image may be obliterated by the blooming artifact as

labeled KHYG-1 accumulate in the tumour. This problem could be solved by reducing the SPIO sensitivity of the MRI sequence by reducing TR, or by injecting mixed populations of labeled and unlabeled cells to reduce the size of the blooming artifact.

5.2.2 Metabolic Imaging

In this thesis, pyruvate was used to monitor tumour metabolism in terms of the conversion of pyruvate to lactate. Other metabolites in the ATP production pathway can also be labeled with ^{13}C and would be useful for studying different aspects of tumour development and response to NK therapy. For example, the conversion of [1,4- $^{13}\text{C}_2$]fumarate to [1,4- $^{13}\text{C}_2$]malate is an indicator of necrosis and cell death due to chemotherapy, which is particularly interesting because we observed necrosis in our tumour model (6). Tumours also have a lower extracellular pH, which can be detected through spectroscopy of the conversion of bicarbonate ($\text{H}^{13}\text{CO}_3^-$) to carbon dioxide ($^{13}\text{CO}_2$) (7).

5.2.3 Bioluminescence Imaging

Bioluminescence imaging (BLI) is another imaging modality that could be useful in preclinical studies of NK therapy in prostate cancer. Cancer cell lines transduced with luciferase emit light when the substrate luciferin is injected, then this light is detected by a camera. In these experiments, either the PC-3M cell line or the KHYG-1 cell line could be transduced with luciferase, depending on the desired measurement. One advantage of BLI is that only live cells catalyze the substrate and emit light, whereas with SPIO it is harder to differentiate between living and dead labeled cells (8,9). Another advantage over cell tracking with SPIO is that BLI allows for quantification of the light signal generated (10), while there is less ability to quantify hypointensities in MRI, particularly once the signal is essentially zero with a high dose of SPIO per voxel. If this technique was used with transduced PC-3M cells, it could be used to study metastasis and treatment success. If the KHYG-1 cells were stably transduced with a suitable luciferase expression vector, it could be used for tracking NK cells and monitoring their viability *in vivo*, although the sensitivity would not be as high as it is in MRI when iron oxide nanoparticles are used as a contrast agent.

5.2.4 Imaging NK Cells in Metastatic Models

The orthotopic model is presented here as a model for the treatment of the primary tumour in human patients. However, this is perhaps not representative of how NK therapy would be used clinically; the available immunotherapies are all treatments for late stage metastatic castrate resistant prostate cancer (mCRPC) after the primary tumour has been treated by irradiation or chemotherapy (2). While the orthotopic PC-3M model uses an androgen independent cell line and causes metastases in the locoregional lymph nodes, the primary tumour is too large to allow the spontaneous metastases to grow to a significant size before the mouse must be sacrificed.

There are metastatic models of prostate cancer that may be more representative of the situation in human disease. Cancer cells can be injected directly into the bone marrow (11) to mimic bone metastasis. Bone marrow and bone metastases are hyperintense in bSSFP images, so the bSSFP sequence could still be used to track labeled NK to the metastases, to optimize dose and dose timing, and to monitor the effect of treatment on metastasis volume. Other metastatic models involve the intravenous or intracardiac administration of the cancer cells to cause multiple metastases throughout the body (12), or direct injection of cells into the lymph node (13).

Because the treatment of the primary tumour in clinical practice can include radiation therapy and chemotherapy, it would also be interesting to similarly treat the orthotopic tumour and determine the effect on NK tracking and effectiveness of NK cytotoxicity following such therapy. The different activating and inhibiting ligands on the cancer cells may be up- or down-regulated after treatment with chemotherapeutics and radiation therapy (14), so the effect of each on the cytotoxicity of NK cells could be examined in a more clinically relevant model. Stress induced by treatment can increase the expression of activating receptors, but can also induce ligand shedding which would decrease the NK response. It has been determined that tumour expression of MIC A/B (the ligands for the NKG2D activating receptor on NK cells) is upregulated by radiation therapy and chemotherapy, and there are mixed results on the effect of radiation therapy and chemotherapy on the tumour expression of the ligands for the natural cytotoxicity receptors (14). As well, other experiments show that radiation can make the tumour

microenvironment less immunosuppressive (15). A microCT system has been modified at our site to irradiate small animals and could be used in this experiment (16).

5.3 References

1. Siegel R, Naishadham D, Jemal A. Cancer statistics, 2012. *CA Cancer J Clin* 2012;62(1):10-29.
2. Sonpavde G, Kantoff PW. Immunotherapy for castration-resistant prostate cancer. *The Urologic Clinics of North America* 2012;39(4):465-81.
3. Miller JS, Soignier Y, Panoskaltsis-Mortari A, McNearney SA, Yun GH, Fautsch SK, et al. Successful adoptive transfer and in vivo expansion of human haploidentical NK cells in patients with cancer. *Blood* 2005, Apr 15;105(8):3051-7.
4. Matera L, Galetto A, Bello M, Baiocco C, Chiappino I, Castellano G, et al. In vivo migration of labeled autologous natural killer cells to liver metastases in patients with colon carcinoma. *J Transl Med* 2006;4:49.
5. Brand JM, Meller B, Von Hof K, Luhm J, Bähre M, Kirchner H, Frohn C. Kinetics and organ distribution of allogeneic natural killer lymphocytes transfused into patients suffering from renal cell carcinoma. *Stem Cells Dev* 2004, Jun;13(3):307-14.
6. Gallagher FA, Kettunen MI, Hu DE, Jensen PR, Zandt RI, Karlsson M, et al. Production of hyperpolarized [1,4-¹³C₂]malate from [1,4-¹³C₂]fumarate is a marker of cell necrosis and treatment response in tumors. *Proc Natl Acad Sci U S A* 2009, Nov 24;106(47):19801-6.
7. Gallagher FA, Kettunen MI, Day SE, Hu DE, Ardenkjaer-Larsen JH, Zandt Ri, et al. Magnetic resonance imaging of pH in vivo using hyperpolarized ¹³C-labelled bicarbonate. *Nature* 2008, Jun 12;453(7197):940-3.
8. Guenoun J, Ruggiero A, Doeswijk G, Janssens RC, Koning GA, Kotek G, et al. In vivo quantitative assessment of cell viability of gadolinium or iron-labeled cells using MRI and bioluminescence imaging. *Contrast Media Mol Imaging* 2013;8(2):165-74.
9. Ribot EJ, Martinez-Santesteban FM, Simeanea C, Steeg PS, Chambers AF, Rutt BK, Foster PJ. In vivo single scan detection of both iron-labeled cells and breast cancer metastases in the mouse brain using balanced steady-state free precession imaging at 1.5 T. *J Magn Reson Imaging* 2011, Jul;34(1):231-8.
10. Zabala M, Alzuguren P, Benavides C, Crettaz J, Gonzalez-Aseguinolaza G, Ortiz de Solorzano C, et al. Evaluation of bioluminescent imaging for noninvasive monitoring of colorectal cancer progression in the liver and its response to immunogene therapy. *Mol Cancer* 2009;8:2.

11. Morgan TM, Pitts TE, Gross TS, Poliachik SL, Vessella RL, Corey E. RAD001 (everolimus) inhibits growth of prostate cancer in the bone and the inhibitory effects are increased by combination with docetaxel and zoledronic acid. *Prostate* 2008, Jun 1;68(8):861-71.
12. Killian PH, Kronski E, Michalik KM, Barbieri O, Astigiano S, Sommerhoff CP, et al. Curcumin inhibits prostate cancer metastasis in vivo by targeting the inflammatory cytokines CXCL1 and -2. *Carcinogenesis* 2012, Dec;33(12):2507-19.
13. Lizardo MM, Macdonald IC, Tuck AB, Chambers AF. A new breast cancer model for lymphatic metastasis. *Cancer Treat Res* 2007;135:157-65.
14. Rosental B, Appel MY, Yossef R, Hadad U, Brusilovsky M, Porgador A. The effect of chemotherapy/radiotherapy on cancerous pattern recognition by NK cells. *Curr Med Chem* 2012;19(12):1780-91.
15. Tsuchikawa T, Hirano S, Tanaka E, Matsumoto J, Kato K, Nakamura T, et al. Novel aspects of preoperative chemo(radiation)therapy improving anti-tumor immunity in pancreatic cancer. *Cancer Sci* 2013, Jan 31.
16. Jensen M, Chen J, Holdsworth D, Drangova M, Van Sas F, Wong E. TH-C-220-05: Development of GE explore CT 120 micro-CT for small animal radiotherapy with an in-bore collimator (abstract). *Medical Physics* 2011, Jun;38(6):3863-.

Appendices

Appendix A: Pilot Study of Longitudinal Hyperpolarized ^{13}C Imaging of Tumour Metabolism

Introduction

This study was conducted to attempt to measure a treatment effect of NK cells in orthotopic prostate tumours using hyperpolarized $[1-^{13}\text{C}]$ pyruvate MRI. The experiment was based on the direct injection experiment presented in Chapter 2 and literature reports of tumour treatment with natural killer cells (1). The baseline results from this study are reported in Chapter 4. Here the follow-up results and relationships between volume and lac/pyr ratio are presented. We hypothesized that the lac/pyr ratio would be lower in the treatment group than in the follow-up group, as cancer cells in the treated tumours were killed by the KHYG-1 cells and the untreated tumours continued to grow.

Methods

PC-3M and KHYG-1 were cultured as previously described (no iron oxide labeling) As described in Chapter 4, 500,000 PC-3M were injected into the prostate of male nude mice (6 mice) and allowed to grow for 22 days. On day 22, mice were scanned (^{13}C MRSI) using $[1-^{13}\text{C}]$ pyruvate to quantify tumour metabolism. On day 23, they were scanned using bSSFP (^1H) to obtain tumour volumes. On day 25, $\sim 35\ \mu\text{L}$ of saline (control, 3 mice) or 10 million KHYG-1 in HBSS (treated, 3 mice) were injected directly into the tumours. The incisions were re-sutured and the mice were treated with ketaprofen IP for one day (anti-inflammatory, analgesic) and enrofloxacin intramuscularly (antibiotic) for 3 days. One control mouse died after the injection of saline. Mice in the treatment group also received 25,000 IU of IL-2 IP daily for 3 days. On day 28, the mice were scanned for both pyruvate metabolism and anatomical images then sacrificed.

Tumour volumes and lac/pyr ratios were calculated as in Chapter 4, using Osirix and SAGE, respectively. Pyruvate voxels were classified as low- or high-uptake as in Chapter 4. Percentage change values were calculated as $100\% \times |d22-d28|/d22$. All statistics were calculated in GraphPad Prism 5.0.

Results

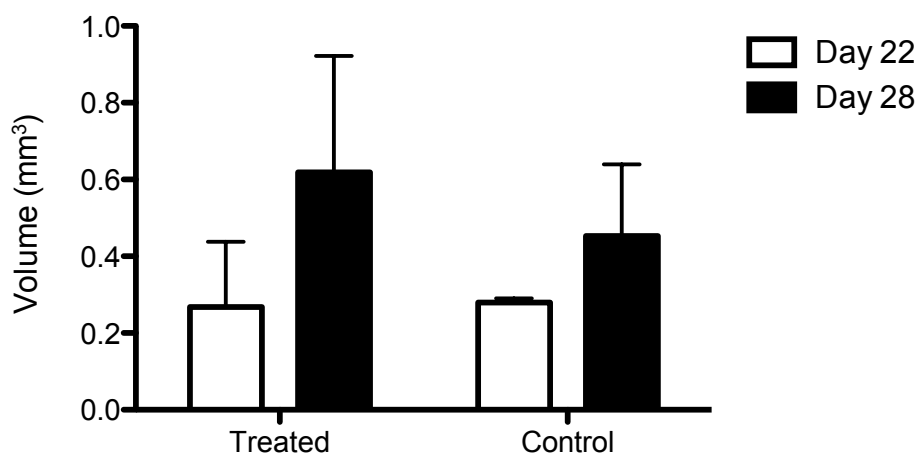


Figure 1: Prostate tumour volume over time.

The volumes of all mice at each time point were included (3 control mice on day 22, 2 on day 28, 3 treated mice at each time point). A 2-way repeated measures analysis of variance was used to compare tumour volume over time and between treatment groups. There was a significant increase in volume overall but there was no difference between groups.

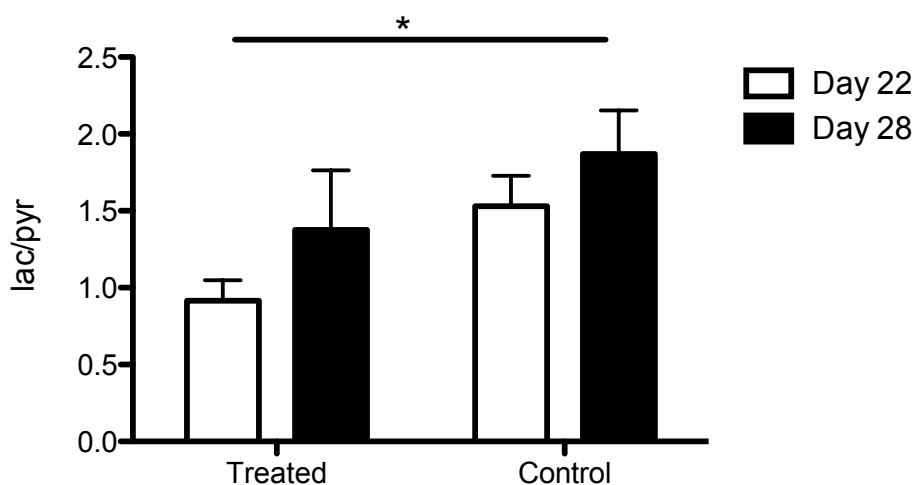


Figure 2: Tumour metabolism over time.

The lac/pyr ratio for 2 control mice and 2 treated mice was compared over time using a 2-way repeated measures analysis of variance. Using a Bonferroni post-hoc test, the treated tumours increased in ratio more than the control tumours (0.46 for treated vs. 0.34 for control). Note: one treated mouse was excluded because the follow-up pyruvate spectrum was acquired through the incorrect section of the mouse so this analysis includes 2 mice in the treated and 2 mice in the control groups.

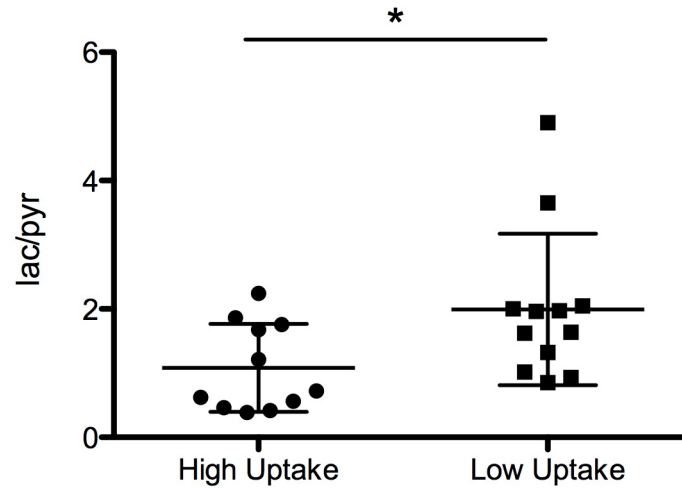


Figure 3: Difference in lac/pyr between high- and low-uptake voxels

Lac/pyr ratio was compared between all high uptake voxels and all low-uptake voxels. At baseline (see Chapter 4), the lac/pyr ratio trended to be higher in the low uptake voxels than the high uptake voxels ($p=0.07$). At follow-up, lac/pyr ratio was significantly higher in low-uptake voxels than high uptake voxels. As discussed in Chapter 4, regions of low pyruvate uptake correspond to regions of necrosis in the bSSFP and histology images. At baseline, 3/6 mice had low-uptake regions in the tumours, while at follow-up, 3/4 did. Both tumours in the control group and one tumour in the treatment group had necrosis.

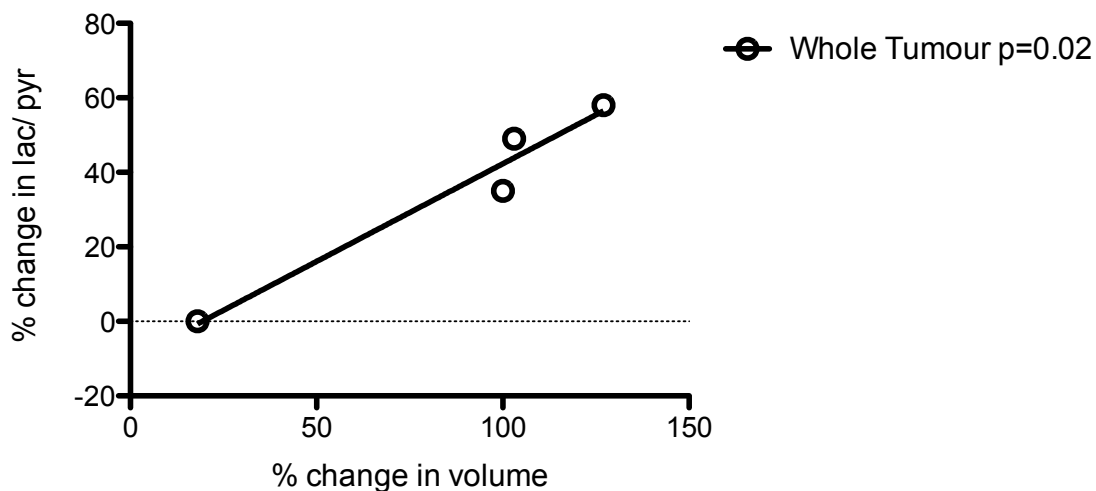


Figure 4: Change in tumour volume and change in lactate/pyruvate are correlated.

The percentage change in tumour volume was compared to the percentage change in lac/pyr ratio for all tumours pooled together. There was a linear relationship between the relative change in tumour volume and the relative change in lac/pyr ratio.

Discussion

Lac/pyr ratio may be a sensitive measure for detecting change in tumour metabolism due to natural killer cell treatment. However, the difference detected here is the opposite of what was hypothesized. Change in tumour volume was correlated with change in lactate/pyruvate. A possible explanation for this effect could be that the tumours were becoming more hypoxic as they increased in size, so there was an increase in anaerobic glycolysis. This experiment should be repeated with a larger sample size and smaller tumours to allow for longer studies and non-necrotic tumours. Histology should be used to determine the biological basis for the signal change.

References

1. Lim YT, Cho MY, Noh YW, Chung JW, Chung BH. Near-infrared emitting fluorescent nanocrystals-labeled natural killer cells as a platform technology for the optical imaging of immunotherapeutic cells-based cancer therapy. *Nanotechnology* 2009, Nov 25;20(47):475102.

Appendix B: Permissions

Rightslink Printable License

https://s100.copyright.com/AppDispatchServlet

JOHN WILEY AND SONS LICENSE TERMS AND CONDITIONS

Jan 22, 2013

This is a License Agreement between Christiane Mallett ("You") and John Wiley and Sons ("John Wiley and Sons") provided by Copyright Clearance Center ("CCC"). The license consists of your order details, the terms and conditions provided by John Wiley and Sons, and the payment terms and conditions.

All payments must be made in full to CCC. For payment instructions, please see information listed at the bottom of this form.

License Number	3074371435732
License date	Jan 22, 2013
Licensed content publisher	John Wiley and Sons
Licensed content publication	Contrast Media & Molecular Imaging
Book title	
Licensed content author	C. McFadden,C. L. Mallett,P. J. Foster
Licensed content date	Nov 29, 2011
Start page	514
End page	522
Type of use	Dissertation/Thesis
Requestor type	Author of this Wiley article
Format	Print and electronic
Portion	Figure/table
Number of figures/tables	6
Number of extracts	
Original Wiley figure/table number(s)	Figures 1, 2, 3, 4, 8, 9
Will you be translating?	No
Order reference number	
Total	0.00 USD

Terms and Conditions

TERMS AND CONDITIONS

This copyrighted material is owned by or exclusively licensed to John Wiley & Sons, Inc. or one of its group companies (each a "Wiley Company") or a society for whom a Wiley Company has

[Print This Page](#)

Dear Christiane Mallett

Thank you for your email. As author of the requested article, you do not need to seek Elsevier's permission to include it / material from it in your thesis as it is part of the rights you retain as an Elsevier journal author.

For further information on the rights you retain as an Elsevier journal author, please visit our web page <http://www.elsevier.com/authors/author-rights-and-responsibilities>.

Yours sincerely
Jennifer Jones
Rights Associate
Global Rights Department

Elsevier Limited, a company registered in England and Wales with company number 1982084, whose registered office is The Boulevard, Langford Lane, Kidlington, Oxford, OX5 1GB, United Kingdom.

Open-Access License

No Permission Required

PLOS applies the [Creative Commons Attribution License \(CCAL\)](#) to all works we publish (read the [human-readable summary](#) or the [full license legal code](#)). Under the CCAL, authors retain ownership of the copyright for their article, but authors allow anyone to download, reuse, reprint, modify, distribute, and/or copy articles in PLOS journals, so long as the original authors and source are cited. **No permission is required from the authors or the publishers.**



In most cases, appropriate attribution can be provided by simply citing the original article (e.g., Kaltenbach LS et al. (2007) Huntingtin Interacting Proteins Are Genetic Modifiers of Neurodegeneration. *PLOS Genet* 3(5): e82. doi:10.1371/journal.pgen.0030082). If the item you plan to reuse is not part of a published article (e.g., a featured issue image), then please indicate the originator of the work, and the volume, issue, and date of the journal in which the item appeared. For any reuse or redistribution of a work, you must also make clear the license terms under which the work was published.

This broad license was developed to facilitate open access to, and free use of, original works of all types. Applying this standard license to your own work will ensure your right to make your work freely and openly available. Learn more about [open access](#). For queries about the license, please [contact us](#).

Appendix C: Animal Use Protocol



March 31, 2010

This is the Original Approval for this protocol
 A Full Protocol submission will be required in 2014

Dear Dr. Foster:

Your Animal Use Protocol form entitled:
 MRI of Cancer Cell Metastasis to the Mouse Lymph Nodes
 Funding Agency Ontario Cancer Research Institute - UWO ROLA #R4174A11; National Cancer Institute of Canada
 - UWO ROLA #R4174A10

has been approved by the University Council on Animal Care. This approval is valid from **March 31, 2010 to March 31, 2011**. The protocol number for this project is **2010-210** which **replace 2006-013** which has expired..

1. This number must be indicated when ordering animals for this project.
2. Animals for other projects may not be ordered under this number.
3. If no number appears please contact this office when grant approval is received.
 If the application for funding is not successful and you wish to proceed with the project, request that an internal scientific peer review be performed by the Animal Use Subcommittee office.
4. Purchases of animals other than through this system must be cleared through the ACVS office. Health certificates will be required.

ANIMALS APPROVED FOR 4 Years

Species	4 Year Total Numbers Estimated as Required	List All Strain(s)	Age / Weight
Mouse	168	120 NuNu Foxn1(088) mice and 48 CB-17 SCID	18-22g

REQUIREMENTS/COMMENTS

Please ensure that individual(s) performing procedures on live animals, as described in this protocol, are familiar with the contents of this document.

The holder of this Animal Use Protocol is responsible to ensure that all associated safety components (biosafety, radiation safety, general laboratory safety) comply with institutional safety standards and have received all necessary approvals. Please consult directly with your institutional safety officers.

c.c. Approval - P. Foster, W. Lagerwerf

The University of Western Ontario
 Animal Use Subcommittee / University Council on Animal Care

Curriculum Vitae

Name: Christiane Mallett

**Post-secondary
Education and
Degrees:** University of Guelph
Guelph, Ontario, Canada
2000-2006 BScH (Co-op)

The University of Western Ontario
London, Ontario, Canada
2006-2008 MSc

The University of Western Ontario
London, Ontario, Canada
2009-2013 PhD

**Honours and
Awards:** Canadian Institutes of Health Research (CIHR) Institute of
Gender and Health/Ontario Women's Council Master's Award
2007-2008

CIHR Frederick Banting and Charles Best Canada Graduate
Scholarship – Doctoral Award
2009-2012

Province of Ontario Queen Elizabeth II Graduate Scholarship in
Science and Technology
2012-2013

**Related Work
Experience:** Research Assistant
Physics Department, Carleton University
2002, 2003

Research Assistant
Physics Department, University of Guelph
2004-2005

Research Assistant
Imaging Research Laboratories, Robarts Research Institute
2006, 2008-2009

Publications:

Christiane L. Mallett, Yuhua Chen, Catherine McFadden, Paula J. Foster. Migration of iron-labeled KHYG-1 natural killer cells to subcutaneous tumors in nude mice, as detected by magnetic resonance imaging. *Cytotherapy*. 2012 Jul;14(6):743-51

Sonali de Chickera, Christy Willert, **Christiane L. Mallett**, Ronan Foley, Paula Foster, Gregory A. Dekaban. Cellular MRI as a suitable, sensitive non-invasive modality for correlating *in vivo* migratory efficiencies of different dendritic cell populations with subsequent immunological outcomes. *International Immunology*. 2012 Jan;24(1):29-41

Catherine McFadden, **Christiane L. Mallett**, Paula J. Foster. Labeling of multiple cell lines using a new iron oxide agent for cell tracking by MRI. *Contrast Media and Molecular Imaging* 2011; Nov-Dec; 6(6): 514-522.

Christiane L. Mallett, Paula J. Foster. Optimization of the Balanced Steady State Free Precession (bSSFP) Pulse Sequence for Magnetic Resonance Imaging of the Mouse Prostate at 3T. *PLoSOne* 2011 Apr 8;6(4):e18361

Iris Shai, J. David Spence, Dan Schwarzfuchs, Yaakov Henkin, Grace Paragga, Assaf Rudich, Aaron Fenster, **Christiane Mallett**, Noa Liel, Amir Tirosh, Arkady Bolotin, Joachim Thiery, Georg Martin Fiedler, Matthias Blüher, Michael Stumvoll, Meir J. Stampfer for the DIRECT group. Dietary Intervention to Reverse Carotid Atherosclerosis. *Circulation* 2010 **121**(10):1200-1208.

Christiane L. Mallett, Lori Gardi, Aaron Fenster, Grace Parraga. Prospective Cardiac Gating of Carotid Three-Dimensional Ultrasound. *Medical Physics* 2009 **36**(7): 3168-3175.

Christiane L. Mallett, Andrew A. House, J.David Spence, Aaron Fenster, Grace Parraga. Longitudinal measurement of carotid atherosclerosis in one, two and three dimensions. *Ultrasound in Medicine and Biology* 2009 **35**(3):367-75.

John L. Campbell, Ralf Gellert, May Lee, **Christiane L. Mallett**, John A. Maxwell, Joanne M. O'Meara. Quantitative in-situ determination of hydration of bright high-sulfate Martian soils. *Journal of Geophysical Research: Planets* 2008 113 E06S11
doi:10.1029/2007JE002959.

Christiane L. Mallett, Joanne M. O'Meara, John A. Maxwell, John L. Campbell. Calibration of the MER α -particle x-ray spectrometer for detection of 'invisible' OH and H₂O possibly present in Martian rocks and soils. *X-Ray Spectrometry* 2006 **35**(6): 329 – 337.

Peer-Reviewed Abstracts:

Christiane Mallett, Catherine McFadden, Paula Foster. Human Natural Killer Cells Labeled with Dual Iron/Fluorescent Agent Tracked to Subcutaneous Prostate Tumors in Nude Mice after Both Intravenous and Subcutaneous Administration. Oral presentation at World Molecular Imaging Congress, September 8-11 2010, Kyoto, Japan.

Christiane Mallett, Catherine Ramsay, Paula Foster. SPIO-Labeled Natural Killer Cells: Cytotoxicity and *In vivo* Imaging. Poster presentation at the annual meeting of the International Society for Magnetic Resonance in Medicine, May 1-7 2010, Stockholm, Sweden.

Christiane Mallett, Paula Foster. Fast, High-Resolution, 3-Dimensional Imaging of the Mouse Prostate with bSSFP. Poster presentation at the Annual Meeting of the International Society for Magnetic Resonance in Medicine, May 1-7 2010, Stockholm, Sweden.

Catherine Ramsay, **Christiane Mallett**, Paula Foster. Efficient Labeling of Multiple Cell Lines with a New SPIO Agent for Cell Tracking by MRI. E-poster presentation at the Annual Meeting of the International Society for Magnetic Resonance in Medicine, May 1-7 2010, Stockholm, Sweden.

Christiane Mallett, Lori Gardi, Janet Pope, J. David Spence, Aaron Fenster, Grace Parraga. Development of cardiac-gated 3-dimensional ultrasound imaging of carotid atherosclerosis. *Medical Physics* 2007 **34**(6): 2332.